Investigations on Two Aspects of Two Important Classes of Nanomaterials: Resistive Switching with Synaptic Applications of TiO$_2$ based Memory Devices and Nonlinear Optical Properties of Perovskite RbPbI$_3$ using SSPM Technique

A thesis submitted towards partial fulfilment
of the requirements for the degree of

Master of Technology
in
Nanoscience and Technology

Submitted by

AVINASH SHAW

Registration no.: 154576 of 2020 - 2021

Exam Roll no.: M4NST22007

Under the guidance of

Prof. (Dr.) Kalyan Kumar Chattopadhyay

Thin Film and Nanoscience Laboratory,

Head of the department - Department of Physics,

Professor-School of Materials Science and Nanotechnology

Jadavpur University

Course affiliated to
Faculty of Engineering and Technology
Jadavpur University
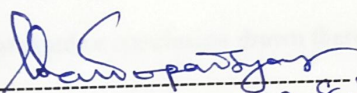Kolkata – 700 032
India

August, 2022

This thesis is dedicated to Allah – Mahaprabhu, for the supremacy and to the Redeemer of my soul.

Also, dedicated to my parents, elder sister, family members and Teachers for their endless love, support, encouragements and sacrifices.

M. Tech. (Nanoscience and Technology)
Course affiliated to
Faculty of Engineering and Technology
Jadavpur University
Kolkata, India

CERTIFICATE OF RECOMMENDATION

This is to certify that the thesis entitled **"Investigation on Two Aspects of Two Important Classes of Nanomaterials: Resistive Switching with Synaptic Applications of TiO₂ based Memory Devices and Nonlinear Optical Properties of Perovskite RbPbI₃ using SSPM Technique"** is a bonafide work carried out by **AVINASH SHAW** under our supervision and guidance for partial fulfilment of the requirement of Master of Technology (Nanoscience and Technology) in School of Materials Science and Nanotechnology, Jadavpur university, during academic year 2020 – 2022.
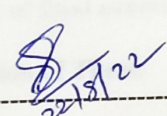

Prof. Kalyan Kumar Chattopadhyay
Thesis advisor
Professor, School of Materials Science and Nanotechnology,
Professor and Head of the Department of Physics,
Jadavpur University,
Kolkata – 700 032.

Prof. Kalyan Kr. Chattopadhyay
Professor and Head
Department of Physics
Jadavpur University
Kolkata – 700 032

Dr. Sourav Sarkar
Director
School of Materials Science and Nanotechnology,
Jadavpur University,
Kolkata – 700 032

Dr. Sourav Sarkar
Director
Associate Professor
School of Materials Science & Nanotechnology
Jadavpur University
Kolkata-700032

Dean
Faculty Council of Interdisciplinary Studies, law and Management
Jadavpur University,
Kolkata – 700 032

Dean
Faculty of Interdisciplinary Studies
Law & Management
Jadavpur University, Kolkata-700032

CERTIFICATE OF APPROVAL **

This foregoing thesis is hereby approved as a credible study of an engineering subject carried out and presented in a manner satisfactorily to warranty its acceptance as a prerequisite to the degree for which it has been submitted. It is understood that by this approval the undersigned do not endorse or approve any statement made or opinion expressed or conclusion drawn therein but approve the thesis only for purpose for which it has been submitted.

Committee of final examination   --

for evaluation of Thesis   --

** Only in case the thesis is approved.

<u>DECLARATION OF ORIGINALITY AND COMPLIANCE OF</u>

<u>ACADEMIC ETHICS</u>

I hereby declare that this thesis contains literature survey and original research work by the undersigned candidate, as part of my Master of Technology (Nanoscience and Technology) studies during academic session 2020-2022. All information in this document has been obtained and presented in accordance with academic rules and ethical conduct. I also declare that, as required by this rules and conduct, I have fully cited and referred all material and results that are not original to this work.

NAME: AVINASH SHAW

ROLL NUMBER: M4NST22007

THESIS TITLE: **"Investigation on Two Aspects of Two Important Classes of Nanomaterials: Resistive Switching with Synaptic Applications of TiO_2 based Memory Devices and Nonlinear Optical Properties of Perovskite $RbPbI_3$ using SSPM Technique".**

Signature: Date:

Acknowledgement

I would like to express my profound gratitude to my guide **Prof (Dr). Kalyan Kumar Chattopadhyay** for his advice and guidance from the very early stage of this research as well as giving me extraordinary experiences throughout the work. He provided me constant encouragement and support in every stage of this research tenure. Also thank you for the welcoming atmosphere at Thin Film and Nanoscience Lab that makes it possible for me to do comprehensive research. All of these gave me tremendous support and enabled me to get through my project's challenging times; without them, I don't believe I could have finished it.

I would also like to express my sincere thanks to **Dr. Sourav Sarkar, Dr. Chandan Kumar Ghosh, Dr. Mahua Ghosh Chowdhury**, for their help, support, encouragement, suggestions and advices during the course of my M. Tech. program.

I am grateful to the **Higher Education Department, Govt. of West Bengal**, for providing me scholarship under the "**Swami Vivekananda Merit Cum Means Scholarship Scheme**" for pursuing my Master of Technology degree course.

I would like to express my sincere gratitude to **Dr. Biswajit Das** for his constant support in these research projects with his wealth of scientific knowledge and ideas. He will always remain very close to my heart not only for his sheer excellence and aptitude in the research field, but also as a good human being. My beloved "dada" who never said "no" at any time of my tenure as well as any queries that seemed really troublesome to my personal life.

Abstract

In the human brain, distributed parallel processing happens due to a vast interconnected network of neurons. For this reason, the human brain can do high-speed data processing tasks and self-learning, language processing, and prediction tasks. And also, the human brain consumes very low power for doing these tasks. So, the human brain is a perfect example in which Von Neumann's bottlenecks are not seen. Researchers do their research in this domain to perfectly mimic the human brain for advanced neuromorphic computing and memory device applications. Titanium dioxide (TiO_2) nanostructures represent a unique combination of shape and functionality where the dimensionality of the nanostructures directly influences the material's properties. Recent research is mainly focused on the cost-effectiveness and efficiency of the device. For these reasons, TiO_2 thin films have been considered the primary material for memory device applications. First part of this thesis entitled **"Study of Resistive Switching and Synaptic Properties on TiO_2-Based Memory Devices and Its Application as Artificial Vision Sensor with Machine Learning Approach",** aimed to investigate the resistive switching (RS) behaviours with synaptic functionalities of TiO_2-based thin film devices. The TiO_2 films are synthesized using the hydrothermal technique. Another major aim is to create a machine learning classifier model that collaborates with the RS device to artificially mimic the human vision system.

After hydrothermal synthesis of TiO_2 thin films, to obtain the best performing device, the growth time has varied from 30 min to 5 h. Following basic characterizations were done for all samples for deep scientific understanding. Fundamental memristor properties are evaluated by current-voltage (I-V) characteristics, followed by retention test, endurance test, and on/off current ratios measurement for all the devices. One hour (abbreviated asT1) device was selected as the best device by comparing all the above-said test results. This

device exhibited up to 10^4 seconds retention time with 599 continuous complete endurance cycles and 8×10^4 on/off current ratio. In the next phase, all synaptic functions like STDP, SRDP, LTP, LTD, PPF, and PPD are emulated by the T1 device successfully for both electrical and optical stimuli. After that, we used the T1 device as an artificial retina for image sensing purposes in terms of light intensity. After a successful image is sensed, we put that image in the Support Vector Machine (SVM) Linear Classifier model (MATLAB program) for recognition purposes. T1 device successfully gave the best result for each input light. This T1 sample can be used in a robotic vision system as an artificial vision sensor (artificial retina) with an experimental linear Classifier model.

In the second work, titled **"Determination of Nonlinear Refractive Index (n_2) and Third Order Susceptibility ($\chi^{(3)}$) for RbPbI$_3$ Perovskite Nanorods in Different Solvents Using SSPM Method,"** we have done a nonlinear optical study of RbPbI$_3$ nanorods. From the above study, the nonlinear optical parameters such as nonlinear refractive index and third-order susceptibility have been calculated using the spatial self-phase modulation (SSPM) technique. This study was done for two solvents to investigate the nonlinear refractive index's dependency on the solvents' viscosity. RbPbI$_3$ halide perovskite nanorods are synthesized using a low-cost, simple chemical route. Basic characterizations like XRD, FESEM, UV-Vis absorbance, and EDS were done to understand this perovskite sample deeply. This type of study has been done for the first time for this material. As a result, RbPbI$_3$ emerges to be a promising material for nonlinear optical applications. The calculated nonlinear refractive indexes were 2.165×10^{-5} and 2.088×10^{-5}, and third-order susceptibility was 9.67×10^{-9} and 8.031×10^{-9} for NMP and 2-propanol solvents, respectively.

Contents

Chapter 1: Introduction

Chapter 2: **Literature review**

Chapter 3: **Instruments, Characterisation Techniques and Synthesis Processes**

Chapter 4: Study of Resistive Switching and Synaptic Properties on TiO$_2$-Based Memory Devices and Its Application as Artificial Vision Sensor with Machine Learning Approach

Chapter 5: Determination of Nonlinear Refractive Index (n_2) and Third Order Susceptibility ($\chi^{(3)}$) for RbPbI₃ Nanorods in Different Solvents Using SSPM Method

Chapter 6: Grand Conclusion and Scopes for Future Works

x

Chapter 1

Introduction

1.1. Introduction:

1.1.1. Nanotechnology – Overview

The engineering of functional system at molecular level is mainly concept of nanotechnology. The idea of nanoscience and technology were present in in-depth imagination of 20th century scientists. Prof. Richard P. Feynman was one of them. Prof. Feynman discussed about it in his scientific talk in American Physical Society on December 29, 1959 entitled "There is plenty room at the bottom". "There are no fundamental reasons that materials could not be fabricated by manipulating at atomic level". [1] In 1980's scientist K. Eric Drexler first introduce the term nanotechnology. "Nanotechnology is the understanding and management of matter at dimensions between about 1 and 100 nanometers where unique phenomena permit revolutionary applications," according to the US National Nanotechnology Initiative (NNI). [2] It is an interdisciplinary domain where mechanical, electrical, chemical, civil, electronics engineers, material scientists, metallurgist, biologists, medical practitioners, chemists, physicists contribute together to extend the existing limits. Generally, 1 to 100 nm is the range for nano dimension. By help of nanotechnology one can make a new nanomaterial using conventional material but the properties of that new material are totally different with conventional one. This advantage gives freedom to a scientist to think out of the box and try to solve different problems. As per example we all familiar with silicon solar cell devices but using nanotechnology measures today scientist made very advanced solar cell devices with the help of transition metal oxides, silicon nanowires, perovskite materials. In nanoscale system most of the classical concepts, theories are not fitted, shows contradictory. As per example, melting point of nano materials, band gap of nanomaterials etc. Quantum physics is the backbone in nanoworld where classical physics is not

appropriately fit. Neil Armstrong described "a small step for a man but giant step for mankind" when he stepped on moon first time. Similarly, nanotechnology is a giant leap for mankind by step too small with respect to Neil Armstrong's would look like a solar system in size. [3]

1.1.2. Classification of nanomaterials based on chemical composition:

Based on chemical compositions nanomaterials are classified into following categories,

1) Carbon based: Graphene, CNT, Fullerene, carbon quantum dot (CQD), carbon black.

2) Metal based: Metal nanoparticles (gold, silver, platinum, tungsten, copper etc.)

3) Metal oxide based: TiO_2, WO, HfO_2, ZnO nanoparticles, nano silica, Al_2O_3 np etc.

4) Composite based: Nanocomposite polymers (organic, inorganic, organo-metallic)

5) Perovskite Nanomaterials

6) Chalcogenide and two dimensional dichalcogenide (TMD) materials.

1.1.3. Classification based on dimension:

Generally nano materials are classified into four categories depending on their dimension,

1) Zero dimension (0-D)

2) One dimension (1-D)

3) Two dimensions (2-D)

4) Three dimensions (3-D)

Another dimension also seen that is 4-D in hemoglobin protein structure.

Zero dimensional nanomaterials are nanoparticles and quantum dots. Here only atomic sized material present. Charge carriers can move in all three x-y-z directions. Carbon

quantum dot (CQD) and fullerene are famous 0-D materials in nano domain. One 0-D nanomaterial shown in figure 1.1,

One dimensional nanomaterial are nanorods, nanofibers, nanotubes. Here only two dimensions considered for charge carrier movement. They are anisotropic nanocrystals, and having large aspect ratio of length and diameter. 1-D nanomaterial shown in figure 1.1. Nanosheet, nanoflakes are 2-D nanomaterials. Here two dimensions are clearly measurable. These are having sheet like structure. Very extensive research done on 2-D nanomaterials till date. Graphene is the famous 2-D nanomaterial.
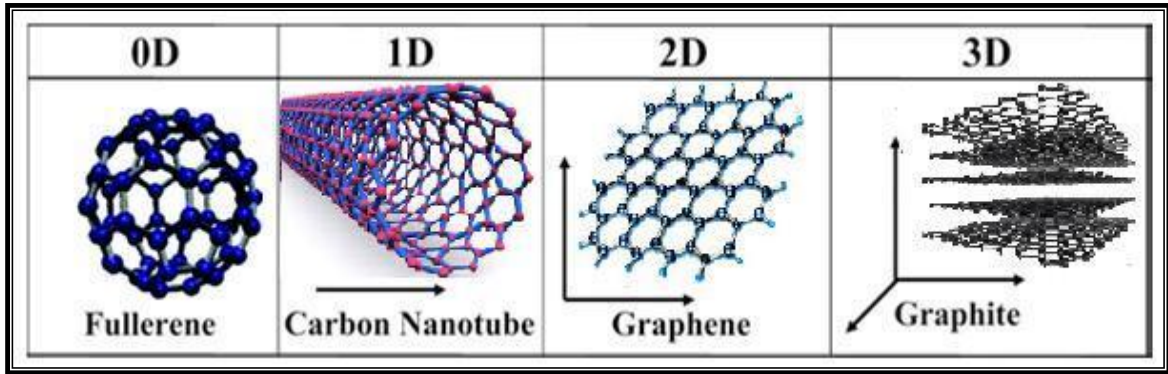
Figure 1.1: Representation of different nanomaterials based on dimensions.

[adapted from internet]

The electronic structure of the materials changes with dimensionality. In a three-dimensional (3D) material (assembly of one-dimension (1D) nanorods, nanowires, nanotubes etc.), it can be shown that the density of states D_{3D} (E) varies with the $E^{1/2}$ and the possible states in which an electron can be found are quasi-continuous. For a two-dimensional material (2D) i.e., nanosheets, nanoflake, nanoplate, nano foil, etc., D_{2D} (E) is still quasi-continuous, but the density of states does not depend on the energy E. Here it is a step-function. For one-dimensional materials (1D), i.e., nanowires, nanorods, nanotubes, nanobelts, nano pins, nanoneedles etc., D_{1D} (E) is proportional to $1/E^{1/2}$ and thus exhibits singularities near the band edges. Finally, in the limiting case when all dimensions shrink,

i.e., for a zero-dimensional solid (0D, quantum dot), D_{0D} (E) is proportional to 1/E which is a delta function [4-6]. Schematic illustration of structural dimensionality of nanomaterials with density of states function are shown in figure 1.2 below.
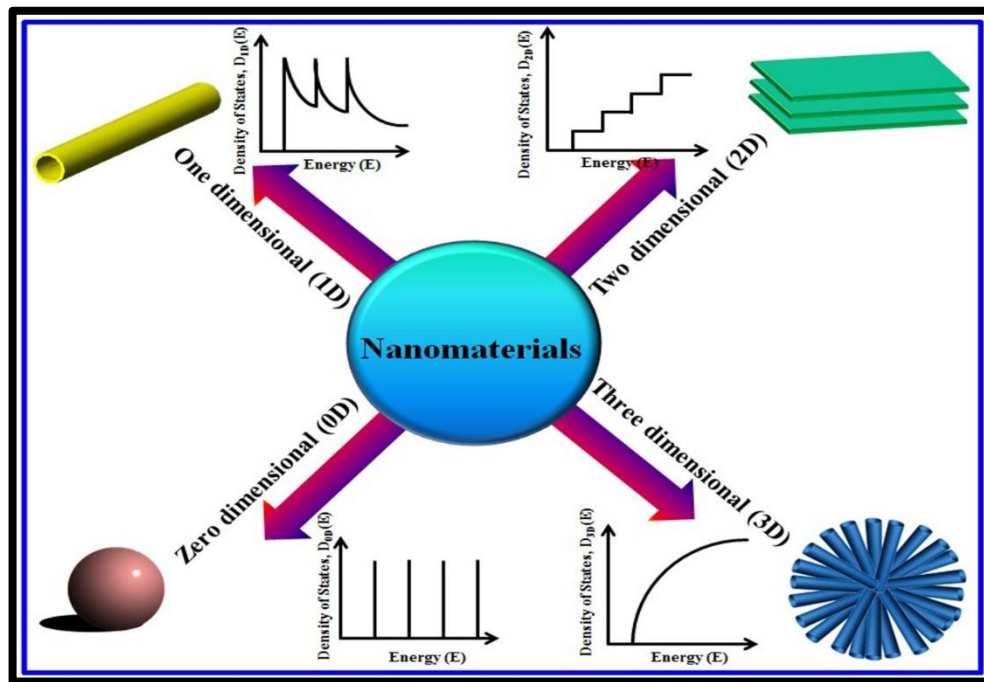
Figure 1.2: Schematic illustration of structural dimensionality of nanomaterials with density of states function. [adopted from internet]

1.1.4. Synthesis of Nanomaterials:

After 50 years of extensive research in nanotechnology, it is obvious that there is no single process for producing nanomaterials. Nanomaterial fabrication can be accomplished in two ways: top-down and bottom-up. In a top-down approach, a bulk material is typically taken and machined into the required shape and result. Manufacturing of integrated circuits with a series of procedures such as crystal growth, lithography, etching, and ion implantation, is an example of this type of technique. Ball milling is a critical top-down approach in nanomaterial production. On the other side, when building something from the ground up,

the bottom-up technique is applied. Nanomaterial is created when atoms of a fundamental material link together. The top-down strategy incorporates some lithographic processes, whereas the bottom-up approach does not. PVD, CVD, electrodeposition, sol-gel, wet chemistry, hydrothermal, and solvothermal processes are examples of bottom-up procedures. A schematic representation of these two techniques as shown in figure 1.3.
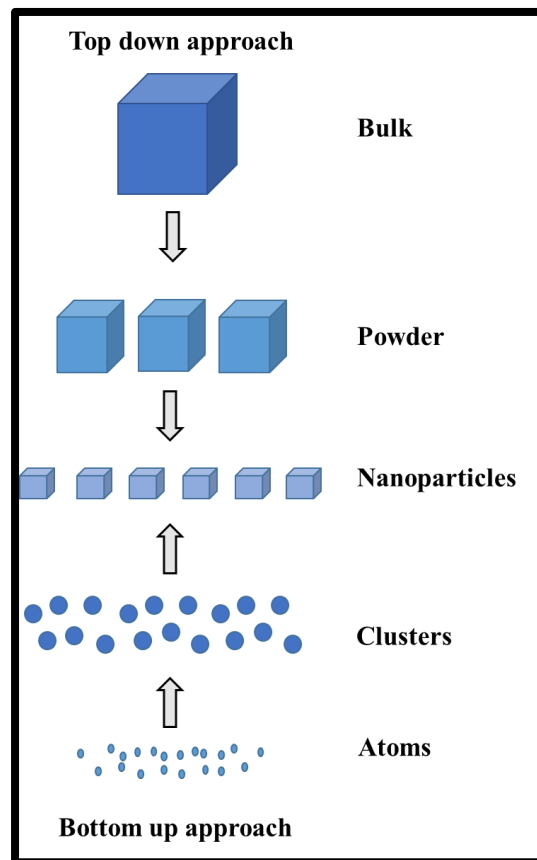
Figure 1.3: Schematic representation of top-down and bottom-up approaches. [adapted from internet]

1.1.5. Characterization of Nanomaterials:

Characterization techniques are of following two types, probe based and another is beam based.

All types are shown as information chart in figure 1.4 for better understanding.
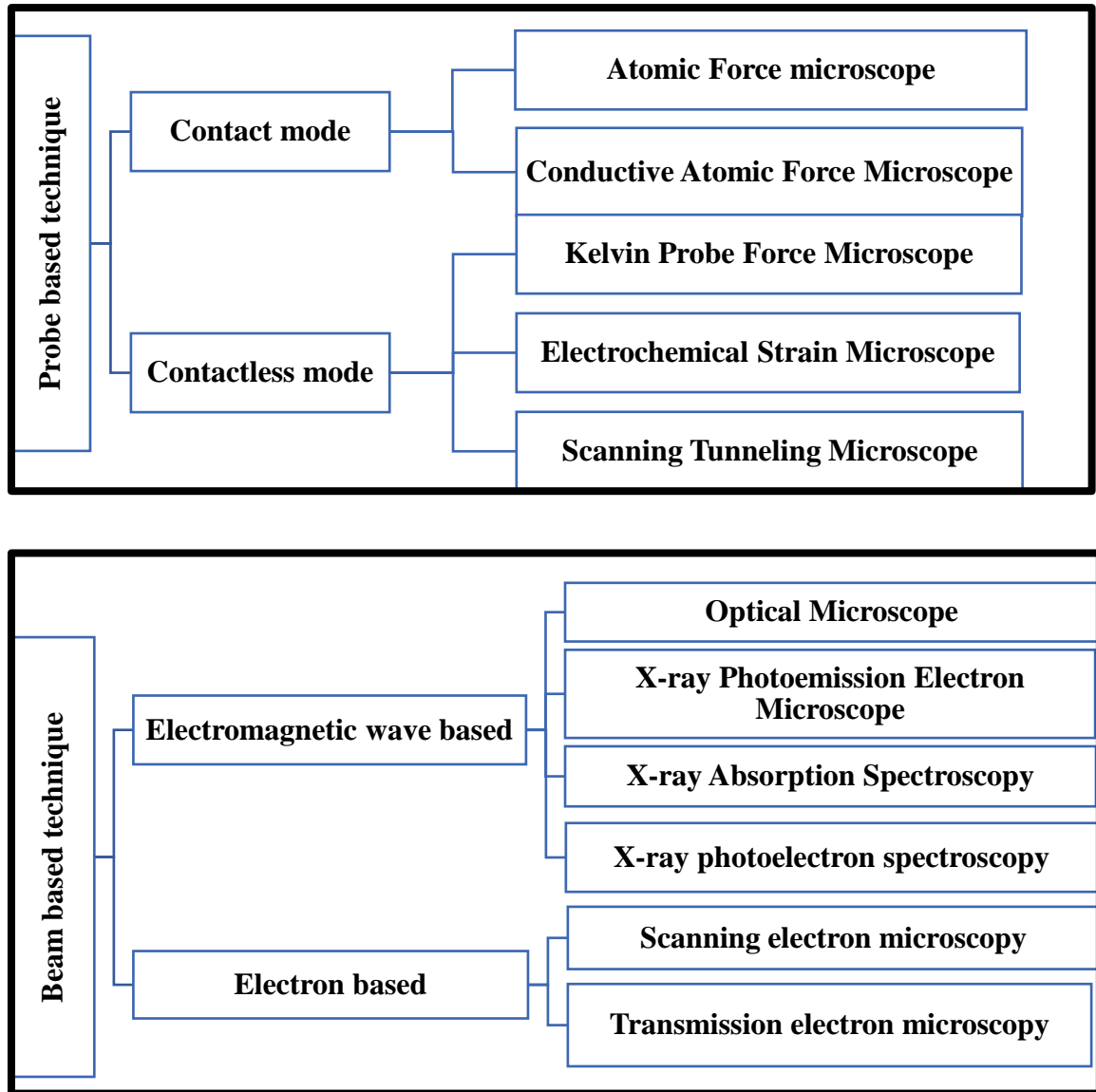
Figure 1.4: Different characterization techniques of probe and beam based shown in chart format.

1.2. General Introduction of Experimental Materials:

1.2.1. Titanium Dioxide (TiO$_2$) - A Novel Material in Nanotechnology.

Titanium dioxide is naturally present oxide of titanium (Ti). The chemical formula is TiO$_2$. It largely extracted from mines on earth as ores e.g., ilmenite, rutile, anatase, leucoxene. [7] "Titanium White", "Pigment White 6" are the industrial name of titanium oxide when it is used as pigment material. Industrial production started since 1918, in Germany, USA, Norway. It applied in various industries like paint, coating, skin care, plastic, electronic semiconductor, hydrogen generation, battery, paper, printing, toothpaste, pharmaceutical etc. Due to its wide range of applications in various industries the demand of pristine TiO$_2$ powder increasing day by day. Titanium dioxide (TiO$_2$) is the most efficient material among the options and has attracted a lot of attention due to its unique properties such as high permittivity, refractive index, effectiveness, low price, chemical stability, non-toxicity, catalytic properties, photostability, and ability to decompose a wide range of organic compounds. It is n-type semiconducting material because it contains electron acceptors and holes as charge carriers.

❖ **Identification information:**

IUPAC name	Dioxo titanium
ICSC number	0338
PubChem CID	26042
Chemical structure	O=Ti=O
Canonical SMILES	O=[Ti]=O

❖ **Different Crystal structures:**

Four different crystallographic forms of TiO_2 under ambient conditions are rutile (most stable form), anatase, brookite, srilankite (TiO_2 II or PbO_2 type TiO_2). [8,9,10] mainly amorphous phase is formed under 350 ℃ and rutile phase formed above 800 ℃. Due to transition metal oxide, it has both crystalline and amorphous forms. TiO_2 crystals are made of d^0 titanium ions (+IV) at the center of octahedra of six O ions. The fundamental structural unit in these four TiO_2 crystals forms from TiO_6 octahedron units and has different modes of arrangement and links the crystal parameters, the Ti-O interatomic distances, and the O— Ti— O bond angles for the four phases are summarized in Table 1.1

Table 1.1: The crystal parameters, the Ti-O interatomic distances, and the O— Ti— O bond angles for the four phases

Properties	Srilankite	Anatase	Rutile	Brookite
Crystal structure	Monoclinic	Tetragonal	Tetragonal	Orthorhombic
Lattice constant (Å)	a=12.16, b=3.74, c=6.51	a=b= 3.78, c= 9.5	a=b= 4.59, c= 2.95	a= 9.18, b= 5.44, c= 5.15
Space group	C2/m	I 4_1/amd	P4_2/mnm	Pbca
Point group		4/mmm	4/mmm	mmm
Ti - O bond length (Å)	-----	1.937 (4) 1.965 (2)	1.949 (4) 1.980 (2)	1.87-2.04
O-Ti-O bond angle	β =107.29	77.7° 92.6°	81.2° 90.0°	77.0°-105°

The schematic crystal structure of three main different phases shown in below figure 1.5,
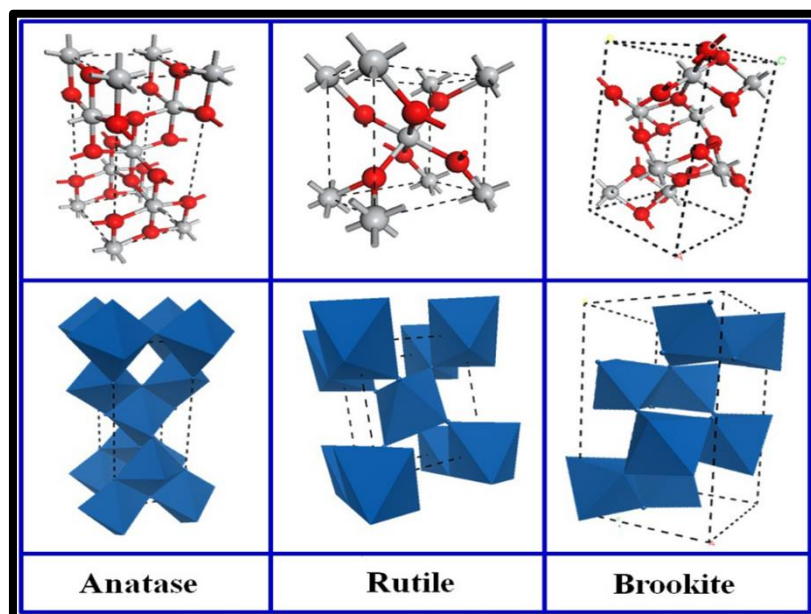
Figure 1.5: Schematic crystal structures of three different phases. [adapted from internet]

❖ Properties of TiO$_2$:

a) Chemical and Physical Properties:

Chemical and physical properties of TiO$_2$ compound are shown as table format in below

table 1.2, [11]

Table 1.2: Tabular representation of chemical and physical properties of TiO$_2$

Property name	Values
Molecular weight	79.87 g/mol
pH	7.5
Exact mass	79.93 u
Topological polar surface area	34.1 Å
Heavy atom count	13

Complexity	18.3
Covalently bonded unit count	1
Canonicalized	Yes
Boiling point	2773.15 to 3273.15 K at 76.0mm Hg (NTP)
Melting point	2128.15 K at 760mmHg (NTP)
Solubility	Less than 1mg/mL at 293.15 K (NTP) (Insoluble in water and organic solvents. Dissolves slowly in hydrofluoric acid and hot concentrated sulfuric acid. Also soluble in alkali.)
Density	3.9 to 4.2 g/cm^3 (NTP)
Hydrogen bond acceptor count	2
Rotation bond count	0

b) Optical Properties:

TiO_2 has very large band gap as semiconducting material. Band gap of TiO_2 lies between 3.05 to 3.26 eV for all possible phases. TiO_2 exhibits high ionic properties and high refractive index value nearly 2.25. It shows high refractive index due to its TiO_6 octahedral structure. Rutile is the most desirable phase in terms of transparency and index value, but it also has the highest birefringence, with n_0 = 52.9 and n_e= 52.6, and is frequently undesirable in terms of scattering. The anatase phase is less birefringent than rutile and has an index of 2.5 [12]. It differs from rutile in the coordination number of its TiO_6 octahedra (10 for rutile, 8 for anatase), is less birefringent, and it has an index of 2.5.

c) Electrical properties:

Donor-type defects, such as oxygen vacancies and titanium interstitials (Ti^{3+} and Ti^{4+}), are primarily responsible for the n-type conductivity and nonstoichiometric of TiO_2, resulting

in the apparent shortage of oxygen TiO_{2-x}. The most practicable defect disorder model that is consistent with the electrical conductivity data for oxidized TiO_2 is based on the assumption that: (i) the predominant defects are oxygen vacancies, (ii) the minority defects are Ti interstitials, and (iii) Ti vacancies may acquire reasonably large concentrations, despite being rather stationary. At normal temperature, single crystal titanium dioxide TiO_2 has a resistivity of around 1013 cm.

d) Defect Equilibrium / Defect Disorder:

Donor-type oxygen vacancies are considered to be the most common defects in n-type TiO_2 across a wide range of stoichiometries, while donor-type titanium interstitials are considered to be the minority defect. The predominant defect may, however, become tetravalent titanium interstitials under extreme conditions, however this is difficult to achieve experimentally. Titanium vacancies, on the other side, can significantly contribute to defect disorder under prolonged oxidative conditions.

e) Dielectric constant:

TiO_2 seems to have a dielectric constant (k) of 40 for anatase and 86-170 for rutile [13-14]. As a result, TiO_2 has been studied as a high-k insulator for transistors and dynamic random-access memories (DRAM) [15-17]. The significant leakage caused by TiO_2's relatively small band gap and n-type conductivity is the most major downside to its application as an insulator. The increased conductivity is mostly based on the ease with which oxygen deficit can be created.

❖ Applications of TiO_2 Nanomaterial:

There are wide range of applications of TiO_2 nanomaterial. All application domains are listed below.

1. Li-ion Batteries

2. Photovoltaic cell

3. Sensor application (different gas sensors, humidity sensors)

4. Field emission display technology

5. Biomedical application – joint replacement, dental implants, cardiovascular implants etc.

6. Photocatalytic application – waste water treatment, water purification etc.

7. Antibacterial surface coatings, paints, self-cleaning devices.

8. Hydrogen production and storage

9. Photocatalytic conversion of CO_2 into hydrocarbon fuels

10. **Nest generation memory devices** – Synaptic resistive switching devices

1.2.2. Halide Perovskite RbPbI$_3$ (Rubidium Lead Iodide): General Introduction:

Calcium titanium oxide material is known as perovskite material. In this type of material calcium titanate ($CaTiO_3$) is the main compound and crystal structure also same as $CaTiO_3$. Other compounds having crystal structure similar to $CaTiO_3$ are known as perovskite structure materials. Main chemical formula is ABX_3. In halide perovskite one halogen is present as X in ABX_3 formula. Other chemical formulas for halide perovskite are ABX_4, A_2BX_4, $A_{n+1}B_nX_{4n+1}$ $A_nB_nX_{3n+1}$. These halide perovskites having 2D and 3D connected network where corners shared by metal halide octahedral.

Halide perovskites having extraordinary properties which makes them promising candidate for active material for advanced resistive switching device application. The properties are as follows:

a) Tunable bandgap [18-20]

b) Majority carrier control [21,22]

c) Fast ion migration [23-25]

d) Super flexibility [26-28]

By defect engineering and addition of various suitable substitute materials in crystal structure can changed these above said properties. In halide perovskite I-V hysteresis caused by fast ion migration.[29]   Substitution of the elements in each site can caused bandgap tuning in HPs. Substitute the metal cation in B site to adjust the bonding of metal cation in B site and halide anion in X site.[30] Metal cation also determined the band edge, for this reason by tuning the VBM and CBM also manipulated.

'A' cations are responsible for stability in ABX_3 crystal structure based perovskites. Our material $RbPbI_3$ having orthorhombic crystal structure with P_{nma} space group similar to NH_4CdCl_3 crystal structure. This halide perovskite has stable crystal structure and not change to another phase until it melts. [31] lattice constants decrease with decrease in halide atomic size from I to Cl. It is clearly understand using following table 1.3 below,

Table 1.3: Different values of lattice constants for rubidium lead halide perovskite material when halide are I, Br, Cl respectively. [32]

	Lattice constants (Å)		
	a	**b**	**c**
RbPbI₃	10.54	4.89	17.81
RbPbBr₃	9.52	4.67	16.67
RbPbCl₃	9.10	4.47	15.94

A schematic crystal structure of RbPbI₃ shown in figure 1.6. RbPbI₃ is an indirect bandgap semiconductor because valance band maxima (VBM) and conduction band minima (CBM) situated at Γ and X respectively shown in figure.1.7.
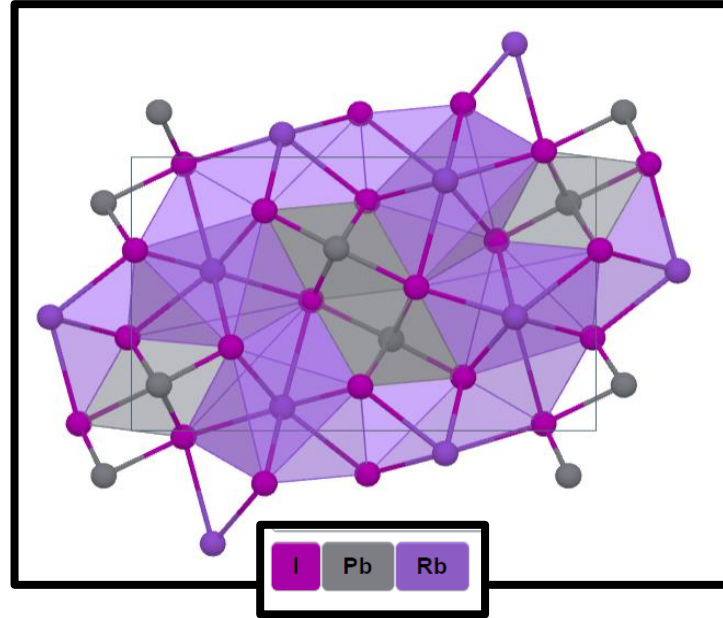
Figure 1.6: A schematic crystal structure of RbPbI₃ perovskite. [33]
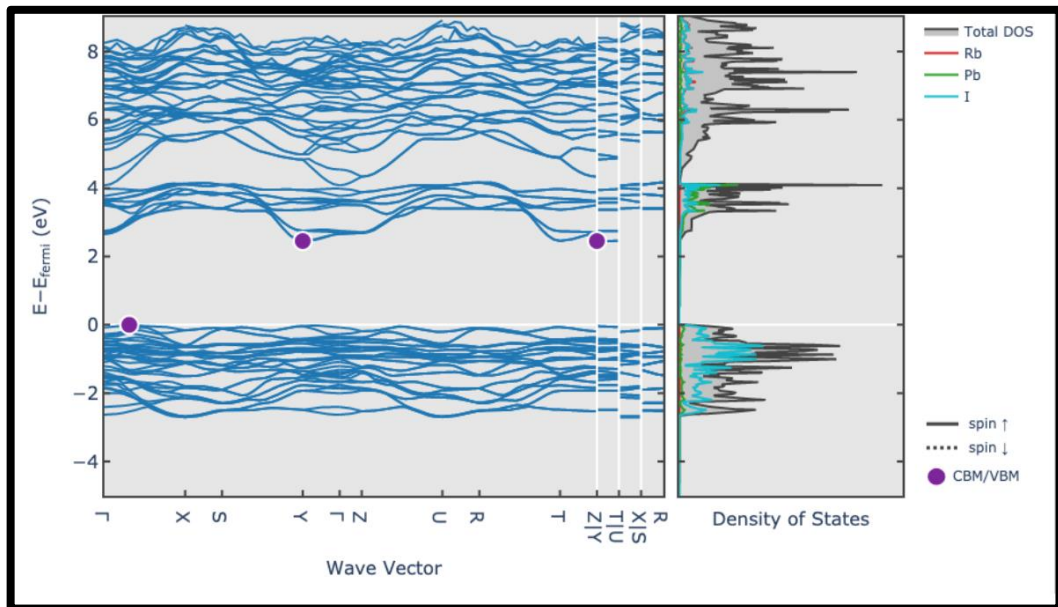
Figure 1.7: Band structure and density of states (DOS) of RbPbI₃ material. [33]

The bandgap values lie between 2.44 to 4.12eV where 2.44eV is conduction band minimum (CBM). Effective mass of charge carriers is important parameter for carrier transport properties in inorganic halide perovskite based electronic devices. In $RbPbI_3$, holes are efficiently transported because of their minimum effective mass. Compared with other halide perovskite materials, the effective mass of carriers is higher due to flat nature of band diagram of $RbPbI_3$. In this perovskite VBM occupied by p orbits of halide atoms and CBM occupied by p orbits of Pb atoms. Refractive index of $RbPbI_3$ is 2.237 and dielectric constant is 5.005.

1.3. Discussion for the Memory Device Application:

❖ Different Types of Next Generation Memories and Comparisons Between Them:

There are mainly four types of next generation memories invented till now to eliminating the drawbacks of conventional one. They are as follows,

1) Ferroelectric RAM (FeRAM): In this type of memory dielectric layer replaced by ferroelectric layer.

2) Magneto resistive RAM (MRAM): It is also known as Spin Transfer Torque MRAM (STTMRAM). In a magnetic tunnel junction, the orientation of magnetic layer is the key concept of this kind of memories.

3) Phase Change RAM (PRAM): It uses phase change property of chalcogenide glass from amorphous to crystalline phases.

4) Resistive RAM (ReRAM): the main mechanism based on change of resistive states (HRS, LRS) by creation and rupture of conductive filaments in dielectric layer.

One descriptive comparison between NAND flash memory with these next generation memories are shown in below as table format in table 1.4.

Table 1.4: comparison between NAND flash memory with other next generation memories.

Particulars	NAND flash	FeRAM	STTMRAM	PRAM	ReRAM
Writing time	1 ms	10-100 ns	10-50 ns	20 ns	5 ns
Reading time	100 μs	10-100 ns	10-50 ns	~50ns	~5 ns
Cell size (relative)	1	4.4	4.0	0.9	0.8
Endurance	$>10^5$	$>10^{14}$	$>10^{16}$	$>10^8$	$>10^{10}$

❖ Why Resistive RAM (ReRAM) chosen?

The majority of next-generation memories outperformed traditional NAND Flash memory in terms of performance. They do, however, have a problem seeing as how the cell size is greater than that of conventional flash memory. In next-generation memory techniques, scalability is a critical factor. Basically, these next-generation memories are approach for bypassing the scaling shortcomings of conventional NAND Flash memory. It's tough to replace traditional NAND Flash memory without decreasing cell sizes. ReRAM has received extensive attention as a promising candidate for next-generation memory since it has the highest terms of scalability and performance.

❖ Resistive Switching (RS) Phenomenon:

It is this switching process resistance state goes from high to low of an active layer by applying external electric field. It is analogous to Prof. Chua's prediction of memristor in which the device can memorize the last current value as a function of resistance that passes through it. [34] This change is nonvolatile and reversible in nature. It first reported in 1960's when scientists observed negative differential resistance in binary oxides. In 2008, HP lab first made and experimentally proved the Prof. Chua's prediction in transition metal

oxide based resistive switching crossbar array device under supervision of Prof. R. Stanley Williams. RS device mainly consists of three layers like metal-insulator-metal (MIM). [35] This insulating material may be transition metal oxides, perovskite materials, polymer nanocomposites with charge trapping elements, carbon based and silicon-based semiconductors. RS mainly two types, one is unipolar and another is bipolar resistive switching. Both types are present in TiO_2 based memristors reported till date. In unipolar case the resistive state change either the same or opposite polarities of applied external field. In bipolar resistive switching process, the memory states toggled between two states when external electric field applied. The compliance current needed for unipolar resistive switching. Many scientists explained the RS mechanism by various processes e.g., spatial inhomogeneity, oxygen vacancy migration, trapping of charge carriers, Schottky barriers, interfaces and electric 'faucets', filamentary path formation, Mott metal-insulator transitions, correlation effects etc.. main mechanisms are illustrated in latter. To overcome conventional drawbacks of separation of memory and processing units in computers, scientists proposed processing inside the memory concept. In this concept three techniques are concluded e.g.,

a) Processing with memory (PwM) – memory device itself a processing unit.

b) Processing in memory (PiM) – processing device is integrated with memory unit but both are separated.

c) Processing near memory (PnM) – processing unit is situated near memory.

Some unique properties of resistive switching:

1. High switching speed.

2. High density.

3. Low power consumption near picojoules.

4. Processing capabilities.

The interface plays a precise role in RS device performance. An additional thin layer introduced within the device interface can dramatically change power consumption, device retention, uniformity, on/off current ratio etc. The on/off current ratio will increase with interface engineering. For this reason, leakage current will decrease. And the negative set phenomenon is solved by insertion engineering.

❖ **Resistive Switching Mechanisms:**

Three types of nonvolatile RS mechanisms reported till date. They are shown in below figure 1.8.

```
                    ┌─────────────────────┐
                    │   Non-volatile RS   │
                    │     mechanisms      │
                    └─────────────────────┘
         ┌───────────────────┼───────────────────┐
┌─────────────────┐ ┌─────────────────┐ ┌─────────────────┐
│ Electrochemical │ │ Valence-charge  │ │ Theromochemical │
│ metalization    │ │ mechanism (VCM) │ │ Mechanism (TCM) │
│ (ECM)           │ │                 │ │                 │
└─────────────────┘ └─────────────────┘ └─────────────────┘
```
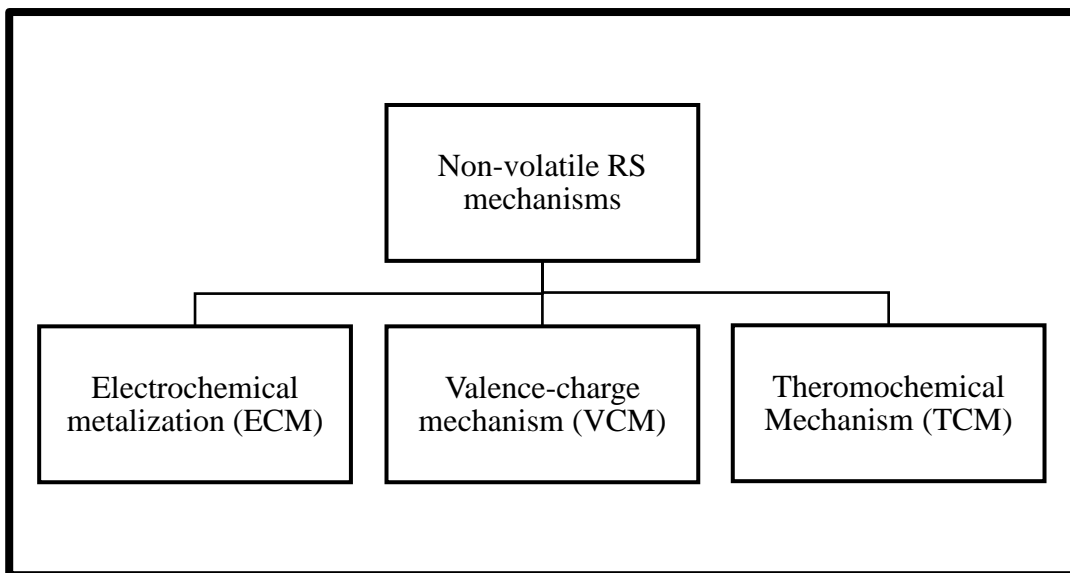
Figure 1.8: Different types of nonvolatile RS mechanisms.

Another one is present but for volatile switching that is Threshold Switching (TS).

By applying specific write voltage pulse resistance state of the device switched to LRS from HRS. This process is known as SET process. similarly, when erase pulse applied then device goes down to HRS from LRS. This is known as RESET process.

a) **Electrochemical metallization (ECM):** The mechanism based on the redox reactions of active metal electrode in active layer. The active layer sandwiched between an active electrode (Ag, Cu, Ni) and an inactive electrode (Pt, Pd, W, Au, Sn). Oxidation of active electrode and reduction of inactive electrode inside the insulating layer form the conductive filament (CF). After applying forward bias at anode side, oxidation starts in anode/insulator interface. We take as example that the active electrode is Ag. The oxidation reaction shown in below,

$$Ag \longrightarrow Ag^+ + e^-$$
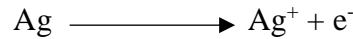
The Ag^+ ions gathered towards cathode. And combined with e^- from cathode to become Ag again.

$$Ag^+ + e \longrightarrow Ag$$
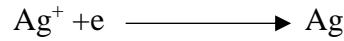
By this process Ag deposited and form CF. the device switched to LRS from HRS. By applying reversed bias to anode side, the CF start rupturing from middle by dissolving Ag atoms. And the device switched to HRS from LRS. This rupturing process may be partial or complete depending on strength of external field.

b) **Valence-charge mechanism:** It is mainly observed in TMO (Transition Metal Oxide) based RS devices. Oxygen vacancies plays a crucial role in it act as a main player. By applying positive bias, generation of oxygen vacancies starts. These construct an electric channel by releasing O^{2-} from its position and drift to anode oxide interface for formation of "oxygen reservoir".

$$O \longleftrightarrow V_O^{2+} + O^{2-}$$

Opposite process happens when reverse bias applied. O^{2-} migrate back to its previous positions. In this process metal ions not contribute to form CF. Vo^{2+} Oxygen vacancies have grater mobility and diffusion rate that metal ions. Water or moisture plays a crucial role in VCM.

In TCM thermal effect influence the switching process. RESET process in TCM joule heating is broadly believed to induced the rupture of the CF at the thinnest position. Now a brief description of Memristor given in next discussion.

❖ **Memristor: Fundamental Step into Synaptic Memory Devices**:

Memristor is a new concept of fourth fundamental circuit element first postulated almost 50 years ago by Prof. Leon Chua in his IEEE publication. [34] But to develop a functional practical prototype of it, takes 37 years. Prof. R. Stanley Williams et al. first made a fully practical and successful prototype of a metal oxide based memristor device for their crossbar array application [35]

Memristor is a resistor with memory. It can store minimum one bit. It is nanoscale two terminal, nonvolatile, non-linear circuit element. The symbol of memristor shown below in figure 3. It can regulate the flow of current in an electrical circuit and also memorize the last number of electrical charges passes through it or last amount of voltage applied through it.
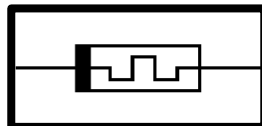
Figure 1.9: symbol of memristor (adopted from internet)

If we consider a charge controlled memristor, then we can write;

$$\phi = f(q)$$ (1)

Where, ϕ is electric flux and 'q' is the amount of charge.

Now differentiating both side with respect to time, then we get,

$$\frac{d\phi}{dt} = \frac{df(q)}{dq}\frac{dq}{dt}$$ (2)

Or, $$v(t) = M(q).i(t)$$ (3)

We can write the above equation because, we know $v(t) = \frac{d\phi}{dt}$, $i(t) = \frac{dq}{dt}$,

$$\therefore M(q) = \frac{df(q)}{dt}$$ (4)

M(q) is the **memristance** of the device, and unit is **ohm.** [36]

A schematic diagram of metal oxide memristor shown in figure 1.10.
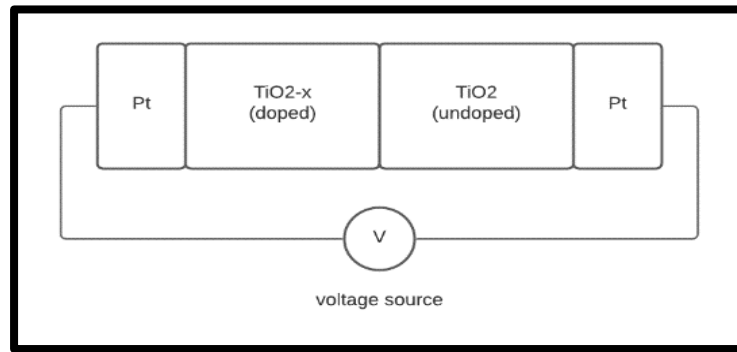
Figure 1.10: Schematic diagram of TiO$_2$ memristor.

When an external voltage source applied across it, then resistance decreases as the current flow through it in forward direction. For these reasons doped layer increases due to movement of oxygen valences. As we reduce the voltage then the current flow decreases and show the opposite feedback loop in voltage – current curve. The I-V characteristics

(hysteresis curve of memristor) shown in figure 1.11. This happens due to shifting of boundary of doped and undoped region. It is clearly shown that at (0,0) position of hysteresis curves the current and voltage both are zero. By his characteristic curve we can clearly understand the non-linearity of memristor device. With different frequencies the shape of the curve will change, and at the higher frequency nearly infinite, the memristor behaves as a simple resistor device
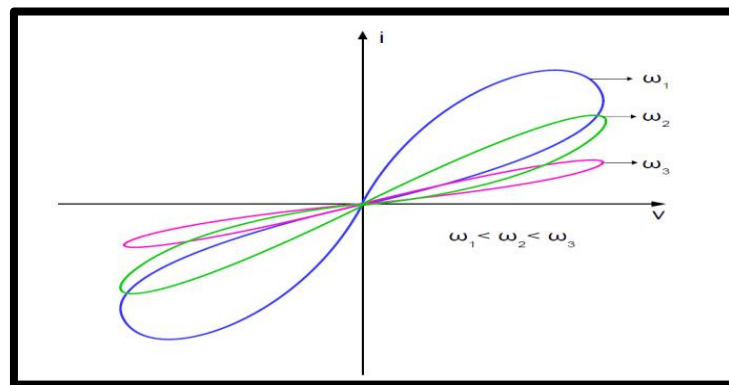
Figure 1.11: Hysteresis loop curve for metal oxide memristor (adopted from [36]).

Memristor can store the data in 0 and 1 form by resistance changing by applied voltage through it. The need of memristor as a memory device is for, conventionally used random access memory (RAM) has volatile nature. For this when power loss then sored data will erased automatically in RAM. And for high data fetching and writing applications we cannot use secondary storage devices. As, these disadvantages overcome in memristor based device, scientists try to developed faster and non-volatile primary storage device mainly ReRAM (Resistive Random-Access Memory). Memristor shows biological synaptic like switching characteristics with high level of plasticity. For these reasons, memristors are used to developed artificial synapses in neuromorphic computing especially wearable electronics, IoT applications etc.

Memristors can be built with various materials like metal oxides, chalcogenides, amorphous silicon, CNT, perovskite QDs, nanocomposite materials, which shows voltage variable resistance properties.

Some properties of memristor are listed below:

- Continuously variable resistance

- Fast switching property. (<10nS)

- Low energy operation (~1 pJ)

- High write endurance (~10^{10})

- Scalability

- Stack-ability

- CMOS compatibility

❖ Why Adapting Synaptic Properties in Memory Devices?

New age computing techniques require high-speed data transfer, low power consuming processors, event-based parallel processing (simultaneously processing and memorizing) and combined memory and logic units in a unit. These extraordinary properties are not in our present computer CPUs because computers are designed based on von Neumann architecture. But the human brain has these extraordinary properties compare to present computer processors. In the human brain distributed parallel processing happens due to a vast interconnected network of neurons. For this reason, the human brain is capable of doing high-speed data processing tasks, as well as self-learning, language processing, and prediction tasks. And also, the human brain consumes less power to doing these tasks. So, the human brain is a perfect example in which Von Neumann's bottlenecks are not present.

Researchers do their research in this domain to perfectly mimic the human brain for advanced neuromorphic computing applications.

❖ Brief Overview of Biological Synapse and Synaptic Characteristics:

Our brain has nearly 10^{11} neurons and nearly 10^{15} synapses with in it. Biological neurons can modulate the received signal from previous neuron. When the modulated signal exceeds the threshold value then the neuron produces action potential which is transmitted through the axon and then synapses. Biological synapse consists of two neurons one is pre-synaptic another is post-synaptic neuron. The connecting region is known as synaptic zone. A biological synapse with all components is shown in figure 1.12, below.
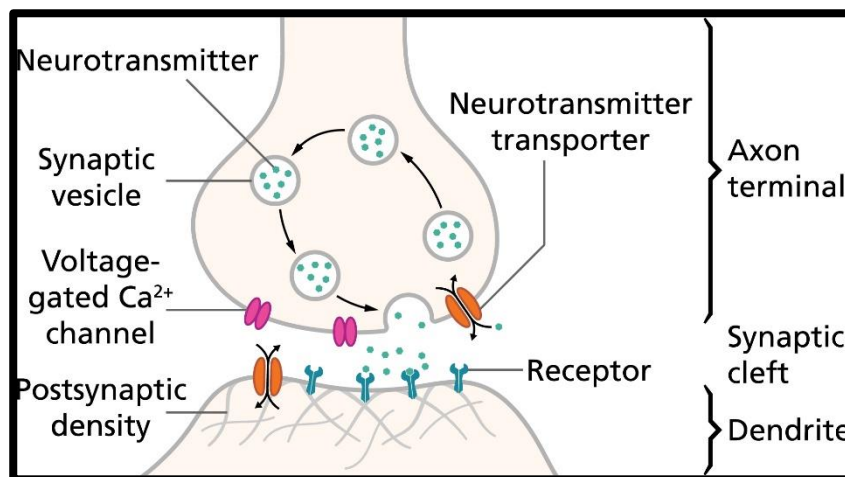
Figure 1.12: biological synapse schematic diagram [adopted from internet]

By electrical pulses and electrochemical signals, the information transferred from pre to post synaptic neuron. Here, the neurotransmitters (dopamine, serotonin, histamine, GABA, glutamine, dynorphin), enzymes, proteins and the charged ions (Ca^{2+}, Na^+, K^+, Mg^{2+}) are plays a key role to transfer the sensory information from pre to post synaptic neurons. These neurotransmitters diffuse into synapse from pre synaptic neuron and bind with the specific

receptors onto the post synaptic neuron derma. By this mechanism the potential of two neuron membranes changes and for this the information transmitted between toe neurons. Synaptic weight is the connection strength between two neurons, and its change is called synaptic plasticity. Synaptic plasticity is mainly two types e.g., autonomous synaptic plasticity, and non-autonomous synaptic plasticity. The classification is shown in figure 1.13 below,
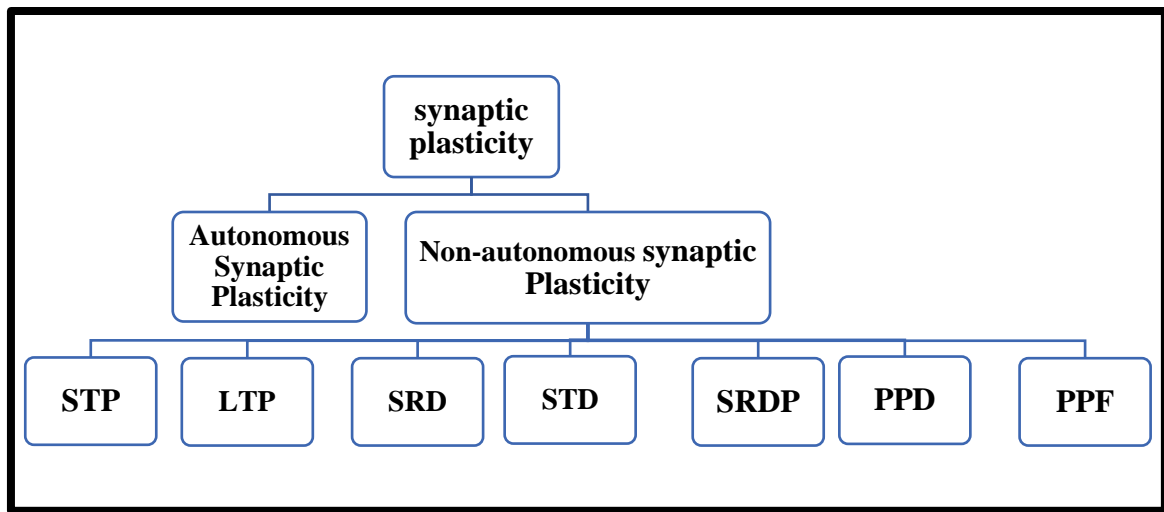
Figure 1.13: Different types of synaptic functionalities.

Synaptic plasticity is responsible for cognitive learning and memory applications in human brain.

In this context we need a device or element which have high data transfer speed, low power consumption and non-volatility. Memristors are the suitable candidate in this purpose. Memristors have all mentioned properties. I discussed briefly about memristors in earlier.

Some synaptic functionalities are listed below, which are the main parameters to justify the new neuromorphic device as artificial synaptic device,

1. Spike time dependent plasticity (STDP)

2. Spike rate dependent plasticity (SRDP)

3. Short term plasticity (STP)

4. Long term plasticity (LTP)

5. Paired pulse depression (PPD)

6. Paired pulse facilitation (PPF)

7. Excitatory post-synaptic current (EPSC)

Firstly, scientists try to make synaptic devices which stimulate only by electrical input pulses, but now they also construct synaptic devices which are stimulated by light stimuli also. This development opens a new sub-domain name optoelectronic neuromorphic device and computing.

1.4. Brief Introduction of Spatial Self phase modulation (SSPM) Technique:

The terminology Spatial Self-Phase Modulation (SSPM) refers to the phase modulation of an optical field traveling through an optical medium caused by the spatial distribution of the applied intensity and the optical medium's unique nonlinear refractive index. [37] Due to the coherent superposition of transverse wave vectors with spatially modulated optical phases caused by the characteristic nonlinear refractive index of the optical medium and the spatially distributed intensity of the Gaussian beam, the SSPM of Gaussian beam in the nonlinear optical materials exhibits the optical concentric diffraction rings at the far-field. According to the even- or odd-integer difference of the nonlinear phase shift, which is regulated by the nonlinear refraction coefficient and the input intensity, the optical field with intensity-modulated spatial phases interferes either constructively or destructively with itself. Strong coherent light-matter interaction causes spatial phase modulation of the incident laser light and diffraction ring patterns in the far field. Following the discovery of the SSPM in liquid crystals by Durbin et al., Wu et al. explored the third-order nonlinear

susceptibility in exfoliated graphene using the SSPM technique in 2011. [38-40] Since then, SSPM has seen a sharp rise in attention, and numerous research teams have looked into the nonlinear behavior of various kinds of materials. Quantum confinement and nonlinear optical absorption are the main reasons for strong nonlinear optical properties in materials.

Halide perovskite materials have strong linear and nonlinear optical and electrical properties, due to these they applied in many optoelectronic applications, optical applications etc. $RbPBI_3$ has relatively thermodynamically stable at room temperature and stable crystallographic structure due to large I atoms in halogen part. Nonlinear refractive index is the change in refractive index of the material or medium is proportional to the incident light intensity. It is denoted by n_2. By intensity dependent SSPM we got third order nonlinear susceptibility and nonlinear refractive index. Many halide perovskites were used to determine the nonlinear optical properties of that materials by researchers worldwide but $RbPBI_3$ first used in this work. this is a novel of its kind for this perovskite to determination of nonlinear optical refractive index (n_2) with different solvents and also nonlinear third order susceptibility ($\chi^{(3)}$).

❖ **Theory and Mathematical Foundation of SSPM Technique:**

Kerr effect is the foundation principle behind SSPM response of nanomaterials.[41] This effect only applicable in laser light sources. The nonlinear refractive index of a material proportionally changes with incident light intensity. That means if intensity increases then nonlinear refractive index of that material also increases under same conditions. The relationship as follows,

$$n = n_0 + n_2 I \qquad \text{.............} \quad (5)$$

here, I = intensity of incident light beam

n_0 = linear refractive index of that material

n_2 = nonlinear refractive index of that material

Phase of incident beam modulated by this Kerr effect. Here incident laser beam has Gaussian distribution. And nonlinear phase shift $\Delta\Psi$ (r) written as follows,

$$\Delta\Psi\ (r) = \frac{2\pi n0}{\lambda} \int_0^{Leff} n_2\ I(r,z)dz \qquad \ldots\ldots\ldots\ldots\ldots\ldots \ (6)$$

R $\in$ [0, +∞) is the radial position of Gaussian beam

L_{eff} = effective length of the light beam travelling through cuvette

λ = wavelength of the laser beam

The phase shift $\Delta\Psi$ (r) of incident beam gets modulated because of changing nonlinear refractive index of material through Kerr effect. This phase shifting resulted diffraction rings in the far field due to spatial self-phase modulation process. The schematic representation shown in the figure 1.14.
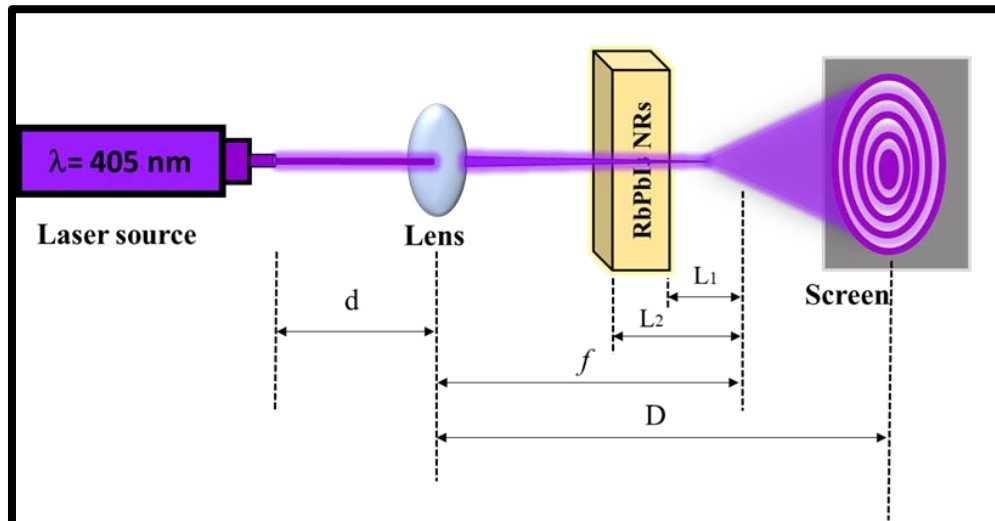
Figure 1.14: Schematic representation of generated diffraction rings due to SSPM

Two points in Gaussian incident field have same slopes, so, they are in same phase and construct bright rings in far field. Diffraction pattern have combination of bright and dark rings that governed by the following equation,

$$\Delta\Psi\ (r_1) - \Delta\Psi\ (r_2) = 2M\pi \qquad \dots\dots\dots\dots\dots\dots \text{(7)}$$

M = integer number, odd for dark rings, even for bright rings.

L_{eff} expressed as the following relation,

$$L_{eff} = \int_{L1}^{L2} \left(1 + \frac{z^2}{z0^2}\right)^{-1} dz = z_0 \tan^{-1}\left[\frac{z}{z0}\right]_{L_1}^{L_2} \qquad \dots\dots\dots\dots\dots \text{(8)}$$

Here $z_0 = \dfrac{\pi\omega_0^2}{\lambda}$ and $\omega_0 = \dfrac{1}{e2}$ beam radius, L_1, L_2 are the distances from focus (f) to cuvette sides.

From equation 2 and 4 we get,

$$n_2 = \frac{\lambda}{2n_0 L_{eff}} \cdot \frac{dN}{dI} \qquad\qquad \dots\dots\dots\dots\dots \text{(9)}$$

Here, I (0, z) = 2I = central peak intensity of Gaussian beam.

n_2 is nonlinear refractive index of experimented material.

$\dfrac{dN}{dI}$ = slope of intensity vs rings no graph.

Third order nonlinear susceptibility $(\chi^{(3)})_{total}$ getting from following equation. [42]

$$(\chi^{(3)})_{total} = \frac{cn_0^2}{12\pi^2} 10^{-7} n_2 \text{ (e.s.u.)} \qquad \dots\dots\dots\dots\dots \text{(10)}$$

c = velocity of light in free space.

$$(\chi^{(3)})_{total} = (\chi^{(3)})_{monolayer} \times N^2_{eff} \qquad \dots\dots\dots\dots \text{(11)}$$

here, N_{eff} = effective number of layers of material in cuvette.

$(\chi^{(3)})_{total}$ strongly dependent on incident optical electric field.

Equation 8, 9, 10, 11 is used to calculate desire parameters.

1.5. Aims and Objectives of Thesis:

- To understand the various synaptic properties and sense signal transport mechanism in human nervous system and also understand the mechanism of human vision system.

- To understand the basics of memristor devices.

- To understand how memristors are used for neuromorphic computing.

- Study past works done in this field.

- To study the TiO_2 as active material in our experimental memory device.

- Study the various synaptic functionalities in our synthesized devices and also build a model for artificial vision system by using machine learning approach.

- To understand the basics of nonlinear optical principle and SSPM technique for determination of nonlinear refractive index and third order susceptibility of any material.

- To synthesis of $RbPbI_3$ perovskite nanorod structure via low cost and simple chemical route.

- To examine the non-linear optical natures for $RbPbI_3$ perovskite material.

- To determine nonlinear refractive index and third order susceptibility for $RbPbI_3$ perovskite nanorod material via SSPM method.

1.6. Orientation of Thesis:

This thesis contains six chapters, of which two chapters (Chapters 4, 5) comprise the main body. Chapter 1, has discussed a general introduction to titanium dioxide crystal structures, properties and applications with the extensive introduction of $RbPbI_3$ material with the SSPM technique. Chapter 2 contains a comprehensive literature review of the present status of research, applications and technological advancement in TiO_2 nanomaterial-based memory device field and the SSPM technique in nonlinear optics. Chapter 3 is a general introduction to the crucial experimental apparatus and characterization instruments used in the present thesis. The research outcomes and findings are presented thoroughly in Chapters 4 and 5. In Chapter 4, the research focuses on the synthesis, characterization and resistive switching with synaptic studies of TiO_2-based synthesized devices. An artificial vision system working model was examined using the best TiO_2 device with machine learning approaches in chapter 4. Chapter 5 focuses on the synthesis process and basic characterizations of $RbPbI_3$ perovskite nanorod material. Furthermore, $RbPbI_3$ nanorod material's nonlinear refractive index (n_2) and third-order susceptibility ($\chi^{(3)}$) were determined for the first time. Finally, Chapter 8 concludes each independent work and discusses the possible prospects for future prospects in these areas.

1.7. References:

[1] Feynman, R.P., There is plenty of room at the bottom, Eng. Sci. 23 (1960), pp. 22-36.

[2] www.nsf.gov/home/crssprgm/nano/nsfnnireports.htm (2000)

[3] Chattopadhyay, K.K., Banerjee, A.N., Introduction to Nanoscience and Nanotechnology, PHI Learning, 2012, pp. 1-5.

[4] P. Motiarty, Rep. Prog. Phys., 64 (2001) pp. 297.

[5] J. H. Davies, "The Physics of Low-Dimensional Semiconductors", Cambridge University Press, Cambridge, (1998).

[6] L. Jacak, P. Haweylak and A. Wójs, Quantum Dots, Spriger, (1998) pp. 20.

[7] A.R. Khataee and M.B. Kasiri, Journal of Molecular Catalysis A: Chemical, 328 (2010) pp. 8–26

[8] Ali I, Suhail M, Alothman ZA, Alwarthan A. Recent advances in syntheses, properties and applications of TiO2 nanostructures. RSC Advances. 2018;8:30125-30147

[9] Grätzel M, Rotzinger FP. The influence of the crystal lattice structure on the conduction band energy of oxides of titanium(IV). Chemical Physics Letters. 1985;118:474

[10] Forro L, Chauvet O, Emin D, Zuppiroli L, Berger H, Lévy F. High mobility n-type charge carriers in large single crystals of anatase (TiO2). Journal of Applied Physics. 1994;75:633 [11] National Center for Biotechnology Information. PubChem Compound Summary for CID 26042, Titanium dioxide. https://pubchem.ncbi.nlm.nih.gov/compound/Titanium-dioxide. Accessed June 7, 2022.

[12] Ludvik Martinuand Daniel Poitras, J. Vac. Sci. Technol. A, 18 (2000)pp. 2619.

[13] D. Gong, C. A. Grimes, O. K. Varghese, W. Hu, R. S. Singh, Z. Chen and E. C. Dickey,J. Mater. Res.,16 (2001) pp.3331.

[14] S. Zhang, L.-M. Peng, Q. Chen, G. H. Du, G. Dawson and W. Z. Zhou, Phys. Rev. Lett., 91 (2003) pp.256103.

[15] Z. R. R. Tian, J. A. Voigt, J. Liu, B. Mckenzie and H. F. Xu,J. Am.Chem. Soc.,125 (2003)pp. 12384–12385.

[16] X.H. Li, W.M. Liu and H.L. Li, Appl. Phys. A-Mater. Sci. Process.,80 (2005) pp. 317–320.

[17] J. M. Macăk, H. Tsuchiya, A. Ghicov and P. Schmuki, Electrochem. Comm., 7 (2005) pp. 1133–1137.

[18] Zhao, X.; Xu, H.; Wang, Z.; Lin, Y.; Liu, Y., Memristors with Organic-Inorganic Halide Perovskites. *InfoMat* **2019,** *1* (2), 183-210.

[19] Jung, M.-H.; Rhim, S. H.; Moon, D., TiO2/RbPbI3 Halide Perovskite Solar Cells. *Solar Energy Materials and Solar Cells* **2017,** *172*, 44-54.

[20] Dastidar, S.; Egger, D. A.; Tan, L. Z.; Cromer, S. B.; Dillon, A. D.; Liu, S.; Kronik, L.; Rappe, A. M.; Fafarman, A. T., High Chloride Doping Levels Stabilize the Perovskite Phase of Cesium Lead Iodide. *Nano Letters* **2016,** *16* (6), 3563-3570.

[21] Lim, D.-H.; Ramasamy, P.; Kwak, D.-H.; Lee, J.-S., Solution-Phase Synthesis of Rubidium Lead Iodide Orthorhombic Perovskite Nanowires. *Nanotechnology* **2017,** *28* (25), 255601.

[22] Yoo, E.; Lyu, M.; Yun, J.-H.; Kang, C.; Choi, Y.; Wang, L., Bifunctional Resistive Switching Behavior in an Organolead Halide Perovskite Based Ag/CH3NH3PbI3−xClx/FTO Structure. *Journal of Materials Chemistry C* **2016,** *4* (33), 7824-7830.

[23] Yoo, E. J.; Lyu, M.; Yun, J.-H.; Kang, C. J.; Choi, Y. J.; Wang, L., Resistive Switching Behavior in Organic–Inorganic Hybrid CH3NH3PbI3−xClx Perovskite for Resistive Random-Access Memory Devices. *Advanced Materials* **2015,** *27* (40), 6170-6175.

[24] Paul, T.; Chatterjee, B. K.; Maiti, S.; Sarkar, S.; Besra, N.; Das, B. K.; Panigrahi, K. J.; Thakur, S.; Ghorai, U. K.; Chattopadhyay, K. K., Tunable Cathodoluminescence Over the Entire Visible Window from All-Inorganic Perovskite CsPbX3 1D Architecture. *Journal of Materials Chemistry C* **2018,** *6* (13), 3322-3333.

[25] Tongay, S.; Suh, J.; Ataca, C.; Fan, W.; Luce, A.; Kang, J.; Liu, J.; Ko, C.; Raghunathanan, R.; Zhou, J.; Ogletree, D.; Li, J.; Grossman, J.; Wu, J., Defects Activated Photoluminescence in Two-Dimensional Semiconductors: Interplay Between Bound, Charged, and Free Excitons. *Scientific reports* **2013,** *3*, 2657

[26] Fassl, P.; Zakharko, Y.; Falk, L. M.; Goetz, K. P.; Paulus, F.; Taylor, A. D.; Zaumseil, J.; Vaynzof, Y., Effect of Density of Surface Defects on Photoluminescence Properties in MAPbI3 Perovskite Films. *Journal of Materials Chemistry C* **2019,** *7* (18), 5285-5292.

[27] Liqiang, J.; Yichun, Q.; Baiqi, W.; Shudan, L.; Baojiang, J.; Libin, Y.; Wei, F.; Honggang, F.; Jiazhong, S., Review of Photoluminescence Performance of Nano-Sized Semiconductor Materials and Its Relationships with Photocatalytic Activity. *Solar Energy Materials and Solar Cells* **2006,** *90* (12), 1773- 1787.

[28] Thi Quynh Hoa, T.; Nam, N.; Canh, T.; Nguyen Ngoc, L.; Manh Ha, H., Optical and Photocatalytic Properties of ZnS:Mn Nanocrystals. *e-Journal of Surface Science and Nanotechnology* **2011,** *9*, 516 520.

[29] Li, Y.; Ding, Y.; Zhang, Y.; Qian, Y., Photophysical Properties of ZnS Quantum Dots. *Journal of Physics and Chemistry of Solids* **1999,** *60* (1), 13-15.

[30] Natik, A. *et al.* (2020) "Structural, elastic, electronic and optical properties of RbPbI3perovskites studied using ab-initio calculations," *Phase transitions*, 93(1), pp. 54–61. doi: 10.1080/01411594.2019.1699087.

[31] Nyayban, A. *et al.* (2020) "First principle studies of rubidium lead halides towards photovoltaic application," *Materials today. Communications*, 24(101190), p. 101190. doi: 10.1016/j.mtcomm.2020.101190.

[32] https://materialsproject.org/materials/mp-23517/#xrd-panel.

[33] K. Sk *et al.*, "Nonlinear coherent light–matter interaction in 2D MoSe $_2$ nanoflakes for all-optical switching and logic applications," *Adv. Opt. Mater.*, p. 2200791, 2022.

[34] Chua, L. O. Memristor - the missing circuit element. *IEEE Trans. Circuit Theory* **18**, 507– 519 (1971)

[35] Strukov, D., Snider, G., Stewart, D. *et al.* The missing memristor found. *Nature* **453,** 80–83 (2008). https://doi.org/10.1038/nature06932.

[36] V. Keshmiri, "A Study of the Memristor Models and Applications," Dissertation, 2014.

[37] S. D. Durbin, S. M. Arakelian, Y. R. Shen, *Phys. Rev. Lett.* **1981**, *47*,1411.

[38] R. Wu, Y. Zhang, S. Yan, F. Bian, W. Wang, X. Bai, X. Lu, J. Zhao, E. Wang, *Nano Lett.* **2011**, *11*, 5159.

[39] G. Wang, S. Zhang, F. A. Umran, X. Cheng, N. Dong, D. Coghlan, Y. Cheng, L. Zhang, W. J. Blau, J. Wang, *Appl. Phys. Lett.* **2014**, *4*, 141909.

[40] R. W. Boyd, *Nonlinear Optics*, Academic Press, Cambridge, MA **2020**.

[41] L. Wu, Y. Dong, J. Zhao, D. Ma, W. Huang, Y. Zhang, Y. Wang, X. Jiang, Y. Xiang, J. Li, Y. Feng, J. Xu, H. Zhang, *Adv. Mater.* **2019**, *31*, 1807981.

[42] Y. Shan, L. Wu, Y. Liao, J. Tang, X. Dai, Y. Xiang, *J. Mater. Chem. C* **2019**, *7*, 3811.

Chapter 2

Literature Review
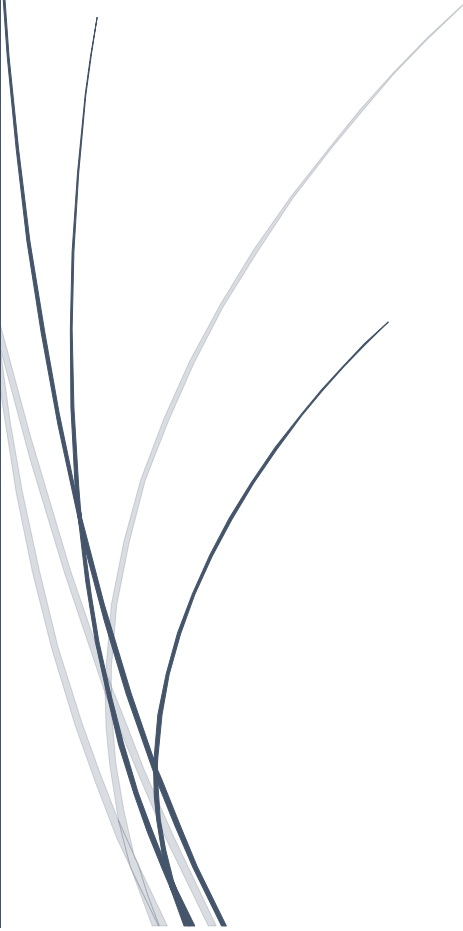
2.1. Literature review for TiO_2 based memristor devices:

Nanostructures represent a unique combination of shape and function, and the properties of these materials can be directly affected by their dimensions. As a result, significant research efforts around the world are focusing on the design and control of novel nanostructures by innovative synthesis strategies. Although the layer thickness approaches the atomic dimension, improved techniques for growing semiconductor thin films with various structural and electronic properties have created new opportunities for basic scientific research and device applications. These new manufacturing techniques have made it possible to reduce the dimensions of devices to the point that quantum size effects play an important role in realistic descriptions of device behaviour and are necessary to reliably predict the performance in electronic and optical applications. Among all transition metal oxides, TiO_2 is certainly the most studied material as it exhibits a wide range of functional properties. TiO_2 powders have traditionally been used as white pigments since ancient times. They are inexpensive, chemically stable, harmless and do not absorb the visible part of electromagnetic radiation spectra. So, they are white. However, the chemical stability of TiO_2 is only preserved in the dark. Instead, it is active under UV radiation and stimulates various chemical reactions. Recently, TiO_2 nanostructured materials with typical dimensions of less than 100 nm have emerged as a product of "quality of life" and is in demand in various parts of the world under the influence of GDP (Gross Domestic Product). In this chapter some of previous important works done by scientists around the world have been discussed.

Here, considering my project work, firstly I would like to enlighten a short review on some aspects of fabrication and device structures and switching mechanism of TiO_2 based memristor devices.

Navaneethan Duraisamy *et al.* reported in 2012; new type of device fabrication process for TiO_2 memristor. [1] The device structure was $Ag/TiO_2/Cu$. Here electrohydrodynamic inkjet printing process applied. TiO_2 active layer deposited by using electrohydrodynamic atomization technique. The electrodes were patterned by electrodynamic printing technique. Anatase TiO_2 present in printed layer with uniform deposition. Bipolar resistive switching observed at operating voltage +0.7 V. the optical transmittance recorded 87% in visible range. Description of synthesis process of TiO_2 nanomaterial illustrated by authors in this report discussed in next. First Titanium isopropoxide (0.96gm/ml) added in ethanol to make a solution. Then stirred for 1 hour at 1000rpm speed. 5ml PVP (0.01gm/ml) added in the solution and again stirred for 20 minutes at 1300 rpm speed. Authors explained the valance charge mechanism responsible for this RS switching.

T. D. Dongale *et al.* first reported fabrication by hydrothermal process of $Ag/TiO_2/Al$ memristor device in 2014. [2] Here anatase TiO_2 with tetragonal structure prepared. Optical reflectance lies between 165-22% of visible region. Here also bipolar resistive switching observed by authors. Here $TiCl_4$ (titanium tetrachloride used as precursors. In hydrothermal process 120 ℃ for 3 hours used. The hydrothermally deposited film annealed at 450 ℃ for 2 hours in ambient condition. Final thickness of thin film was 265nm. Authors achieved high degree of symmetry. Here also authors demonstrated valance charge mechanism only responsible for resistive switching. Valance modification mechanism, oxygen defects, vacancies played the crucial role in this case. [3] Redox reactions both oxidation and reduction took place in TiO_2 active layer interface with metal electrodes. [4] Here oxygen vacancy rich interface acted as a vacancy reservoir. For determining interface electronic barrier work function of metal electrodes give small contributions. [5]

Heeyoung Jeon *et al*. detected oxygen ion drift in their TiO_2 based memristor device. [6] The device structure was $Pt/Al_2O_3/TiO_2/Pt$. here single layer graphene top electrode used for measurement purpose. Single layer graphene served interface free electrode with highly effective indicator for providing O^- ion drift motion in response of electric field in memristor. [7] Here asymmetric resistive switching observed by authors due to redox reactions at interface by O^- ion drift. Endurance of the device improved with increasing the Al_2O_3 layer which provided carrier tunnelling barrier height. Highest endurance was 1800 cycles. Thicknesses of thin film layers were 24nm for TiO_2 layer and 1,3,5 nm for Al_2O_3 layer respectively which were deposited by RPALD method. By Raman and XPS spectroscopy techniques authors described the valance charge mechanism due to oxygen vacancies.

Xian Yang Lin *et al*. reported first Ag cluster doped TiO_2 films for resistive switching and neuromorphic computing.[8] This memristor showed potentiation and depression under consecutive positive and negative pulse trains which represented long term potentiation and long-term depression respectively. The conductance state reached at saturation state due to Hebbian rule. [9] Here Ag cluster ions were mobile ions and migrated from top to bottom electrodes with applied field direction. It was a very low powered device; the power consumption was 26pJ for SET and 22.9pJ for RESET process. This device ideal for low powered electronics applications. [10] authors also successfully employed STM to LTM transition, STDP, PPF, biological synaptic properties in this device.

Shi-Xiang Chen *et al*. demonstrated their RS device $ITO/TiO_2/Pt$ for resistive switching applications.[11] TiO_2 was in amorphous phase in this case that was investigated by TEM

analysis. Bipolar resistive switching observed with 100 times endurance cycles and on/off ratio order of 1. Retention also investigated and recorded 10^4 sec retention time and with 2 order on/off ratio. Here ohmic conduction mechanism happened. SET voltage was 0.6V and RESET voltage was -0.5V respectively which make it a state-of-the-art blow voltage device. Here thermally generated free carriers inside the film contributed in RS switching mechanism. [12-14]

Chi Zhang *et al.* investigated of polymer /nanoparticle interface switching behaviour for TiO_2 nanoparticle with different polymers in 2019. [15] The polymers were PMMA (polymethyl methacrylate), poly (N-vinyl carbazole) (PVK), PFBT, P3HT. authors also studied their influences under mechanical bending conditions. All devices fabricated by vacuum spray deposition technique. The best on/off ratio achieved was 10^3. PFBT shows best endurance upon bending condition. Nanoparticles in polymer may influence stress distribution and NPs dispersion with in film. [16,17] Here switching mechanism associated with field induced tunnelling between adjacent nanoparticles. Polymer molecules served as charge trapping agents. All polymers and TiO_2 nanoparticles mixed in chloroform for solution process with 0.5,0.75,1,1.25,1.5 wt%. the device structure is GaIn/polymer-TiO_2 NP/ITO/PET. On/off ratio was 10^2 that was higher than nanocomposites of other nanoparticles compared to PVK: TiO_2 NPs 1%wt. [18] Due to presence of TiO_2 NPs uniformly in polymer layer, it significantly decreases the band gap of polymer matrix.[19]. By DFT method the interfacial electronic properties were studied for polymer TiO_2 nanoparticle matrix. [20-22]

Yantao Yu *et al.* reported some synthesis process and device structure similar to Au/TiO_2 NR/FTO with different height, diameter, area ratio, oxygen vacancy concentrations 2019. [23] Current of resistive switching behaviour related to oxygen vacancies. Here unipolar switching shown. Here TiO_2 nanorods grown by hydrothermal process with 413K,433K,453K,473K temperatures and 2-hour synthesis time. The grown films were cooled under normal conditions for 120 minutes. Due to faster decomposition rate at higher temperature of titanium butoxide, the length of nanorods increased dramatically. [24-25] Nanorod shapes dependent on solution of hydrothermal process not on substrate used. [26,27] The grown nanorods had rutile phase and contineuous growth took place. Junction surface is created by intertwining of rods by this process electron ways increased. [28,29] Here authors demonstrated current-voltage behaviour by oxygen vacancies and space charge limited current mechanism (SCLC). The nanorods having 3µm or less lengths showed best resistive switching performance. HRS at 10^{-8} A and LRS at 10^{-4} A. electron trapping occurred on the vacancies at the interface between the individual nanorods, and induced the formation of CF for electron mobility. In SCLC, oxygen vacancies act as electron trapping agents which were diffused through the material and start the formation of extra oxygen vacancies under applied electrical field.[30]

Yann Beilliard *et al.* reported the resistive switching and transport mechanism of Al_2O_3/TiO_{2-x} memristor crossbar device with different temperatures in 2020.[31] Authors described switching and transport mechanisms for cryogenic temperatures up to 1.5 K. Total temperature range between 300 – 1.5 K in which phase change mechanism observed and magneli formation (Ti_4O_7) happened. The conductive filaments were made of Ti_4O_7 magneli phases. On/off ratio of 84 observed at cryogenic 1.5 K temperature in selector free cryogenic crossbar device. Here device also showed NDR effect from 130K temperature.

The device structure was Pt/Ti/TiO$_{2-x}$/Al$_2$O$_3$/TiN/SiO$_2$. The growth of conductive filaments during SET process due to migration of oxygen vacancies induced by electric field and thermophoretic forces emerging from local temperature gradients. RESET process as field assisted and temperature activated diffusion of oxygen vacancies leading to the rupture of conductive filaments. Due to this the device switched from LRS to HRS. [32-34]

Carola Ebenhoch *et al.* reported memristor device consisting of TiO$_2$ nanowires grown by simple hydrothermal processing 2021.[35] Authors also examined the main synaptic behaviours like STDP, excitatory post synaptic current, very high endurance and on/off ratios and paired pulse facilitation (PPF) for that device. Authors also examined post synaptic current responses with Kohlrausch's equation. [36-39] By these experimental results they showed lifetime of post synaptic current lies between few milliseconds to some hundred seconds which enabled that device for STP to LTP transition easily. According to this report the polarity of applied test pulses play major role in behaviours of different resistance states. Decaying of negative applied voltage obeyed Kohlrausch's law. The hydrothermal synthesis temperature was 220 ℃ and time was 2 hours. [40] The device structure was Au/TiO$_x$/FTO. Endurance of the device recorded 1000cycles. Three different resistance states were present in the device, they were intermediate low and high resistance states. High resistance states only observed in time dependent measurements not in I-V measurements. Here again oxygen vacancies responsible for forming conductive filaments in active layers. [41-43] By lowering the interface barrier higher conductivity achieved by authors.

Yanmei *et al.* first investigated anodic oxidation time effect on TiO_2 memristor device. [44] Here NDR (negative differential resistance) effect reported on i-v characteristics of memristor. TiO_2 thin film grown on Ti foil by anodic oxidation process. There after Ag/TiO_2/Ti sandwiched structured device constructed. In anodizing process Pt used as counter electrode and Ti foil used as working electrode. 0.25 wt.% NH4F and ethylene glycol used as electrolyte. 60V DC constant voltage applied. Four samples were prepared by 1,3,5,10 min anodizing process. The i-v measurements were done with 0 to ±0.6 v window. The 5 min sample showed very good i-v characteristics. Here electrochemical metallization mechanism happened to corm conductive filaments in TiO_2 active layer.

Yuanmin Du *et al.* reported resistive switching process studied by Kelvin probe force microscopy and conductive atomic force microscopy for TiO_2 thin film memristors. [45] In past works CAFM used for interfacial and conductive filamentary studies in resistive switching process. [46-48] When top electrode removed and AFM tip used as top electrode then MIM memristor also shows resistive switching. Work function mapping achieved by KPFM with high resolution. Distributed defects in oxide or active layer played crucial role in switching behaviour. [49,50] Dislocations provides easy paths for oxygen ion movement. [51,52] Negative oxygen ions injected under negative bias condition also electrons injected in same condition into oxide surface. Here each and every CFs acted as RS unit by redox reactions. Here also valance charge mechanism used to demonstrated resistive switching process.

Au Yan *et al.* reported resistive switching of a crossbar array structured device. The device structure was Au/TiO_2/Au. [53] Width of Au electrodes were 1 μm and TiO_2 layer was

50nm. In voltage controlled electroforming method compliance current (cc) played critical role. Electrical burned out happened when unstable compliance current applied. [54] here bipolar resistive switching observed by authors. The switching process happened due to electroforming. NDR effect also observed in this case. The compliance current was 100mA. Endurance was 1000 cycles and on/off ratio was nearly 10.

Kyung Min Kim *et al.* reported electrical forming methods in TiO_2 based bipolar resistive switching device. [55] The device structure was $Pt/TiO_2/Pt$. here Magneli phase (Ti_nO2_{n-1}) of TiO_2 formed through electroforming and due to this the bipolar resistive switching happened. By varying the compliance current the shape of conductive filaments changed, it caused in different breaking locations. The unipolar switching happened in metal oxide MIM structure due to formation of magneli phase by electrochemical process. 60nm thick metal oxide layer deposited by sputtering technique on the top of Pt/ SiO_2 substrate. NDR (negative differential resistance) effect observed at -0.9 to -1.2V. From the switching layer bottom electrode side asymmetric potential barrier generated. The device went to HRS state empty top electrode switching layer. This time bottom electrode switching layer filled with electrons. Here authors also examined unipolar resistive switching for this device.

Kyung Jean Yoon *et al.* reported first tri stable resistive switching for TiO_2 material. [56] The device structure was $Pt/ TiO_2/ Pt$. tri-stable switching started in the memristor as unipolar RESET. By electroforming process the magneli phases initiated the unipolar reset and then unipolar switching in the device. At the conductive filament ruptured position, the tri stable switching occurred after unipolar reset process happened. Valency assisted mechanism responsible for this kind of switching process authors established the relation.

The thickness of TiO_2 film on Pt substrate was 60 nm which was deposited by plasma enhanced atomic layer deposition method. Pt electrodes were deposited using sputtering techniques. For unipolar switching typical SET voltage range was 1.5-3.5V and same for bipolar switching was 0.5-1.5 V. In this device metallic magneli phase was responsible for conductive filament formation and most of the device current flowed through it alone. Here SET process was bipolar in nature and RESET process was unipolar in nature. SET happened by electroforming process and RESET happened at ruptured region.

Kuyyadi P. Biju *et al.* reported switching properties in TiO_2 resistive switching device. [57] TiO_2 synthesised by sol-gel method. The device structure was Pt/ TiO_2/ W. TiO_2 film deposited on electrode by spin coating technique. Reversible and reproducible resistive switching in the fabricated device observed by authors. The rectifying effect also observed in this device. In low resistance state the rectification ratio was greater than 60 at 2V because top electrode – oxide junction limited the electron injection at opposite field condition. The redox reaction occurred at bottom electrode in transport process. That small rectifying effect caused lower sneak path current. Lower sneak path current is ideal for crossbar array applications. For endurance cycles, 100 cycles reported. On/off current ratio reported was 10^6. And retention up to 10^5 sec.

Xiaofang Hu *et al.* reported negative differential resistance effect in TiO_2 based memristor device. [58] The device structure was Ag/ TiO_2/ FTO. Peak voltage (V_p) / valley voltage (V_v) used to characterise the NDR effect which was n-type NDR. It helped the device to operate at low power. Electron hopping by different valences, temperature dependent magneli phase creation and field generated oxygen valences were collectively responsible

for this n-type NDR effect in that device. SCLC mechanism responsible for migration of electrons in the oxide film from top electrode to bottom electrode. The gap between V_p and V_v was vbery low ~ 0.5V and I_p and I_v was 30mA recorded.

Priyanka Bamola *et al.* reported synthesis of MxPh-TNs (mixed phase TiO_2 nanostructures) for defect study to modifying it for memory device applications. [59] Authors also investigated the interface electronic property changing due to exotic mixed phased TiO_2 hybrids with Pt and Pd electrodes. By electrochemical anodization process TiO_2 nanorods synthesised 1mm thick layer on Ti foil. Anodizing voltage was 40V and time was 2hours. For mixed phased synthesis hydrothermal processed was adopted. The hydrothermal temperature was 500 ºC and duration was 1 hour. The three devices were fabricated e.g; Al/Pd−Pt/MX-TNHs/Ti , Al/MxPh-TNs/Ti, and Al/ Pt/MX-TNHs/Ti. MxPh-TNs had oxygen defects in large amount. These oxygen defects acted as electron trapping agents and trapped electron for space charge limited current and supports the switching phenomenon. MX-TNHs don't had good amount of oxygen vacancies they formed filaments in the inside surface of TiO_2 nanotubes. Al used as top electrode and being active metal, the electrochemical reactions occurred at interfaces. For these two devices Al/Pd−Pt/MX-TNHs/Ti and Al/ Pt/MX-TNHs/Ti the on current and off currents were I_{ON} (2.14×10^{-5} A) and I_{OFF} (7.13×10^{-5} A) at 3 V and I_{ON} (2.13×10^{-3} A) and I_{OFF} 6.77×10^{-4} A) at 3 V, respectively.

Guangdong Zhou *et al.* first reported three different memristor evolution stages in their TiO_2 nanobelt memristor. [60] The three memristor stages were non-standard faradic capacitance (NFC), resistive switching (RS), transition stage or battery like capacitance

stage (BLC). The device structure was Ag/ TiO_2 nanobelt / Ti. The all measurements were done under different moisture conditions. At ambient condition generation and migration and recombination of ions and electrons like charge carriers were restricted for NFC type case. Under moisture condition device switched from NFC to BCL stage due to water based redox reactions, OH- ions captured by Vo vacancies. In RS stage the interaction between ions and vacancies were very prominent and for these reasons device switch to HRS to LRS state. B y this work it was clearly observed by the authors that the significance of moisture in the memristor devices. After exceeding the moisture value 35-40% the NFC evolves BLC and for moisture grange 95-99% BLC evolves in RS. By DFT analysis it was shown that how the energy band structure modulated in TiO_2 layer.

2.2. Literature review for RbPbI$_3$ nanorods used in memory device application and fundamental physical properties of RbPbI$_3$ nanorods:

As already discussed in previous chapter, previous works based on RbPbI$_3$ in resistive switching device applications have been explored in this section. RbPbI$_3$ is purely insulating in pristine state. In this section, I have tried to discuss the modifications done for resistive switching and photoelectronic solar cell application for RbPbI$_3$ in the past works. In this segment, I have focussed on reviewing the important phenomenological effects and applications of RbPbI$_3$ which were studied in past by various scientists.

Ujjal Das *et al.* reported an important measure in resistive switching behaviour upon composite perovskite-based device. [61] Here authors used the perovskite called RbPbI$_3$ with Cl (halide) mixing for their experiment. Authors synthesised all inorganic RbPbI$_3$ with

and without Cl doping as nanorod. To construct resistive switching device perovskite nanorods used with PMMA (poly methyl methacrylate). Pure perovskite device did not show resistive switching behaviour in spite of insulating nature. Two different broad classification of fabricated devices were a) $RbPbI_3$ @ PMMA (1,2,4,6,8 % conc. of PNR) and b) $RbPbI_{2.4}Cl_{0.6}$ @PMMA (1,2,4,6,8% of PNR). Embedded PNRs in polymer composite acted as charge trapping entities and transporting medium and polymer as blocking medium. 1%, 2% devices did not show RS behaviour but 4%, 6%, 8% devices showed good RS behaviours. So, higher concentration of PNR showed higher switching behaviour. Here authors also investigated and described the compatibility of multilabel programming for different values of compliance currents for 4% device. Cl doped 6% device exhibits higher on/off ratio and lower operating voltage. Also 4% device exhibits higher stability of 14 days from fabrication day.

Ujjal Das *et al.* reported filamentary resistive switching device based on perovskite by induced vacancy-oriented method. [62] In this report inorganic $RbPbI_3$ perovskite material doped with Cl in the X_3 Side. This modification introduced because of pure $RbPbI_3$ not switchable. Five different devices were fabricated like $RbPbI_{3-x}Cl_x$ (x= 0,0.3,0.6,0.9,1.2). 20% chloride-based device showed best results, in the sense of high on/off current ratio, large endurance, long retention, etc. Here switching happened based on iodine vacancy mediated CF growth mechanism. This was established with the help of CAFM. Higher Cl concentration increased more defects for that reason Ag CFs were constructed in later devices. So, metal filamentary switching and vacancy mediated switching mechanisms were contributed in this case.

Sang Myeong Lee *et al.* reported resistive switching phenomenon of methylammonium lead iodide (MAPbI$_3$) and RbPbI$_3$ composite mixture. [63] Authors fabricated five different devices based on composition of two halide perovskites (Rb$_{1-x}$MA$_x$PbI$_3$; x= 0,0.31,0.52,0.72,1). The composite memristor devices were showed very good resistive switching characteristics with 10^6 on/off current ratio, 10^3 cycles endurance and operation speed of 640 µs. Electrochemical metallization mechanism was responsible for resistive switching in this case. The device structure was Ag/ Rb$_{1-x}$MA$_x$PbI$_3$ / Pt/Si. Electrochemical metallization mechanism was based on migration of metals which were electrochemically active and formed conductive filaments. By applying external field Ag cation dissolved in active layer and filament formation occurred between TE and BE. Due to this process the resistance decreased and device switched from HRS to LRS. This was SET process. RESET process occurred when opposite electric field applied between tow electrodes. Immolating RbPbI$_3$ resisted the CF formation due to this reason device endurance was proportional to the concentration of halide perovskite. Here non switchable RbPbI$_3$ enhanced the endurance of the device.

Mi-Hee Jung *et al.* reported an oxide halide perovskite solar cell where RbpbI$_3$ used as HP and TiO$_2$ used as oxide material. The device structure was FTO/TiO$_2$/RbPbI$_3$/Spiro-MeOTAD/Au. [64] Highest stability of inorganic RbPbI3 in ambient terms noted in this device. The open circuit voltage of 0.62V, photocurrent density of 3.25mA/cm2, fill factor 44.60% and PLE of 1.04% reported for this device in reverse sweeping direction. This study mainly focused to developed high stability halide perovskite photovoltaic device for day-to-day applications in atmospheric terms.

Jong Soo Lee *et al.* first reported the synthesis process of RbPbI$_3$ nanowires in 2017 as an alternative of CsPbX$_3$ perovskite. RbPbI$_3$ was single crystalline and orthorhombic structured. [65] First synthesized nanowires had diameters around 30-32 nm and lengths up to few micrometres. That perovskite also could absorb 450nm optical illuminance which described its good optoelectronic properties. In synthesis process first 0.188 mmol of RbI$_2$, 5ml ODI, 0.5ml OAM and 0.5ml OA were loaded into a three-neck flask and dried under vacuum for 1h at 120 ℃. the temperature raised to 150 ℃ with N$_2$. Then 1ml Rb-oleate solution quickly added and maintained at that temperature for 30 minutes. Then mixture was cooled down at room temperature and nanowires were precipitated using ethanol and centrifuged at 3500 rpm for 3 minutes. The last solid was redispersed in chloroform. To collect RbPbI$_3$ nanowires as yellow solid. By UV- vis spectroscopy it was observed that the bandgap energy was 2.88 eV. Authors also fabricated a photodetector device to investigate the photo responses.

B. Indrajit Sharma *et al.* first reported the principal calculations with Fp-LAPW method for optoelectronic and transport property study of RbPbX$_3$ (I, Cl, Br). [66] In RbPbI$_3$ the reduced effective mass indicated that it was efficient for charge carrier transport compare to others. Authors also proved experimentally that excitons for RbPbI3 was Mott-Wannier type. For 500nm thick solar cell fabricated with RbPbI$_3$ exhibited 11.59% of SLME (spectroscopic limited maximum efficiency). By electronic band structure calculation authors reported 2.45eV band gap for RbPbI$_3$. Estimated values for band gap positions were -3.7 eV for conduction band and -6.1 eV for valance band.

K Deepthi Jayan *et al.* reported first principle DFT (Density Function Theory) study for investigate various properties of perovskite solar cell at individual layer level. [67] In this paper authors described some DFT functionalities of perovskite solar cell for structural, optical, electronic properties by VASP, WIEN2K software packages. Band gap relaxation time of holes and electrons, visible light absorption, change of these electronic properties due to doping analysed by DFT method. Impact of different types of intrinsic defects in perovskite structure also examined by above said softwires and methods.

Carmen Abia *et al.* reported structural features of $RbPbI_3$ for solar cell applications. Authors synthesized $RbPbI_3$ halide perovskite nanorods using mechano chemical process with green measures, avoiding harmful chemicals. [68] The relative covalency of Rb-I versus Pb-I bonds showed that the Pb-I related vibrations are more rigid than Rb-I related vibrations. These seen i9n Debye temperature from evolution of the anisotropic displacements. The band gap measured was 2.51 eV by UV-Vis reflectance spectroscopy. Authors also reported that thermoelectric Seebeck coefficient was around in third order on magnitude which was larger than other halide perovskites.

2.3. Literature Review for Determination of Non-linear Refractive Index (n_2) and Third Order Susceptibility ($\chi^{(3)}$) via Spatial Self Phased Modulation (SSPM) Technique:

The terminology Spatial Self-Phase Modulation (SSPM) refers to the phase modulation of an optical field traveling through an optical medium caused by the spatial distribution of the applied intensity and the optical medium's unique nonlinear refractive index. [69] Due

to the coherent superposition of transverse wave vectors with spatially modulated optical phases caused by the characteristic nonlinear refractive index of the optical medium and the spatially distributed intensity of the Gaussian beam, the SSPM of Gaussian beam in the nonlinear optical material exhibits the optical concentric diffraction rings at the far-field. According to the even or odd-integer difference of the nonlinear phase shift, which is regulated by the nonlinear refraction coefficient and the input intensity. Nonlinear refractive index (n_2) is the change in refractive index of the material or medium and is proportional to the incident light intensity. It is denoted by n_2. By intensity dependent SSPM we calculated third order nonlinear susceptibility ($\chi^{(3)}$) and nonlinear refractive index. Many halide perovskites have been used to determine the nonlinear optical properties of those materials by researchers worldwide but there is no report of $RbPBI_3$ in this regard best to our knowledge. So, this is a novel work of its kind for this perovskite to determine the nonlinear optical refractive index (n_2) with different solvents and also nonlinear third order susceptibility ($\chi^{(3)}$). In this segment past works done by various researchers on SSPM technique have been reviewed briefly.

Bingxin Shi *et al.* reported SSPM study on Bi_2Se_3 topological insulator and determined the nonlinear refractive index and third order susceptibility first time. [70] A practical solvothermal approach was used to create homogeneous hexagonal nanostructured ultrathin topological insulator bismuth telluride (Bi_2Te_3) nanosheets. With 400 nm, 800 nm, and 1070 nm ultrafast lasers, broad-band spatial self-phase modulation features of these topological insulator nanosheets have been discovered. According to the experimental findings, the broadband, ultrafast, and significant third-order optical nonlinearity of Bi_2Te_3 is what causes this coherent light scattering. The nonlinear refractive index (n_2) of the Bi_2Te_3 dispersion solution was measured to be ~ 10^{-12} m2/W under pulsed

laser stimulation, and the third-order nonlinear susceptibility was ~10^{-7} esu. Our study could pave the way for the creation of topological insulator-based nonlinear optical applications.

Xiaohong Li *et al.* reported SSPM experiment to determination of NLO parameters by using Bi_2Se_3 2D material. [71] By altering the incidence intensity of the controlling light, it was possible to adjust the spatial phase of controlled light as three phases (unchanging, focussing, and diffraction) using a sample of Bi_2Se_3 nanosheets dispersion solution. According to the proposed mechanism, the controlling light modifies the phase distribution of the overlapped region before changing that of the controlled light. The phase distribution of the controlling light and controlled light was recovered from the transmitted patterns using the Gerchberg-Saxton algorithm. The three processes of self-focusing, self-diffraction ring generation, and self-diffraction ring deformation can all be seen in a dynamic spatial self-phase modulation (SSPM) experiment. Additionally, it was shown that this all-optical switching was feasible in a broad wavelength range by measuring the SSPM of controlling light at the typical wavelengths of 350 nm to 1160 nm. These findings demonstrate Bi_2Se_3's enormous potential as an all-optical switching material for a range of optoelectronic applications. The values of n_2 and $\chi^{(3)}$ was around ~10^{-9} and ~10^{-3} esu.

Leiming Wu *et al.* reported as an analogue compound of black phosphorus, a new 2D semiconducting few-layer SnS is successfully synthesized, and its nonlinear optical response was examined. [72] It was demonstrated that the material's third order nonlinear susceptibility and nonlinear refractive index are measured as $n_2 \sim 10^{-5}$ (cm2 W^{-1}) and $\chi^{(3)}$ monolayer 10^{-10} (e.s.u.), respectively. By modulating the propagation of the signal beam by another controlling beam, an all-optical switching mechanism based on few-layer SnS was

realised by taking use of the large Kerr nonlinearity. The development of few-layer SnS as an excellent optical material for all-optical signal processing is suggested by the success of all-optical switching.

Youxian Shan *et al.* demonstrated the SSPM experiment with Graphene oxide and also all optical switching done for the same. [73] Liquid-phase exfoliation is successfully used to create few-layer graphene oxide (GO) dispersions. By using spatial self-phase modulation (SSPM) studies, the nonlinear optical response of GO is examined. Third-order nonlinear susceptibility and nonlinear refractive index of GO are measured as $n_2 = 3.57 \times 10^{-6} \, cm^2/W$ and $\chi^{(3)} \sim 6.05 \times 10^{-10}$ (e.s.u.). Additionally, by using cross-phase modulation and these GO dispersions, they created an all-optical switching light route. The device's operating principle was to modulate the signal light's propagation by altering the strength of the controlling laser beam. These intriguing characteristics point to GO's possible use in novel optical switching devices, optical modulators, detectors, etc.

Gaozhong Wang *et al.* described the calculation of nonlinear refractive index for MoS_2, WS_2, $MoSe_2$ nanosheets and comparison between all in this study. [74] In cyclohexyl pyrrolidone, layered MoS_2, WS_2, and $MoSe_2$ nanosheets were created using liquid-phase exfoliation technology. Through the use of a 488 nm continuous wave laser beam, spatial self-phase modulation (SSPM) was used to study the nonlinear optical response of these nanosheets in dispersions. Right after the laser traversed the nanosheet dispersions, it was discovered that the SSPM diffraction ring patterns were deformed vertically. The third-order nonlinear susceptibility was found to be $\chi^{(3)} 10^{-9}$ e.s.u., and the nonlinear refractive index of the three-transition metal dichalcogenides dispersions was measured to be 10^{-7} $cm^2 \, W^{-1}$. By altering the incident intensities, it is possible to modify the effective nonlinear

refractive index of the MoS_2, WS_2, and $MoSe_2$ dispersions by 0.012–0.240, 0.029–0.154, and 0.091-0.304, respectively. These experimental results suggest that a fresh potential use for two-dimensional transition metal dichalcogenides in nonlinear phase manipulation apparatuses.

Ana B Villafranca *et al.* reported SSPM study by using photopolymerizable organ siloxane media. [75] In a photopolymerizable organ siloxane media, diffraction rings caused by spatial self-phase modulation of a continuous wave, visible laser beam were detected. Self-phase modulation results from changes in the medium's refractive index brought on by free-radical polymerization that was initiated by the laser. This work focuses on the variations in photo response of the organ siloxane in comparison to other nonlinear optical materials and the chances they present to investigate hitherto unreachable self-induced diffraction ring features. In particular, the organ siloxane's non instantaneous response allowed diffraction rings to move across the medium over large distances (>> Rayleigh length) without being impeded by optical self-focusing. Additionally, it was feasible to keep track of the rings' temporal development and thereby acquire a first-hand understanding of the dynamics of self-phase modulation. The conical trajectory of the diffraction rings through the medium was directly visible thanks to the persistent changes in refractive index brought on by polymerization.

Jie Li *et al.* carried out experimental research on the MXene $Ti_3C_2T_x$ (T=O, OH, or F) ultrafast responsiveness and broadband spatial self-phase modulation (SSPM). [76] The MXene $Ti_3C_2T_x$ displayed ultrafast carrier properties with an ultrafast recovery time using femtosecond transient absorption spectroscopy, as well as a broadband nonlinear optical response through SSPM from 400 nm to about 1 m under the ultrafast laser stimulation.

According to the experimental findings, MXenes exhibited a broad nonlinear optical response, which pave the way for the development of ultrafast optoelectronic devices based on MXenes.

Qian Zhang *et al.* characterized the performance of optical limiting by self-phase modulation (SSPM) in hot atomic vapor cell. [77] The outcomes showed that the position of the sample cell, which was governed by the Rayleigh length of the beam, was highly related to the performance of the optical limiter. The sample position at 10 mm from the coordinate origin yielded the lowest limiting threshold and clamp output (the beam waist). The theory of SSPM and z-scan, which were induced by both the Kerr effect and the thermal optical nonlinearity, provided a clear explanation for the occurrence. Finding the ideal location for the sample cell in the optical limiter and other SPM applications was one of the useful insights gained from this work.

Amir Reza Sadrolhosseini *et al.* reported for the purpose of demonstrating the nonlinear features of nanocomposites, the spatial self-phase modulation effect in graphene oxide with silver and gold nanoparticles was taken into consideration. [78] Different times of laser ablation were used to create gold and silver nanoparticles in graphene oxide. X-ray diffraction spectroscopy, transmission electron microscopy, and UV-visible spectroscopy were used to characterise the produced samples. The blue and green absorption peaks were related to silver and gold nanoparticles, and the nanoparticles were capped by spherical graphene oxide. As the ablation period was extended, the nanoparticle concentration rose. The spatial self-phase modulation technique was then used at 532 and 405 nm wavelengths to study the nonlinear effect in graphene oxide and graphene oxide containing gold and silver nanoparticles. At various intervals between 5 and 35 minutes, laser ablation was used

to create silver and gold nanoparticles. With an increase in ablation time, nanoparticle concentration rose, and they took on a spherical shape in the GO. As a result, the presence of Au-NPs and Ag-NPs in Go caused a negative change in refractive index, the appearance of a negative lens, and an increase in the nonlinearity effect with increasing nanoparticle volume percent. The self-defocusing effect consequently manifested in the aforementioned medium, and the quantity of spatial self-phase modulation rings increased with a corresponding rise in nanoparticle volume percentage.

R Karimzadeh *et al.* described the findings of theoretical and experimental studies of diffraction ring patterns. [79] A continuous wave laser beam travelling through a dye solution in ethanol causes self-phase modulation, which results in the formation of diffraction rings. The changes in the sample's refractive index brought on by the sample being heated by a small amount of laser energy that was absorbed which caused the laser beam to self-phase modulate. Authors had solved the heat transfer equation incorporating conduction and convection effects in a liquid medium in order to identify the thermal nonlinearity within the liquid exposed to a Gaussian laser beam. On the basis of a Fresnel-Kirchhoff diffraction integral in the approximation of an optically thin absorbing medium, the temporal dynamics and structural properties of the diffraction ring patterns were theoretically investigated. According to the simulation results, when a Gaussian laser beam passes through liquid, the intensity distribution pattern in the far field initially formed a sequence of circular diffraction rings, but with time, due to convection, the rings alter to have half-circular symmetry.

2.4. Reference:

[1] Navaneethan Duraisamy, Nauman Malik Muhammad, Hyung-Chan Kim, Jeong-Dai Jo, Kyung-Hyun Choi, Fabrication of TiO2 thin film memristor device using electrohydrodynamic inkjet printing, Thin Solid Films, Volume 520, Issue 15, 2012, Pages 5070-5074.

[2] T.D. Dongale, S.S. Shinde, R.K. Kamat, K.Y. Rajpure, Nanostructured TiO2 thin film memristor using hydrothermal process, Journal of Alloys and Compounds, Volume 593, 2014, Pages 267-270.

[3] R. Waser, Microelectron. Eng. 86 (2009) 1925.

[4] N. Duraisamy, N.M. Muhammad, H.C. Kim, J.D. Jo, K.H. Choi, Thin Solid Films 520 (2012) 5070–5074.

[5] J.J. Yang, J.P. Strachan, F. Miao, M.X. Zhang, M.D. Pickett, W. Yi, A.A. Douglas, G. Ohlberg, R. Medeiros-Ribeiro, W. Stanley, Appl. Phys. A 102 (2011) 785–789.

[6] Heeyoung Jeon, Jingyu Park, Woochool Jang, Hyunjung Kim, Seungbae Ahn, Ki-Joon Jeon, Hyungtak Seo, Hyeongtag Jeon, Detection of oxygen ion drift in Pt/Al2O3/TiO2/Pt RRAM using interface-free single-layer graphene electrodes, Carbon, Volume 75, 2014, Pages 209-216.

[7] Chen S, Brown L, Levendorf M, Cai W, Ju S-Y, Edgeworth J, et al.. Oxidation resistance of graphene-coated Cu and Cu/Ni alloy. ACS Nano 2011;5(2):1321–7.

[8] Yan, X. B., Zhao, J. H., Liu, S., Zhou, Z. Y., Liu, Q., Chen, J. S., Liu, X. Y., *Adv. Funct. Mater.* 2018, 28, 1705320. https://doi.org/10.1002/adfm.201705320

[9] S. Martin, P. Grimwood, R. Morris, *Annu. Rev. Neurosci.* **2000**, *23*, 649.

[10] P. A. Merolla, J. V. Arthur, R. Alvarez-Icaza, A. S. Cassidy, J. Sawada, F. Akopyan, B. L. Jackson, N. Imam, C. Guo, Y. Nakamura, B. Brezzo, I. Vo, S. K. Esser, R. Appuswamy, B. Taba, A. Amir, M. D. Flickner, W. P. Risk, R. Manohar, D. S. Modha, *Science* **2014**, *345*, 668.

[11] Shi-Xiang Chen *et al.* 2018 *ECS J. Solid State Sci. Technol.* **7** Q3183

[12] F. C. Chiu, P. W. Li, and W. Y. Chang, *Nanoscale res. let.*, **7**(1), 178 (2012).

[13] R. Waser, R. Dittmann, G. Staikov, and K. Szot, *Adv. Mater.*, **21**(25), 2632 (2009).

[14] J. J. Yang, M. D. Pickett, X. Li, D. A. Ohlberg, D. R. Stewart, and R. S. Williams, *Nat. nanotechnol.*, **3**(7), 429 (2008).

[15] Chi Zhang, Pei-Lun Yu, Yue Li, Jian-Chang Li, Polymer/TiO2 Nanoparticles interfacial effects on resistive switching under mechanical strain, Organic Electronics, Volume 77, 2020,
105528, ISSN 1566-1199.

[16] A. Chatterjee, M.S. Islam, Fabrication and characterization of TiO(2)-epoxy nanocomposite, Mater. Sci. Eng. A 487 (2008) 574–585, https://doi.org/10.1016/ j. msea.2007.11.052.

[17] A. Laiho, H.S. Majumdar, J.K. Baral, F. Jansson, R. Osterbacka, O. Ikkala, Tuning the electrical switching of polymer/fullerene nanocomposite thin film devices by control of morphology, Appl. Phys. Lett. 93 (2008), https://doi.org/10.1063/ 1.3033221, 203309.

[18] B. Cho, T.W. Kim, M. Choe, G. Wang, S. Song, T. Lee, Unipolar nonvolatile memory devices with composites of poly(9-vinylcarbazole) and titanium dioxide nanoparticles, Org. Electron. 10 (2009) 473–477, https://doi.org/10.1016/j. orgel.2009.02.001.

[19] J. Kang, F.M. Wu, J.B. Li, Modulating the bandgaps of graphdiyne nanoribbons by transverse electric fields, J. Phys. 24 (2012), https://doi.org/10.1088/0953-8984/24/16/165301, 165301.

[20] Z.L. Tseng, P.C. Kao, M.F. Shih, H.H. Huang, J.Y. Wang, S.Y. Chu, Electrical bistability in hybrid ZnO nanorod/polymethylmethacrylate heterostructures, Appl. Phys. Lett. 97 (2010), https://doi.org/10.1063/1.3511756, 212103.

[21] J.D. Yang, S.H. Cho, T.W. Hong, D.I. Son, D.H. Park, K.H. Yoo, W.K. Choi, Organic photovoltaic cells fabricated on a SnOx/Ag/SnOx multilayer transparent conducting electrode, Thin Solid Films 520 (2012) 6215–6220, https://doi.org/10.1016/j.tsf.2012.05.029.

[22] Q.D. Ling, Y. Song, S.L. Lim, E.Y.H. Teo, Y.P. Tan, C.X. Zhu, D.S.H. Chan, D. L. Kwong, E.T. Kang, K.G. Neoh, A dynamic random access memory based on a conjugated copolymer containing electron-donor and -acceptor moieties, Angew. Chem. 45 (2006) 2947–2951, https://doi.org/10.1002/anie.200504365.

[23] Yantao Yu, Chunqi Wang, Chao Jiang, Isaac Abrahams, Zuojuan Du, Qiancheng Zhang, Jia Sun, Xiaozhong Huang, Resistive switching behaviour in memristors with TiO2 nanorod arrays of different dimensions, Applied Surface Science, Volume 485, 2019, Pages 222-229, ISSN 0169-4332.

[24] E. Hosono, S. Fujihara, K. Kakiuchi, H. Imai, Growth of submicrometer-scale rectangular parallelepiped rutile TiO2 films in aqueous TiCl3 solutions under hydrothermal conditions, J. Am. Chem. Soc. 106 (2004) 7790–7791.

[25] J. Yu, G. Wang, B. Cheng, M. Zhou, Effects of hydrothermal temperature and time on the photocatalytic activity and microstructures of bimodal mesoporous TiO2 powders, Appl. Catal., B 69 (2007) 171–180.

[26] X. Feng, K. Shankar, O.K. Varghese, M. Paulose, T.J. Latempa, C.A. Grimes, Vertically aligned single crystal TiO2 nanowire arrays grown directly on transparent conducting oxide coated glass: synthesis details and applications, Nano Lett. 8 (2008) 3781–3786.

[27] X. Feng, K. Zhu, A.J. Frank, C.A. Grimes, T.E. Mallouk, Rapid charge transport in dye-sensitized solar cells made from vertically aligned single-crystal rutile TiO2 nanowires, Angew. Chem. 124 (2012) 2781–2784.

[28] Z. Wei, Y. Yao, T. Huang, A. Yu, Solvothermal growth of well-aligned TiO2 nanowire arrays for dye-sensitized solar cell: dependence of morphology and vertical orientation upon substrate pretreatment, Int. J. Electrochem. Sci. 6 (2011) 1871–1879.

[29] Y. Zhang, C. Han, G. Zhang, D.D. Dionysiou, M.N. Nadagouda, PEG-assisted synthesis of crystal TiO2 nanowires with high specific surface area for enhanced photocatalytic degradation of atrazine, Chem. Eng. J. 268 (2015) 170–179.

[30] X.W. He, Y.L. Yin, J. Guo, H.J. Yuan, Y.H. Peng, Y. Zhou, D. Zhao, K. Hai, W.C. Zhou, D.S. Tang, Memristive properties of hexagonal WO3 nanowires induced by oxygen vacancy migration, Nanoscale Res. Lett. 8 (2013).

[31] Yann Beilliard, François Paquette, Frédéric Brousseau, Serge Ecoffey, Fabien Alibart, *and* Dominique Drouin , "Investigation of resistive switching and transport mechanisms of Al_2O_3/TiO_{2-x} memristors under cryogenic conditions (1.5 K)", AIP Advances 10, 025305 (2020) https://doi.org/10.1063/1.5140994

[32] J. S. Lee, S. Lee, and T. W. Noh, Appl. Phys. Rev. **2**, 031303 (2015).

[33] D. Ielmini, F. Nardi, and C. Cagli, Nanotechnology **22**, 254022 (2011).

[34] D. Ielmini, Semicond. Sci. Technol. **31**, 063002 (2016).

[35] Ebenhoch, C., Schmidt-Mende, L., TiO$_2$ Nanowire Array Memristive Devices Emulating Functionalities of Biological Synapses. *Adv. Electron. Mater.* 2021, 7, 2000950. https://doi.org/10.1002/aelm.202000950

[36] R. Kohlrausch, *Ann. Phys.* **1854**, *167*, 179.

[37] H. Scher, M. F. Shlesinger, J. T. Bendler, *Phys. Today* **1991**, *44*, 26.

[38] D. C. Elton, *arXiv:1808.00881* **2018**.

[39] J. Klafter, M. F. Shlesinger, *Proc. Natl. Acad. Sci. U. S. A.* **1986**, *83*,848.

[40] J. Kalb, A. Folger, C. Scheu, L. Schmidt-Mende, *J. Cryst. Growth* **2019**, *511*, 8.

[41] R. Waser, M. Aono, *Nat. Mater.* **2007**, *6*, 833.

[42] R. Waser, R. Dittmann, G. Staikov, K. Szot, *Adv. Mater.* **2009**, *21*, 2632.

[43] V. Aglieri, A. Zaffora, G. Lullo, M. Santamaria, F. Di Franco, U. Lo Cicero, M. Mosca, R. Macaluso, *Superlattices Microstruct.* **2018**, *113*, 135.

[44] Yanmei Yu, Feng Yang, Shuangsuo Mao, Shouhui Zhu, Yongfang Jia, Ling Yuan, Mayameen Salmen, Bai Sun, Effect of anodic oxidation time on resistive switching memory behavior based on amorphous TiO2 thin films device, Chemical Physics Letters, Volume 706, 2018, Pages 477-482, ISSN 0009-2614.

[45] Yuanmin Du, Amit Kumar, Hui Pan, Kaiyang Zeng, Shijie Wang, Ping Yang, and Andrew Thye Shen Wee, "The resistive switching in TiO2 films studied by conductive atomic force microscopy and Kelvin probe force microscopy", AIP Advances 3, 082107 (2013) https://doi.org/10.1063/1.4818119.

[46] B. J. Choi, D. S. Jeong, S. K. Kim, C. Rohde, S. Choi, J. H. Oh, H. J. Kim, C. S. Hwang, K. Szot, R. Waser *et al.*, J. Appl. Phys. **98**, 033715 (2005).

[47] R. Muenstermann, T. Menke, R. Dittmann, and R. Waser, Adv. Mater. **22**, 4819 (2010).

[48] L. Yang, C. Kuegeler, K. Szot, A. Ruediger, and R. Waser, Appl. Phys. Lett. **95**, 013109 (2009).

[49] K. Shibuya, R. Dittmann, S. B. Mi, and R. Waser, Adv. Mater. **22**, 411 (2010).

[50] J. Y. Ye, Y. Q. Li, J. Gao, H. Y. Peng, S. X. Wu, and T. Wu, Appl. Phys. Lett. **97**, 132108 (2010).

[51] K. Szot, W. Speier, R. Carius, U. Zastrow, and W. Beyer, Phys. Rev. Lett. **88**, 075508 (2002).

[52] J. Philibert, *Atom Movements — Diffusion and Mass Transport in Solids* (Editions de Physique, 1991).

[53] Yan, A., Liu, G., Zhang, C., & Fang, L. (2013). The Study of Au/TiO$_2$/Au Resistive Switching Memory with Crosspoint Structure. In Advanced Materials Research (Vols. 652–654, pp. 659–663). Trans Tech Publications, Ltd. https://doi.org/10.4028/www.scientific.net/amr.652-654.659

[54] Doo Seok Jeong, Herbert Schroeder, Uwe Breuer, and Rainer Waser, J. Appl. Phys. 104, 123716 (2008)

[55] Kyung Min Kim *et al.* 2010 *Nanotechnology* **21** 305203

[56] Kyung Jean Yoon *et al.* 2012 *Nanotechnology* **23** 185202

[57] Kuyyadi P Biju *et al.* 2010 *J. Phys. D: Appl. Phys.* **43** 495104

[58] Xiaofang Hu, Wenhua Wang, Bai Sun, Yuchen Wang, Jie Li, and Guangdong Zhou *The Journal of Physical Chemistry Letters* **2021** *12* (22), 5377-5383 DOI: 10.1021/acs.jpclett.1c01420

[59] Priyanka Bamola, Bharti Singh, Aranya Bhoumik, Mohit Sharma, Charu Dwivedi, Mandeep Singh, Goutam K. Dalapati, and Himani Sharma *ACS Applied Nano Materials* **2020** *3* (11), 10591-10604 DOI: 10.1021/acsanm.0c01648

[60] Guangdong Zhou, Zhijun Ren, Bai Sun, Jinggao Wu, Zhuo Zou, Shaohui Zheng, Lidan Wang, Shukai Duan, Qunliang Song, Capacitive effect: An original of the resistive switching memory, Nano Energy, Volume 68,2020,104386, ISSN 2211-2855

[61] Ujjal Das, Anurag Dehingia, Bappi Paul, Pranab Kumar Sarkar, and Asim Roy *The Journal of Physical Chemistry C* **2021** *125* (24), 13610-13618.

[62] Ujjal Das, Dip Das, Bappi Paul, Tridip Rabha, Soumya Pattanayak, Aloke Kanjilal, Snigdha Bhattacharjee, Pranab Sarkar, and Asim Roy *ACS Applied Materials & Interfaces* **2020** *12* (37), 41718-41727.

[63] Lee, S. M., Choi, J., Jeon, J. B., Kim, B. J., Han, J. S., Kim, T. L., Jung, H. S., Jang, H. W., *Adv. Electron. Mater.* 2019, 5, 1800586. https://doi.org/10.1002/aelm.201800586

[64] Mi-Hee Jung, Sonny H. Rhim, Dohyun Moon, TiO2/RbPbI3 halide perovskite solar cells, Solar Energy Materials and Solar Cells, Volume 172, 2017, Pages 44-54,

[65] Lim, D.-H., Ramasamy, P., Kwak, D.-H. & Lee, J.-S. Solution-phase synthesis of rubidium lead iodide orthorhombic perovskite nanowires. *Nanotechnology* **28**, 255601 (2017)

[66] Nyayban, A., Panda, S., Chowdhury, A. & Sharma, B. I. First principle studies of rubidium lead halides towards photovoltaic application. *Mater. Today Commun.* **24**, 101190 (2020)

[67] Jayan, K. D. & Sebastian, V. An overview of the first principles DFT exploration of various properties of the individual layers of perovskite solar cells. in *Advanced Aspects of*

Engineering Research Vol.12 1–12 (Book Publisher International (a part of SCIENCEDOMAIN International), 2021).

[68] Carmen Abia, Carlos A. López, Javier Gainza, João Elias F. S. Rodrigues, Mateus M. Ferrer, Gustavo Dalenogare, Norbert M. Nemes, Oscar J. Dura, José L. Martínez, María T. Fernández-Díaz, Consuelo Álvarez-Galván, and José A. Alonso *Inorganic Chemistry* **2022** *61* (14), 5502-5511.

[69] K. Sk *et al..*, "Nonlinear coherent light–matter interaction in 2D MoSe $_2$ nanoflakes for all-optical switching and logic applications," *Adv. Opt. Mater.*, p. 2200791, 2022.

[70] B. Shi *et al..*, "Broadband ultrafast spatial self-phase modulation for topological insulator Bi2Te3 dispersions," *Appl. Phys. Lett.*, vol. 107, no. 15, p. 151101, 2015

[71] X. Li *et al..*, "Tri-phase all-optical switching and broadband nonlinear optical response in Bi2Se3 nanosheets," *Opt. Express*, vol. 25, no. 15, pp. 18346–18354, 2017.

[72] L. Wu *et al..*, "Few-layer tin sulfide: A promising black-phosphorus-analogue 2D material with exceptionally large nonlinear optical response, high stability, and applications in all-optical switching and wavelength conversion," *Adv. Opt. Mater.*, vol. 6, no. 2, p. 1700985, 2018.

[73] L. Wu et al.., "Few-layer tin sulphide: A promising black-phosphorus-analogue 2D material with exceptionally large nonlinear optical response, high stability, and applications in all-optical switching and wavelength conversion," Adv. Opt. Mater., vol. 6, no. 2, p. 1700985, 2018.

[74] Wang, G. *et al..* (2015) "Tunable nonlinear refractive index of two-dimensional MoS_2, WS_2, and MoSe_2 nanosheet dispersions [Invited]," *Photonics research*, 3(2), p. A51. doi: 10.1364/prj.3.000a51.

[75] Villafranca, A. B. and Saravanamuttu, K. (2009) "Diffraction rings due to spatial self-phase modulation in a photopolymerizable medium," *Journal of Optics A Pure and Applied Optics*, 11(12), p. 125202. doi: 10.1088/1464-4258/11/12/125202.

[76] Li, J. *et al..* (2020) "Broadband spatial self-phase modulation and ultrafast response of MXene Ti3C2Tx (T=O, OH or F)," *Nanophotonics*, 9(8), pp. 2415–2424. doi: 10.1515/nanoph-2019-0469.

[77] Zhang, Q. *et al..* (2017) "Optical limiting using spatial self-phase modulation in hot atomic sample," *Optics and laser technology*, 88, pp. 54–60. doi: 10.1016/j.optlastec.2016.09.001.

[78] Sadrolhosseini, A. R. *et al..* (2016) "Spatial self-phase modulation patterns in graphene oxide and graphene oxide with silver and gold nanoparticles," *Optical and quantum electronics*, 48(4). doi: 10.1007/s11082-016-0485-2.

[79] Karimzadeh, R. (2012) "Spatial self-phase modulation of a laser beam propagating through liquids with self-induced natural convection flow," *Journal of optics (2010)*, 14(9), p. 095701. doi: 10.1088/2040-8978/14/9/095701.

Chapter 3

Instruments, Characterization Techniques and Synthesis processes

3.1. Abstract:

The creation of nanomaterials has attracted the interest of the scientific community recently due to its unique features and wide range of uses. This chapter is separated into two main areas: the general description of the major synthesis equipment and the primary characterizing accessories. These two sections are used to characterize techniques and evaluation procedures used to analyse the synthesized nanomaterials. Numerous physical and chemical methods are improving nanoparticle preparation. We have primarily concentrated on the chemical synthesis process for the construction of nanostructures instead of using complex and expensive physical approaches. TiO_2 nanorods on FTO coated glass substrates were also produced using hydrothermal process, autoclaves, sonicate machine, and oven.

Additionally, a brief summary of the various characterization techniques used to examine the material's structural, compositional, morphological, optical, and electrical properties is provided. These techniques include powder X-ray diffraction (XRD), field emission scanning electron microscopy (FESEM), energy dispersive X-ray (EDX) and UV-Vis analysis.

3.2. Synthesis techniques and apparatuses:

3.2.1. Hydrothermal process:

The term "hydrothermal" is defined as performing chemical reactions in solvents contained in sealed vessels in which the temperature of solvents can be brought to around their critical points via heating concurrently with autogenous pressure. This process referred as hydrothermal because in this method water is used as a primary solvent. In this case aquas mixture of precursors heated in a sealed stainless-steel autoclave above the boiling point of water and concurrently the pressure within the autoclave dramatically increased. This technique is useful to grow nanoparticle or thin film of the material has a high vapour pressure near its melting point or crystalline phases are stable at melting point. Synthesis of nanoparticle or thin film of nanoparticles by hydrothermal process is a crystallization process directly from solution that involves mainly two steps one is crystal nucleation and another is subsequent growth. Nucleation occurs when the solubility of the solute exceeds its limits in the solution means when solution become super saturated.
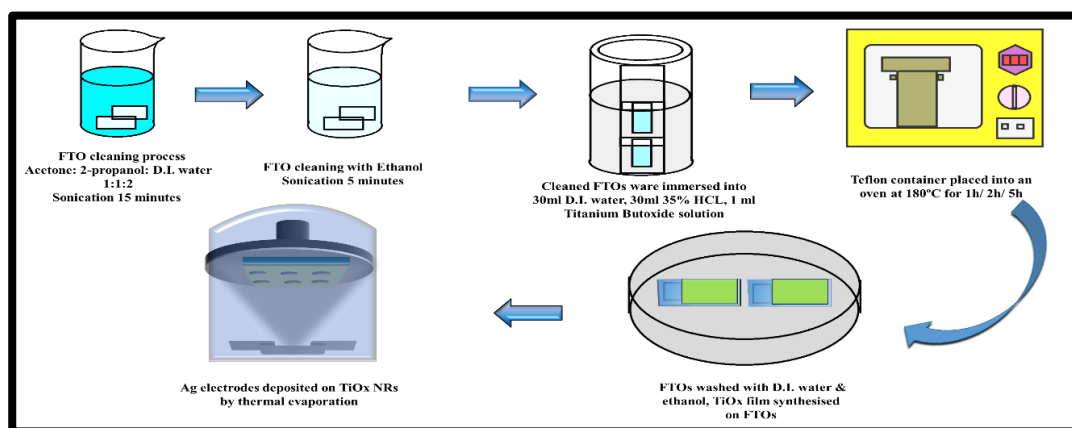
Figure 3.1: schematic representation of hydrothermal synthesis process for TiO_2 nr on

FTO substrate.

73

This reaction is irreversible. It allows greater control, low temperature synthesis, more control over composition of the end product. It is more environment friendly method and replaced the solid-state synthesis processes. The schematic diagram of synthesis of TiO_2 nanorods on FTO coated glass substrate shown in below figure 3.1.

3.2.2. Autoclave:

Hydrothermal method has been widely used in the synthesis of metal oxide nanostructures for the unique advantages in the synthesis. For a typical hydrothermal reaction, apparatus, called either "autoclaves" or "bombs", are used. Synthesis of TiO_2 nanorod thin film on FTO coated glass substrate was done using autoclave apparatus as shown in figure 3.2. An autoclave is a specially designed pressurized reactors to heat aqueous or non-aqueous solvent above their boiling point at a pressure higher than normal pressure. It is consisting of two different parts: Teflon-lined inner part and an outer stainless-steel case. The inner part can easily fit into the outer part which can resist high pressure during a reaction. A cylindrical Teflon tube with a Teflon cap, which serves as the inert reaction chamber, was fitted inside the iron chamber.

Figure 3.2: Autoclave with Teflon container.

3.2.3: Oven:

As the reaction temperature was not more than 250 ºC, a simple low temperature oven was also used in order to perform the reaction. The heating rate of the oven can be controlled with an accuracy of ± 0.5 ºC by an electronic temperature controller. Apart from the purpose of synthesis, the ovens were used for drying the sample also. Optical image of used oven shown in figure 3.3.

Figure 3.3: Photograph of an oven which was used during synthesis procedures.

3.2.4 Thermal evaporation:

One of the most popular physical deposition techniques is this one. It is simple method and one can evaporate a large variety of materials on various substrates. In this method, deposition material is created in a vapor form by heating bulk material in vacuum using resistive heater. The vapor atoms are transported through vacuum to get deposited on the desired substrate. Almost all materials are vaporizing from a solid or liquid phase as

neutral atoms or molecules. This vapour deposition is done only at pressure less than 5^- ^{10} torr. By the help of this instrument, we mainly deposit low melting point materials like Silver, Aluminium and Gold (schematic diagram shown in Fig 3.4). The evaporation of the desired material is done in vacuum system, which consists of a diffusion pump backed by a rotary pump. The desired evaporate material is supplied by a continuous source which is then heated to a sufficiently high temperature to produce desired vapour pressure. The vacuum system employed to deposit and characterize thin films in the present work contain a variety of pumps, tubing, valves and gauges to establish and measure the required pressure. The "Hind Hivac" coating unit's vacuum system (Model No. 12 A4) essentially comprises of a 0.4 m diffusion pump working in tandem with an oil-sealed rotary pump. Optical image of the device shown in figure 3.5. The ultimate pressure achieved in a 30 cm diameter stainless steel bell jar is of the order of 6 x 10^{-6} Torr. Substrates can be cleaned by ion bombardment.
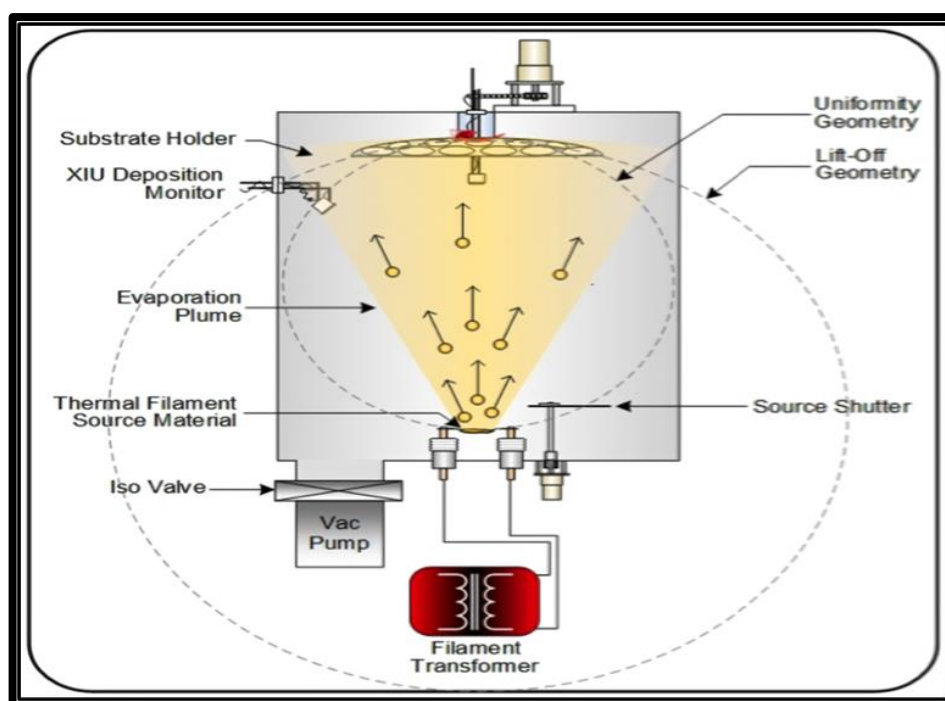
Figure 3.4: schematic diagram of experimental setup for thermal evaporator. [adopted from internet]

A low-tension transformer of 10 V-100 A is used for filament heating. Most of the evaporations are carried out at pressures of (1-8) x 10^{-4} Torr. The pressure obtained by the rotary pump is measured by means of a Pirani gauge and a Penning gauge measures the diffusion vacuum. This machine was used to deposited Ag electrode in our experiment.

Figure 3.5: Thermal evaporator unit with accessories.

3.3 Characterization techniques of nanomaterials:

3.3.1. X-Ray Diffractometer (XRD):

X-Ray diffractometer analysis (XRD), in which X-Ray diffraction patterns are recorded using Cu (Kα) radiation source (λ=1.5406), is the primary characterization technique used to determine the structural phase and crystallinity of a certain material.

❖ *X-Ray diffraction principle and Bragg's Law:*

Considering a crystal to be regular arrays of atoms and X-rays to be the electromagnetic waves then electrons inside the atoms gets scattered through impinging X-ray waves. This is an example of elastic scattering. So, for a regular array of atoms, regular array of spherical waves is generated. These emanating waves of electrons from inside the crystal cancel out each other in most cases through destructive interference barring a few exceptions in which they lead to constructive interference according to Bragg's law:

$$2dSin\theta = n\lambda$$ ....(i)

Here, d is the distance between diffracting planes, θ is the incident angle of the X-rays, n is any integer and λ is the wavelength of the incoming X-ray beam. [1]

Usually when an XRD pattern for a material is obtained it is then compared with standard diffraction database files published by the Inorganic Crystal Structure Database (ICSD) for the material with specific crystal symmetry to match and confirm the phase purity. Other than crystallinity and phase information of a material, information of strain can also be obtained using XRD analysis.

Calculation of strain can be done by observing the shift in diffraction peak positions due to presence of defects or doping as it gives the change in d-spacing and signifies change in lattice constant under homogeneous strain. Information about inhomogeneous strain can also be obtained using XRD analysis in some cases. However, the most accepted way to calculate crystallite size in absence of inhomogeneous strain is given by the Scherrer's formula:
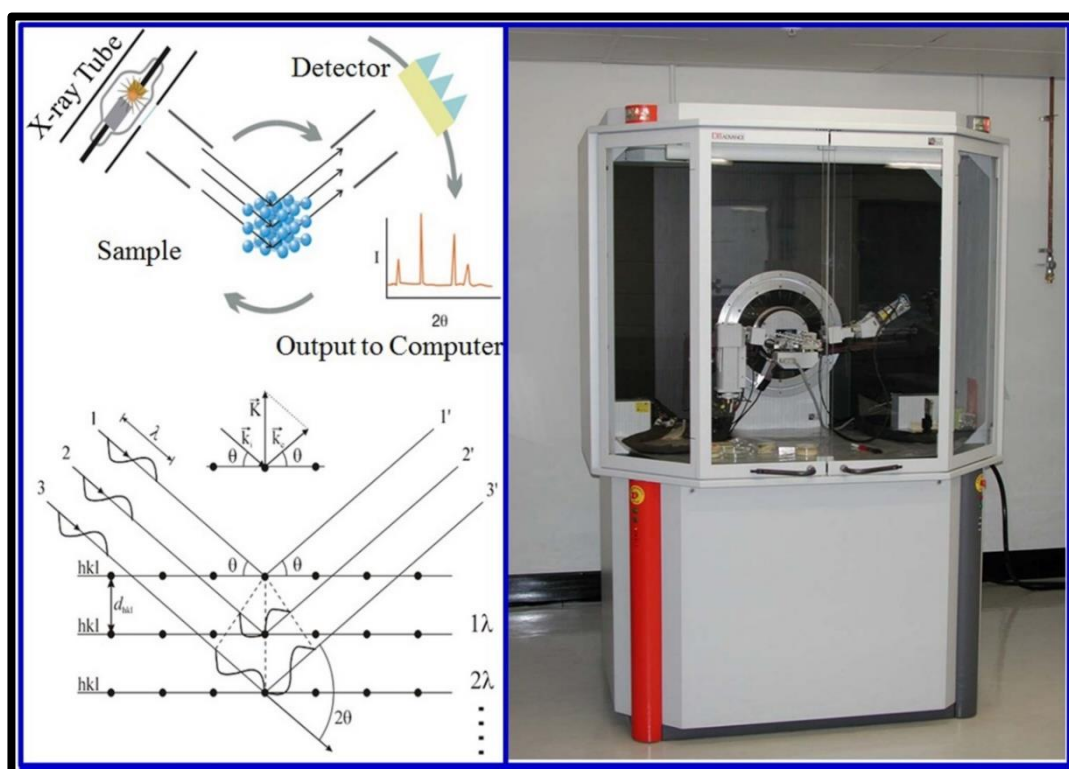

Figure 3.6: Schematic of working principle behind X-Ray diffraction according to Bragg's law with XRD machine in left side. [adopted from internet]

$$D = \frac{k\lambda}{\beta \cos\theta} \qquad \ldots\ldots\ldots\ldots\ldots\ldots\ldots \text{(ii)}$$

Here, D is the crystal size, β is full width and half maxima of diffraction peak, θ is diffraction angle, k is Scherrer constant generally 0.9, λ is the wavelength of x-ray. [2-3]

After getting the XRD data, I plot that data with help of Origin software to get the XRD pattern. With the help of X-part High Score software and Origin I derived the crystallites sizes and Miller indices for my samples. Here XRD unit and schematic representation of mechanism involved in XRD technique also Braggs law shown in figure 3.6.

3.3.2: Field Emission Scanning Electron Microscope (FESEM):

The most effective and widely used method for characterising materials at the nanoscale is electron microscopy. Ernst Ruska invented the TEM in 1939 as a result of the constrained imaging resolution of the time's optical microscopes. The discrepancy is due to the wavelength of the sources that are being utilized, in this case light and electrons. Two research teams, Davisson & Germer [4] and Thomson & Reid, independently conducted their classic electron diffraction experiment in 1927, barely two years after de Broglie's [5] theoretical prediction of the wave qualities of electrons. This experiment verified the wave nature of electrons [2]. The use of electron microscopes over optical microscopes is preferred for two main reasons (OM). The electromagnetic lenses inside the microscope column can readily and effectively manipulate the electrons, which is the first justification. The second factor is the electron's extremely narrow wavelengths, which provide better resolution than the OM. The wavelength of the source has a significant impact on the resolution of microscopes.

High resolution imaging is achieved using the field emission scanning electron microscope (FESEM), which accelerates electrons from a field emission source in a field gradient under high vacuum. These so-called primary electrons are focused and refracted by electronic lenses within the high vacuum column to create a narrow scan beam that bombards the target. In most cases, incident electrons interact with a specimen and six

different types of electrons are produced: transmission, backscattered, reflected, secondary, Auger, and trapped electrons (Figure 3.7 (C). As a result, each area on the item emits secondary electrons. The surface structure of the item is related to the angle and speed of these secondary electrons. The secondary electrons are captured by a detector, and a picture of the sample surface is created by contrasting their intensity with that of the primary electron beam that is scanning. Different signals (secondary electrons, backscattered electrons, etc.) are released from each point that is exposed to an electron beam when it is scanned across a specimen surface.
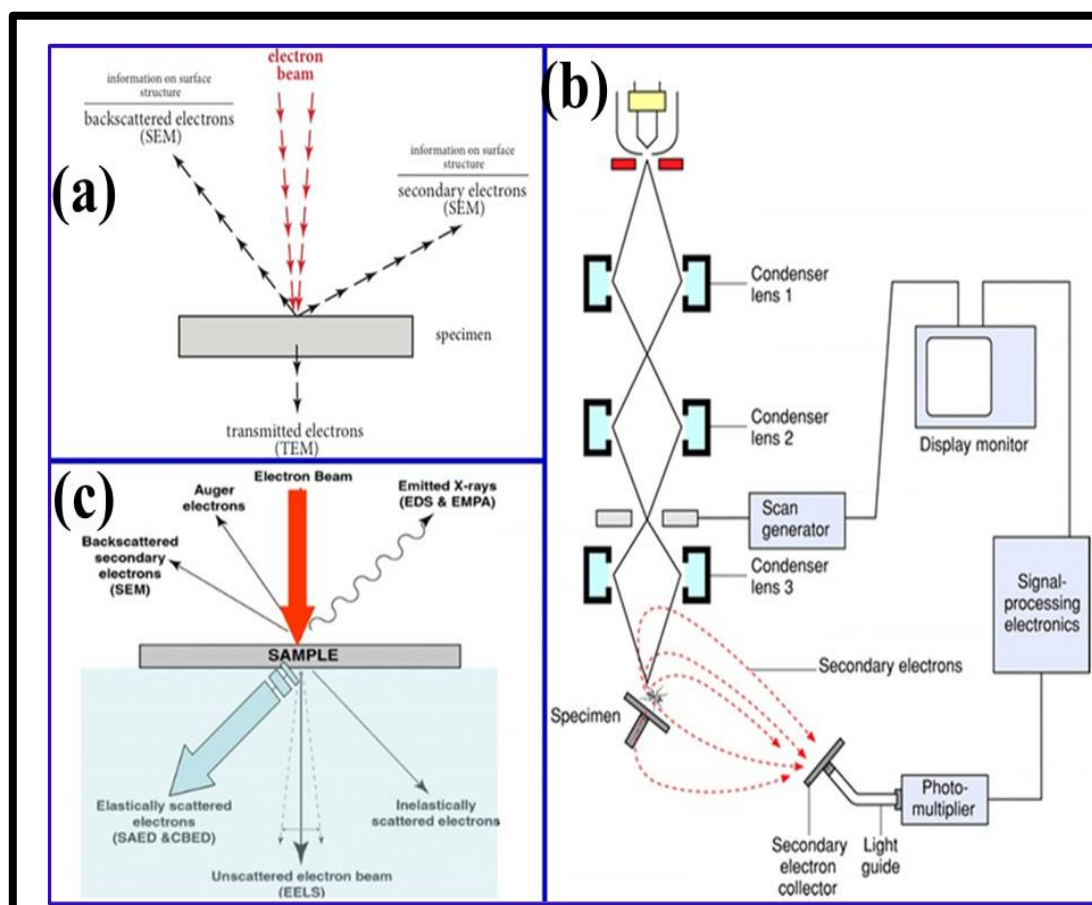
Figure 3.7: Schematic line diagram of FESEM machine. Also, electron paths and different types of secondary beams shown in right side of the image. [Adopted from internet]

These signals are recognized, translated into electric signals, amplified, and either converted into a digital image that can be saved and processed further or into a video scan-image that can be displayed on an LCD monitor. A field emission scanning electron microscope is depicted simply schematically in figure 3.7 (b).

The TiO_2 nanostructures were subjected to detailed morphological investigations with a FESEM (FEI - INSPECT F50) instrument. Coating the sample with a thin layer of conductive material, such gold or platinum, applied using a sputtering machine, is a popular preparation technique. The instrument's resolution was 2 nm (1 kV of accelerating voltage) and 1 nm (Accelerating voltage 15 kV). Between 0.5 and 30 kV is the range of the accelerating voltage (in 100 V steps). It was possible to alter the magnification between 30 X and 3,000 X (low magnification mode) and 100 X and 800,000 X. Figure 3.4 depicts a shot of the FESEM device. With narrower probing beams available at both low and high electron energies thanks to a scanning electron microscope's field-emission cathode, spatial resolution is increased while sample charging and damage are reduced. Original optical image of FEI INSPECT F50 FESEM machine shown in figure 3.8.

Figure 3.8: Optical image of FEI INSPECT F50 FESEM machine.

[Dept. of Physics, J.U.]

3.3.3: Energy Dispersive X-ray Spectroscopy (EDS):

Field emission scanning electron microscopy is used in conjunction with the chemical microanalysis method known as energy dispersive X-ray spectroscopy (EDS or EDX) (FESEM). In order to achieve a localized chemical analysis, EDS makes use of the X-ray spectrum produced by a solid sample that has been subjected to a focused electron beam. The detection of all elements from atomic number 4 (Be) to 92 (U) is theoretically possible. In order to characterize the elemental composition of the studied volume, the EDS technique uses the detection of x-rays released from the sample during bombardment by an electron beam. Analysis is possible for features or phases as tiny as 1 m or less. Electrons are ejected from the surface-containing atoms of the sample when it is blasted by the FESEM's electron beam. Electrons are ejected from the sample's surface atoms when it is hit by the FESEM's electron beam. In order to balance the energy disparity between the two electrons' states, an x-ray is released when the ensuing electron vacancies are filled by electrons from a higher state. The element from which the x-ray radiation was emitted is what makes it up.
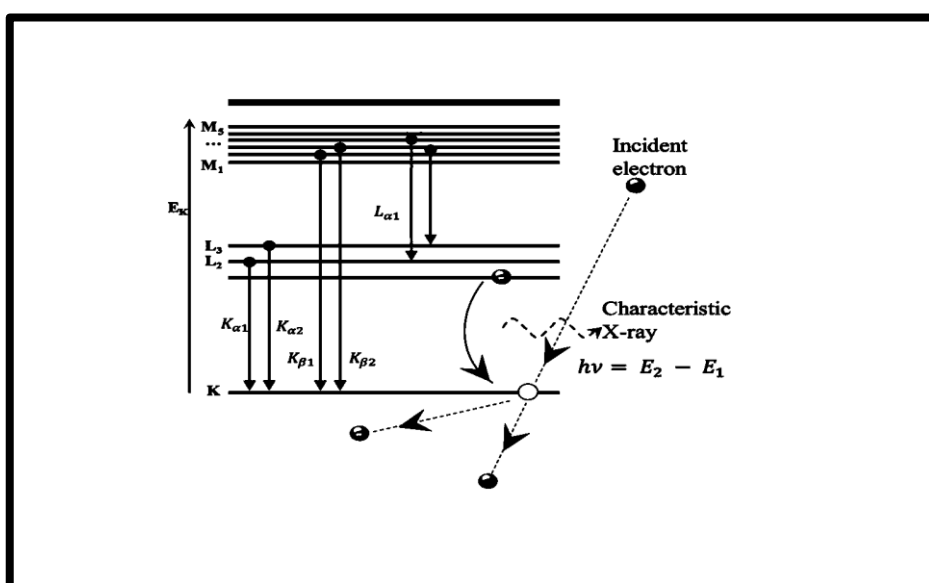
Figure 3.9: creation of a distinctive X-ray quantum. [adopted from internet]

Energy is transferred from an incident electron to an electron in an atom's inner shell during the first stage, called ionisation. This electron is either promoted to the lowest unoccupied level or ejected into the vacuum, depending on the amount of energy actually consumed. This leaves a vacancy in the low energy level, in this case the K shell. An electron from a higher state—in this case, the L3 level—drops down and fills the vacancy in the second step. An X-ray quantum is released as a result of the excess difference energy. Every element has a specific number of localised electrons in distinct energy levels. Schematic representation shown in figure 3.9.

3.3.4: UV-Vis-NIR spectrophotometer:

UV-Vis-NIR spectrophotometer is used to study the optical properties of nano samples. Optical transmittance, absorbance and reflectance can be measured using this spectrometer. The Bouguer-Lambert-Beer law forms the mathematical physical basis for the light absorption measurements on gas and in solution. According to this law, absorbance is directly proportional to the path length, l and the concentration of the absorbing substance, c, and can be expressed as $A = \alpha l c$, where α is a constant of proportionality, called the absorptivity. An important technique for measuring the band gap of the semiconductor material is to study its absorption or transmission of incident photon by the material. Since the photon with energies greater than band gap are absorbed while photon with energy less than the band gap is transmitted. Hence the experiment gives the accurate measure of the material's band gap. [6] A Shimadzu UV-Vis-NIR (UV-3101-PC) spectrophotometer was used to measure reflectance spectra of the TiO_2 thin films.

A beam of light of selected wavelength is passed through the sample. Visible, near - infrared or ultraviolet light from the lamp enters the monochromators, which disperse the

light (spread it into a spectrum) and select the particular wavelength chosen by the operator for the measurement.

Shimadzu UV-Vis-NIR (UV-3101-PC) spectrophotometers were used to measure the extent to which the samples under consideration reflectance light of different wavelengths. A photograph of the instrument is shown in the Fig. 3.10. The instrument automatically records a graph of reflectance vs. wavelength. From that graph the bandgap of TiO_2 thin film measured using some mathematical process. Also, absorbance of $RbPbI_3$ nanorods measured by this machine for determination of direct bandgap.

Figure 3.10: Photograph of Shimadzu UV-Vis-NIR (UV-3101-PC) spectrophotometer.

3.4. Instruments and software used for resistive switching and synaptic property measurements and data analysis tools:

3.4.1. Keysight Source Meter (B2902A):

Keysight B2902A source meter used to measure all current-voltage measurements including resistive switching and synaptic properties during my project work. This SMU is very much portable and advanced, cost effective, easy to use compare to other competitors in market. A 2-channel, small, and reasonably priced bench-top SMU, the Keysight B2902A Precision Source / Measure Unit (SMU) has the ability to source and measure both voltage and current. It can easily and accurately monitor current vs. voltage because to its versatility. [7] I-V measurement is made simple and straightforward without the need to configure different instruments thanks to the integration of 4 quadrant source and measurement capabilities. The minimal expenditure is made possible by the single instrument's extensive coverage of 210 V, 3 A DC, and 10.5 A pulse. Accurate characterization of the DUT is supported by a minimum measurement resolution of 100 fA/100 nV. The Keysight B2902A Precision Source / Measure Unit (SMU) is a benchtop SMU with two channels that can used as source and measure current as well as voltage.

Figure 3.12: (a) Optical image of Keysight SMU B2902A, (b) Optical image of Tungsten Probs.

I also use tungsten(W) probs for connecting top and bottom electrodes with this system. Keysight B2902A SMU and tungsten probs are shown in figure 3.12.

3.4.2. Essential accessories:

Following devices and instruments were used during electrical and optical measurements, e.g;

a) Laptop- computer (HP 15s-eq2000 Ryzen 5500series with Windows 11 support)

b) Blue laser diode ($\lambda = 405$ nm), green laser diode ($\lambda = 532$ nm)

c) UV torch

d) Light holding stands

e) A closed chamber

f) A white screen

g) A DSLR camera

h) Cuvettes with different lengths (L = 10, 5, 1 mm)

i) Lens (f = 20cm)

j) Intensity power meter for light power measurement

k) A DC voltage source

3.4.3. Software:

List of used softwares given below,

a) Keysight Connection Expert

b) Quick IV measurements

c) Origin 2018

d) MS Office tools

e) X-pert High Score Plus

f) MATLAB 2022a

g) DaVinci Resolve 2022

h) ImageJ

3.5. Reference:

[1] https://en.wikipedia.org/wiki/X-ray_crystallography

[2] B. D. Culity and S. R. Stock, Elements of X-ray diffraction. Prentice Hall, New Jersey, 3rd edition, 2001

[3] M. J. Burger. X-ray Crystallography. John Wily and Sons, New York, 3 edition 1962

[4] C. Davisson, and L.H. Germer, Diffraction of Electrons by a Crystal of Nickel. Physical Review, 30(6): p. 705-740 (1927).

[5] L. De Broglie, Recherches sur la Theorie des Quanta (Researches on the Quantum Theory). Ann. Phys., 3: p. 22-128 (1925).

[6] B.G Streetman, Solid state electronics devices. Prentice Hall of India Pvt. Ltd, New York, (1995)

[7]   https://www.keysight.com/us/en/product/B2902A/precision-source-measure-unit-2-ch-100fa-210v-3a-dc-10-5a-pulse.html

Chapter 4

Study of Resistive Switching and Synaptic Properties on TiO$_2$-Based Memory Devices and Its Application as Artificial Vision Sensor with Machine Learning Approach
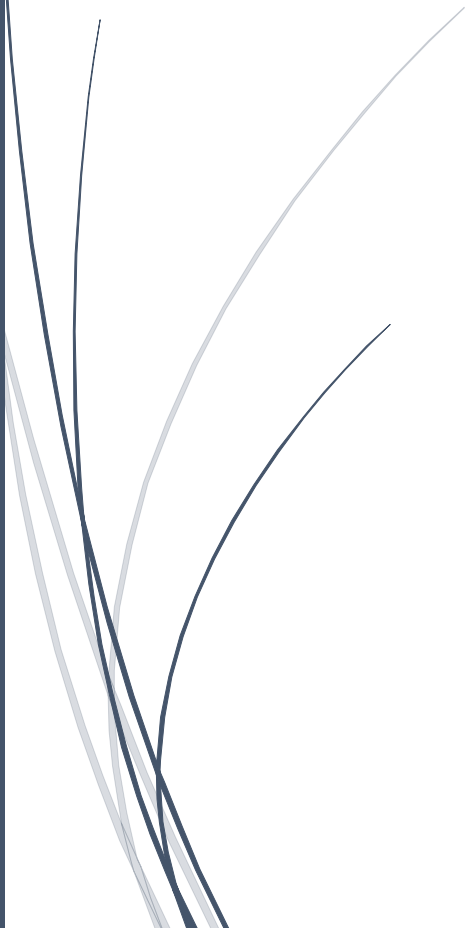
4.1: Introduction:

Memristors or resistive switching (RS) devices has gained more attention as alternative candidate in non-volatile memory device application. ReRAM has more advantages compare to traditional NAND Flash memories, like small cell size, best endurance and retention with low operating current, low power consumption, in memory computing, high scalability etc. [1-4] Memristors are the working units of ReRAM memory devices. Electrical and optical resistive switching behaviour have been reported using various types of nanomaterials including TiO_2. In our experiment, we have explored TiO_2 nanorod based MIM memristor structure. The device structure is $Ag/TiO_2/FTO$. We show here by experiment how resistive switching properties depend on hydrothermal synthesis time of TiO_2 nanorods. There are few reports which had discussed about synthesis temperature but the study of synthesis time variation is done in this work. We have studied the RS by applying both electrical and optical inputs. We have also discussed the switching mechanism in this chapter. After that we have employed synaptic functionalities in our fabricated device for neuromorphic applications. At last, we have used the device as optical sensor and built an artificial vision system model.

4.2: Experimental Section:

4.2.1: Synthesis procedure of TiO$_2$ nanorod arrays on the top of FTO coated glass substrate via hydrothermal synthesis route:

➢ **Materials needed:**

Distilled water (DI) (H$_2$O), acetone (CH$_3$COCH$_3$), 2 - propanol (CH$_3$CHOHCH$_3$), hydrochloric acid (35%-37%) (HCL), titanium butoxide (Ti (OC$_4$H$_9$)$_4$), ethanol (C$_2$H$_5$OH), fluorine doped tin oxide coated glass substrates (FTO).

➢ **Synthesis Process:**

For our experiment, we synthesized 6 different samples namely, TH, T1, T2, T5, T1A, T1E by hydrothermal process. [5,6] From these samples, three T1 samples were made after that two samples are used for annealing and etching purpose. Here temperature was fixed at 180 ℃ and time duration varied according to need. 30 minutes, 1 hour, 2 hours, 5 hours were the synthesis time for respective samples. First FTO coated glass substrates were cleaned by mixture of acetone, 2- propanol, DI with 1:1:2 weight ratio. In that solution FTO coated glass substrates dipped and sonicated for 10 minutes to clean the unwanted dust and chemicals from the top of the FTO coating. In next step that FTO coated glasses again dipped into ethanol and sonicated for next 10 minutes. After sonication process FTO coated glasses dried carefully using hairdryer, it was kept in mind that no bubbles were present on the FTO layer. After drying FTO coated glasses they stored on tissue paper bed for further use.

Now a Teflon container cleaned with soap water and then HCL, DI, ethanol respectively. A magnetic bead put into Teflon container and that container placed on the top of a magnetic stirrer. 30mL DI poured into that Teflon container and 30mL HCL

poured by using micropipette at the rate of 1 mL/minutes for 30 minutes. 1mL titanium butoxide poured into that mixture for another 5 minutes. Now cleaned FTO coated glass substrates attached on a glass slide by using Teflon tape and that glass slide placed diagonally into Teflon container. That container sealed with help of Teflon tape and fitted into autoclave. That autoclave placed into Oven at 180º C for previous mentioned times.

After synthesis autoclave opened and FTO coated glasses removed from glass slide. TiO$_2$ nanorods synthesized vertically on the FTO coated glass substrates. Cleaned by ethanol washed process. Two T1 devices were further processed by 30 min for air annealing and acid etching. At last Silver (Ag) electrodes thermally deposited by thermal evaporator. This whole process with schematic representation shown in the figure 4.1. We gave names to samples according their synthesis times and processing nature namely, TH, T1, T1A, T1E, T2, T5 respectively.
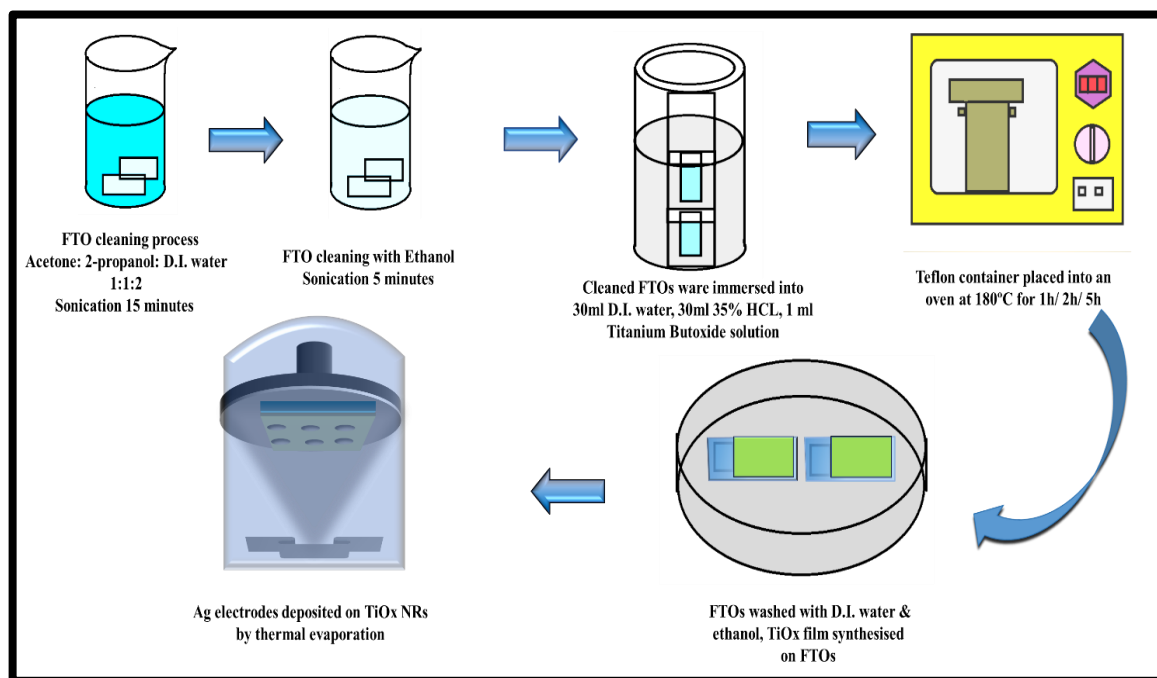
Figure 4.1: Schematic representation of TiO$_2$ nanorod synthesis process by hydrothermal method with electrode deposition for device application.

4.2.2: Basic Characterisations:

4.2.2.1: X-ray Diffraction Analysis:

X-Ray diffraction analysis was carried out by Rigaku MiniFlex 600 XRD instrument. Intensity vs 2θ graph of TH, T1, T2, T5, T1A, T1E, Blank FTO samples are shown in figure 4.2.
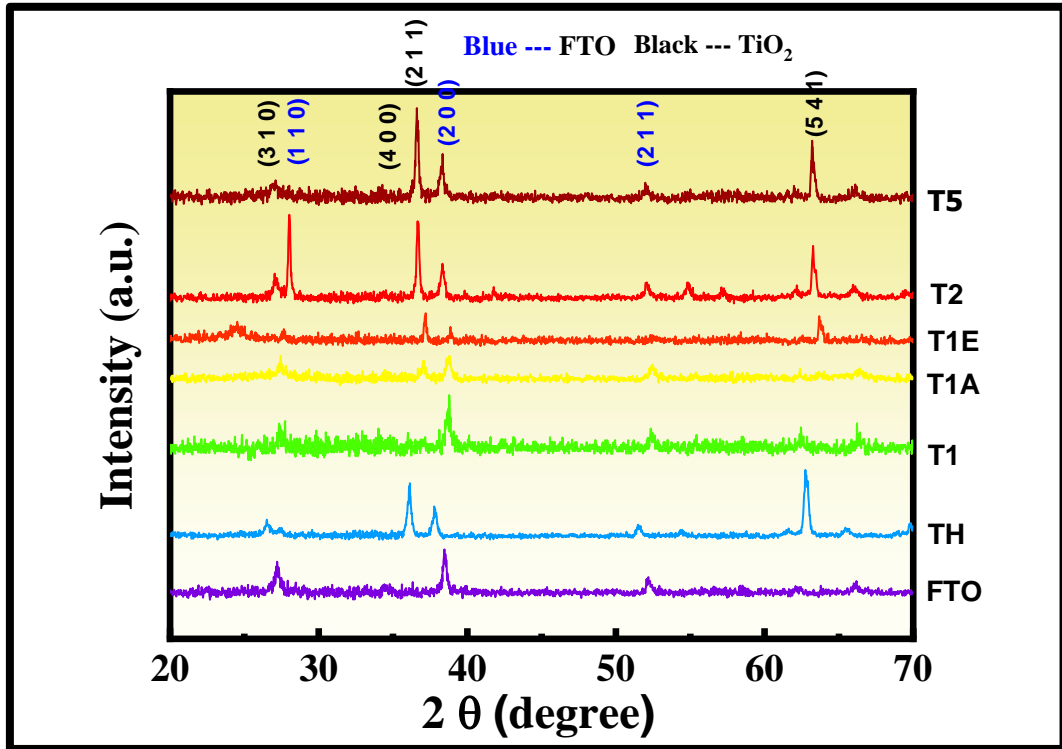
Figure 4.2: XRD patterns for different TiO₂ samples with blank FTO.

These XRD patterns matched with ICDD cards 21-1276, 41-1445 for TiO_2 (rutile) and F-doped SnO_2 (FTO) respectively. Rutile phase of TiO_2 synthesised in this experiment. With increasing time duration, the peaks for TiO_2 increases consistent with height of the nanorods with synthesis time. This revealed that the nanorods vertically grown on the FTO substrate. By above analysis we can say that in our samples TiO_2 rutile phase synthesized. Crystal system were tetragonal crystal system. And schematic crystal structure shown in the figure 4.3(a).

95
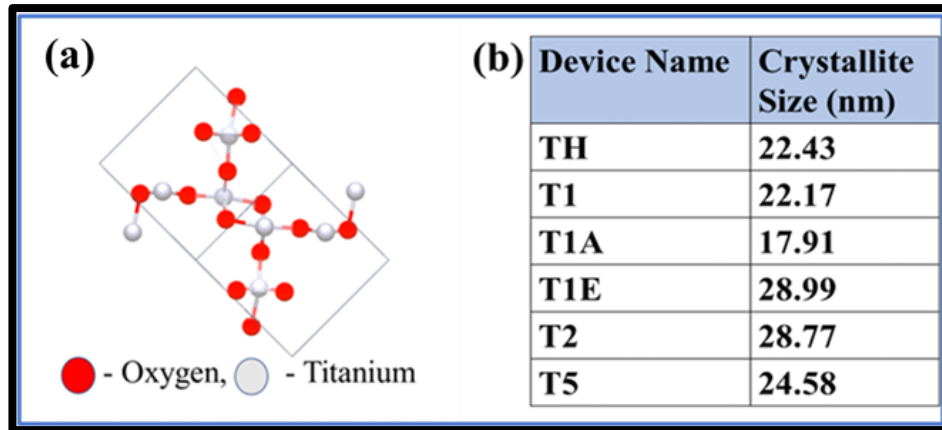
Figure 4.3: (a) Schematic crystal structure of rutile TiO$_2$. (b) Table of calculated average crystallite sizes for all devices.

By using Scherrer equation [7] calculated average crystallite size is 22.17 nm for T1 device. Average crystallite sizes for rest all devices shown in figure 4.3 (b).

4.2.2.2: Morphological analysis:

The morphology and microstructure of the samples were studied by field emission scanning electron microscope (Inspect F50) at an accelerating voltage of 5.0 kV. FESEM images are shown in figure 4.4. Here all images were taken at 1µm magnification. Cross sectional views of all sample devices given in figure 4.5. From figure 4.4 and figure 4.5 we measured diameters and lengths of the nanorods and details are given in table 4.1. Statistical distribution graph by which we got mean diameter values are shown in figure 4.6. Also, graphical representation of diameter and length comparison between sample devices shown in figure 4.7.
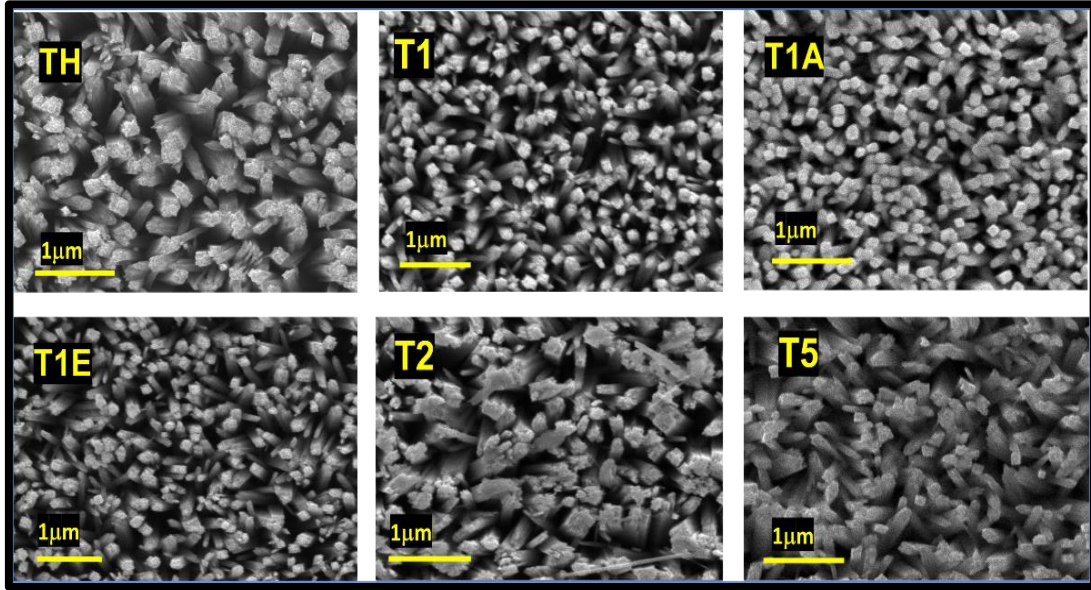
Figure 4.4: FESEM images of all samples at 1µm magnification. Name of respective samples are given in upper left corner of each picture.
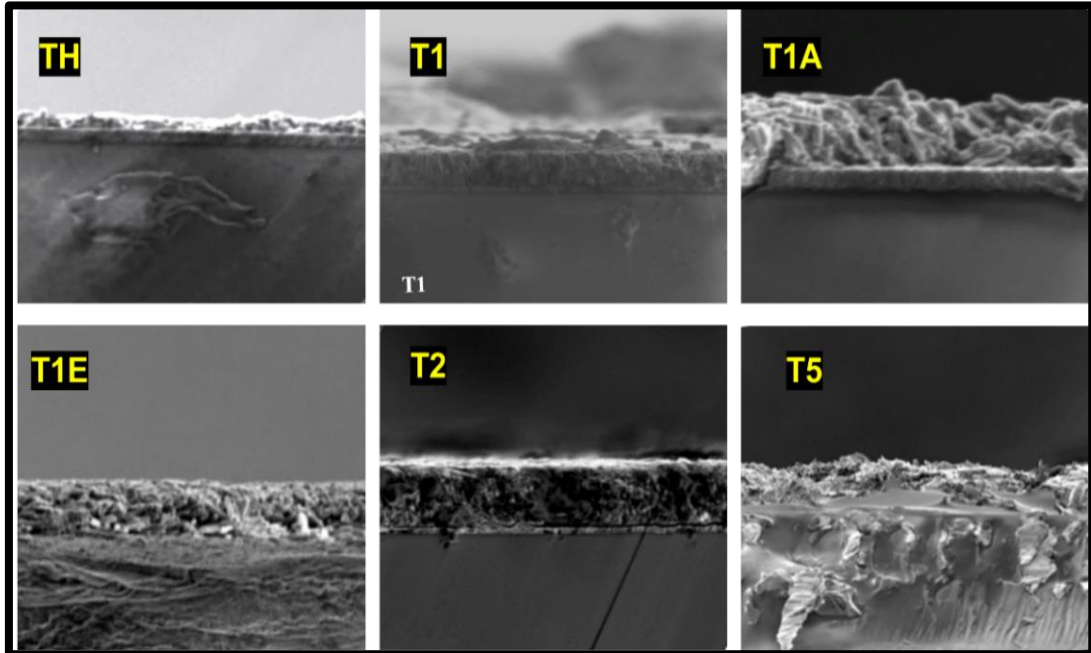
Figure 4.5: Cross section view of all sample devices, respective names are denoted at upper left corner.
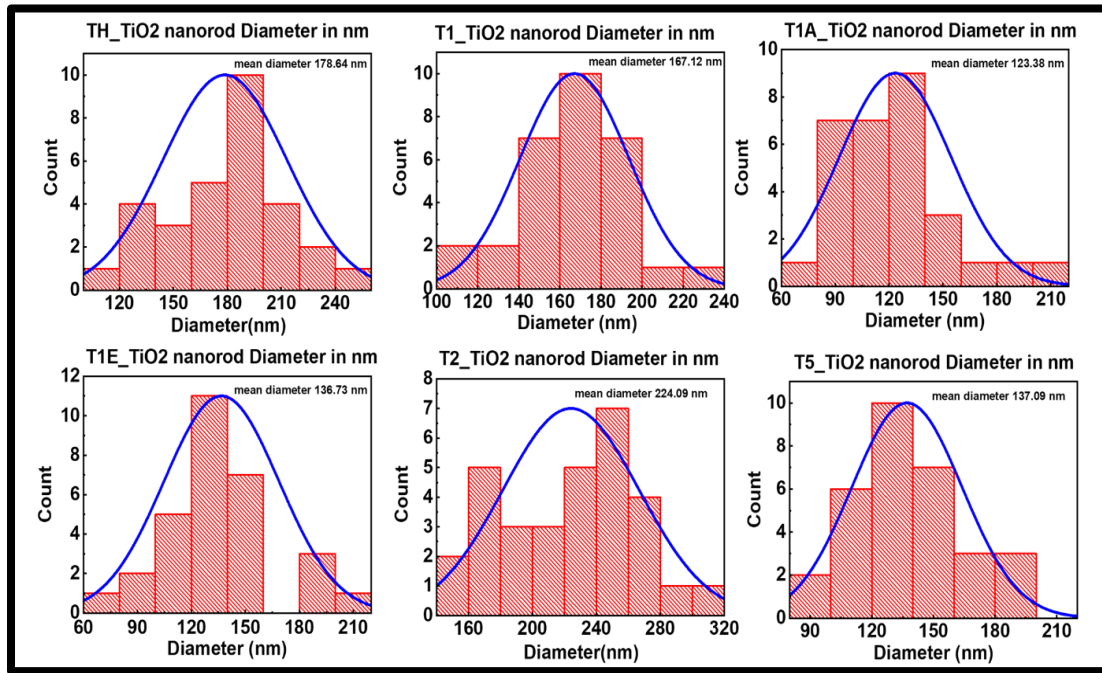
Figure 4.6: Statistical distribution graph by which mean diameter values estimated.
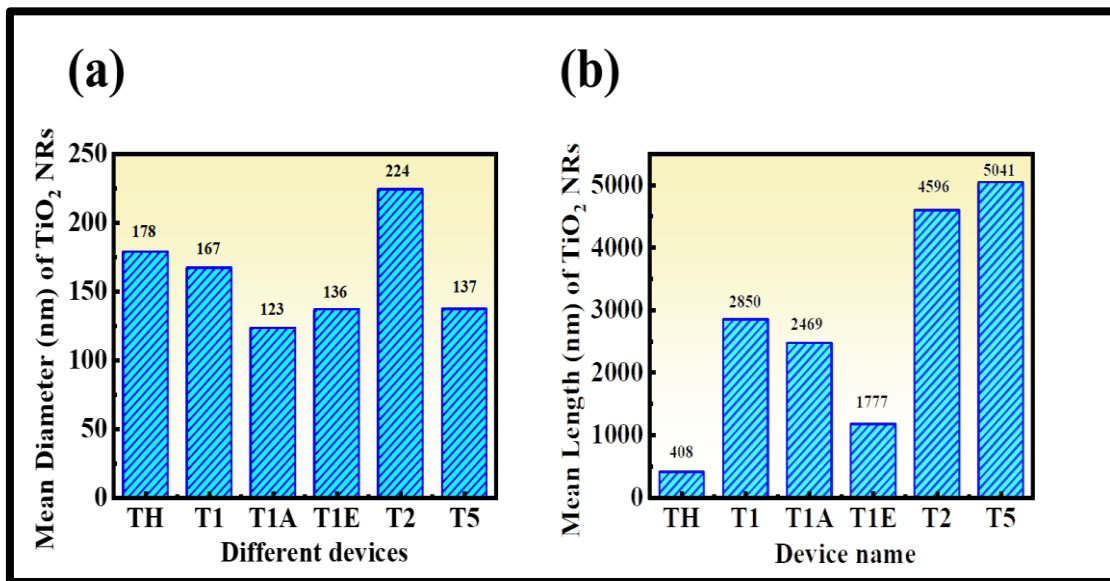
Figure 4.7: (a) measured approximate diameters in nm of TiO_2 nanorods for all samples,

(b) approximate lengths in nm of TiO_2 nanorods measured for all samples.

Table 4.1: (a) measured approximate diameters of nanorods for all samples, (b) approximate lengths of TiO_2 nanorods measured for all samples.

(a) Device name	Mean Diameter of TiO_2 NRs (nm)	(b) Device name	Mean Length of TiO_2 NRs (nm)
TH	178	TH	408.6
T1	167	T1	2850.7
T1A	123	T1A	2469.7
T1E	136	T1E	1777.6
T2	224	T2	4596
T5	137	T5	5041

Square shaped nanorods grown-up vertically with respect to synthesis time. These shapes are dependent on bath solution not on used substrates. [8,9] Junction surface increased by intertwining of nanorods and resulting in electron transfer channels. [10,11] Length of that nanorods increases with time due to decomposition rate of the titanium butoxide increases. [12,13] For this reason length of nanorods in T5 device is highest among all and same for TH is lowest clearly noticed by table 4.1 (b). Here length of T1A decreases because of reduction of oxygen vacancies and moisture. And by acid etching nearly half of length of T1 device etched off in T1E device.

4.2.2.3: Compositional Analysis (EDS – Analysis):

The chemical compositions, as well as the spatial uniformity of the elemental distribution, were analysed by energy disruptive X-ray spectroscopy (EDS, Inspect F50) at 15.0 kV. The EDS results are presented in figure 4.8.
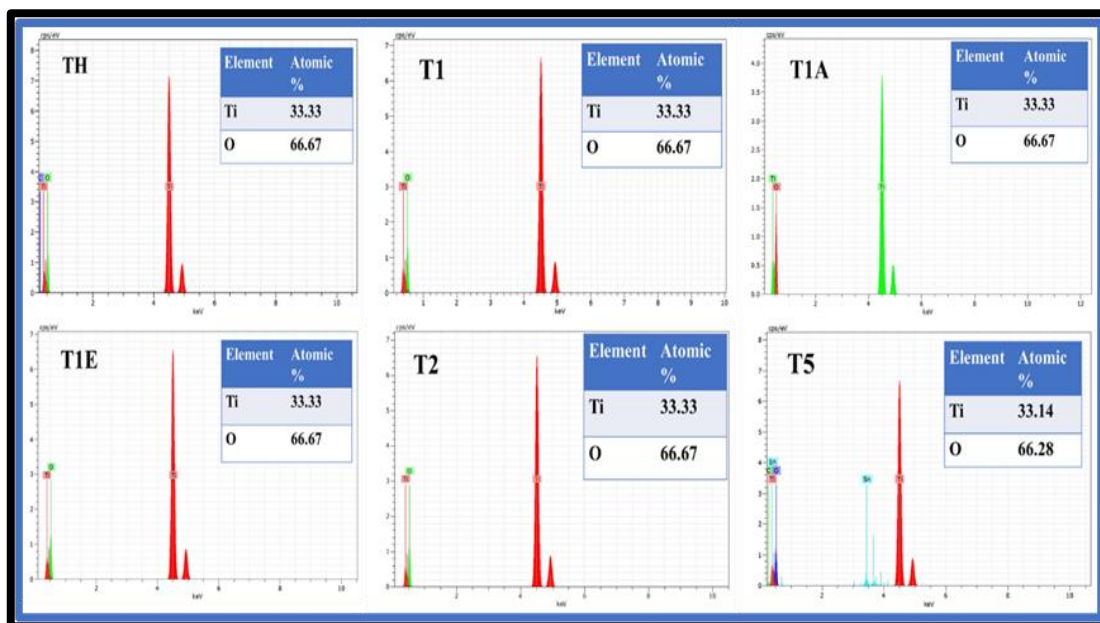
Figure 4.8: EDS analysis result for all sample devices, respective names are indicated upper left for each graph. Compositional atomic percentage also given in inset.

EDS spectra indicates that the samples are composed of Ti, O_2 with an atomic ratio nearly 1:2 which is expected for rutile TiO_2. Extra carbon, tin (Sn) peaks were found because of carbon tape and FTO substrate, which were detected in T5 device. The atomic weight percentages of all elements for all sample devices presented in a inset table for every graphs. Here we successfully achieved to synthesis TiO_2 nanorods for our experiment which is proved by FESEM images and EDS analysis outcome.

4.2.2.4: UV-Vis Reflectance Study – Band Gap Determination:

The optical properties absorption range as well as the band gap of the experimented sample devices were analysed by UV - Vis - NIR spectrometer (Shimadzu UV-Vis-NIR (UV-3101-PC) spectrophotometer). Here only UV-Vis reflectance study conducted. The Kubelka- Munk plot for every device shown in figure 4.9. From this technique we easily calculated the indirect band gap for every device. Calculated band gap energies are shown in table 4.2 for every device respectively.
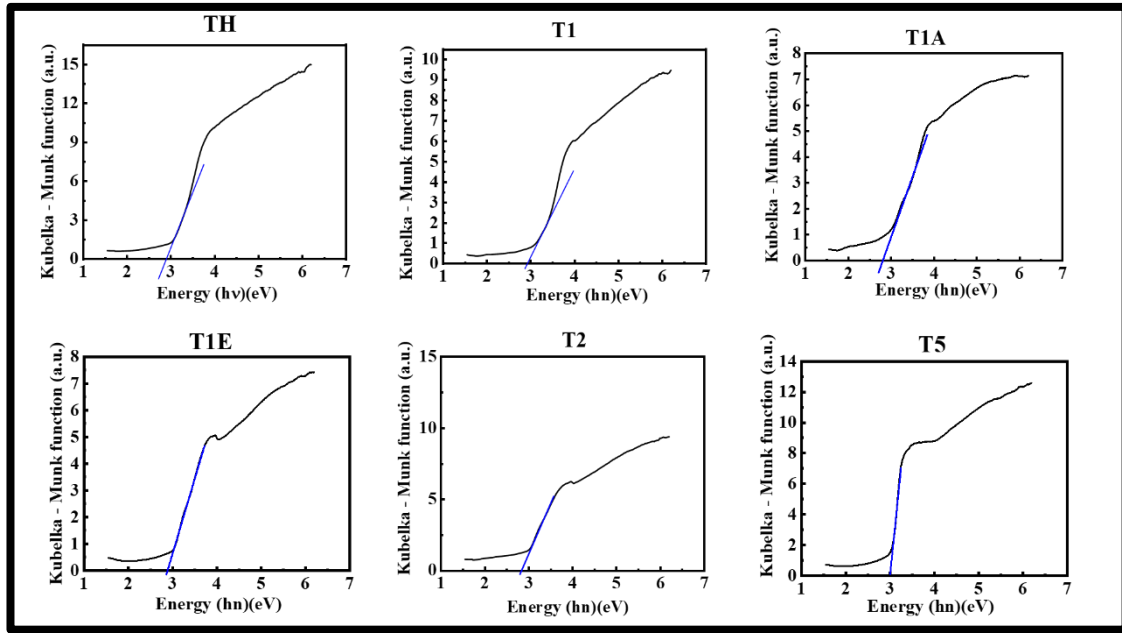
Figure 4.9: UV-Vis reflectance Kubelka – Munk plot of all respective devices.

Table 4.2: Calculated indirect band gaps of every device.

DEVICE NAME	BAND GAP (eV)
TH	2.78
T1	2.78
T1A	2.92
T1E	2.88
T2	2.84
T5	3.00

4.3: Electrical measurements:

Figure 4.10(a), (b) shows schematic and optical image of the Ag/TiO$_2$ NR/ FTO device during electrical measurement. Also figure 4.10 (c) shows only optical image of T1

device. Here only T1 device shown because of every device are identical. The I-V characteristics of six fabricated devices shown in the figure 4.11. These I-V characteristics measured under DC sweeping mode by Keysight source meter B2902A. DC seeping pulse was 0V to -2V then -2V to 0V again 0V to +2V then +2V to 0V. Extremal bias was applied to Ag top electrode whereas FTO bottom electrode were grounded during measurements. Compliance current (I_{cc}) was set at 10^{-5} A to prevent possible damage. From figure 4.11 it is clearly seen that except T1 and T2 devices all devices exhibit poor switching I-V characteristics curve. Comparison graph of On/Off current ratio of these devices also shown in figure 4.12. Comparing these two figures it is clearly noticeable that T1 device had best On/Off ratio and most permissible candidate for further studies in our case. Due to this reason, we choose T1 device as best device and performed next important examinations with it. On/Off ratio for T1 device was 8.29×10^{4}. This high On/Off current ratio indicates good retention property with low leakage current. Low leakage current is desirable in good non-volatile memory devices. For T1 device analogue bipolar resistive switching was noticed. Due to this here we could not get specific SET and RESET voltages.
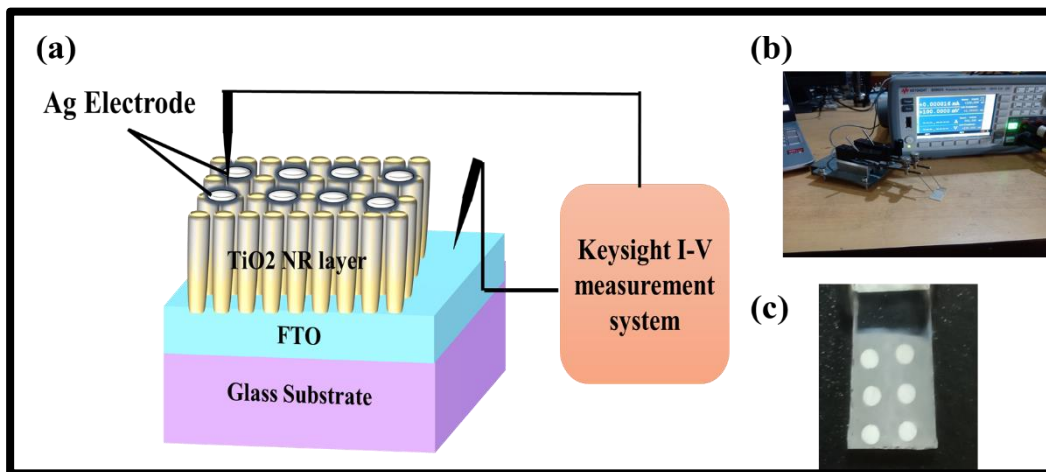
Figure 4.10: (a) Schematic diagram of T1 device under electrical measurement condition. (b) original image of experiment setup under electrical measurement, (c) optical image of T1 device.
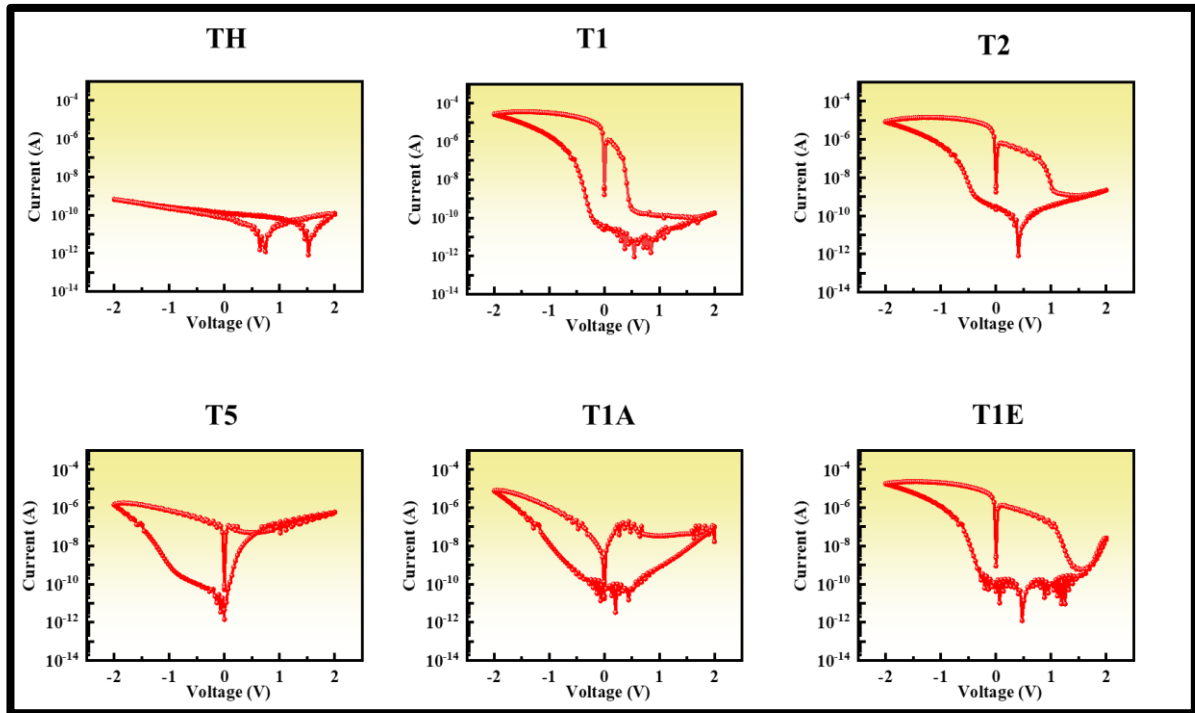
Figure 4.11: The I-V characteristics of six fabricated devices with respective device name on the top of each graph.
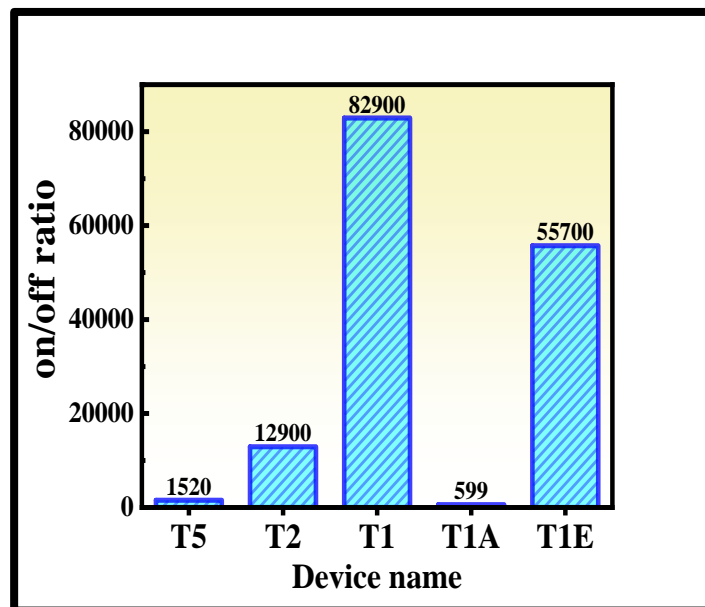

Figure 4.12: The statistical distribution of LRS and HRS currents read at – 0.25V of all sample devices.

For retention and endurance testing T1 device was examined under ambient condition with room temperature at 25 ℃. During retention testing -0.1 V read voltage applied with ac pulse of -0.1V (+0.1V) to SET(RESET). In our experiment 10^4 seconds (nearly 3 hours) was recorded as retention time for T1 device. Retention graph shown in figure 4.13 (a). T1 device also stable up to 599 cycles with prominent HRS and LRS resistance states. In figure 4.13 (b) endurance response for T1 device shown. Stable On/Off states after 10^4 continues reading cycles, signify good reproducibility and reliability of T1 device as non-volatile memory device.
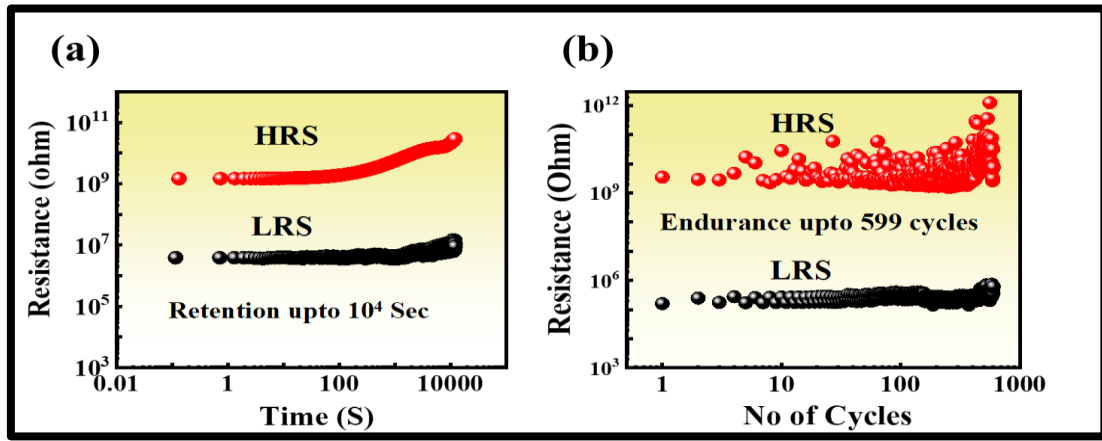
Figure 4.13: (a) Retention graph up to 10^4 sec of T1 device. (b) endurance graph up to 599 continues cycles for same device.

We also test the repetition of cycles in a single simulation with and without violet light illumination. Figure 4.14 (a), (b) shows 30 repetitive cycles and 14 repetitive cycles with and without blue light illumination, with nearly same On/Off current ratios. This repetition signifies good memory behaviour which is desirable in good non-volatile memory device. For blue light illumination case, device current increases rapidly by increasing negative bias voltage. This was happened because of photogenerated extra electrons which were more quickly trapped by oxygen vacancies and quickly formed conductive filament between top and bottom electrodes. The whole switching process for

normal and under violet light illumination discussed in later discussions. Figure 4.14 (c) describes the differences between (a) and (b) I-V graphs. Here black one for measurement under UV light and red one for normal measurement condition.
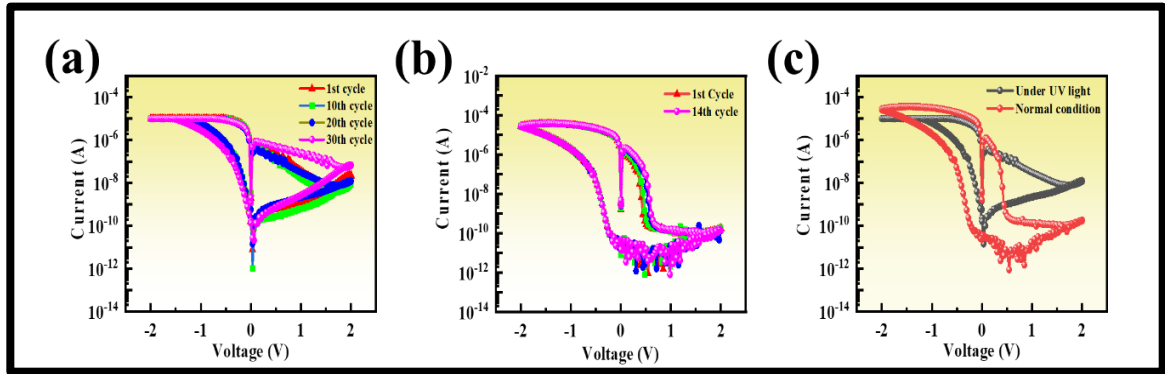

Figure 4.14: (a), (b) Repetitive I-V characteristics of T1 device under UV light and normal condition respectively, (c) comparison of previous two graphs.

> **Elaborate Explanation on Switching Process and Conduction Mechanism:**

In this segment we elaborately try to discuss the switching and carrier conduction mechanism happened in T1 device. Oxygen vacancies played vary vital role on it. [14] At the rest condition when no bias applied to the device, the device is in high resistive state (HRS). Oxygen vacancies denoted as grey circles distributed randomly as per figure 4.15 (a) in HRS condition. In our case we always connect FTO (bottom electrode) with ground terminal of the source meter. Now when we applied negative bias to top electrode then small potential gradient generated and electrons injected into active layer from top electrode and probe. Oxygen vacancies act as an electron trapping site and trapped these foreign electrons (orange circles) as per figure 4.15 (b). By increasing bias magnitude filled oxygen vacancies come closer to each other and construct conducting filament

(CF). Due to CF current increase inside the device, device switched to low resistive state (LRS) from HRS, SET process happened as per figure 4.15 (c).
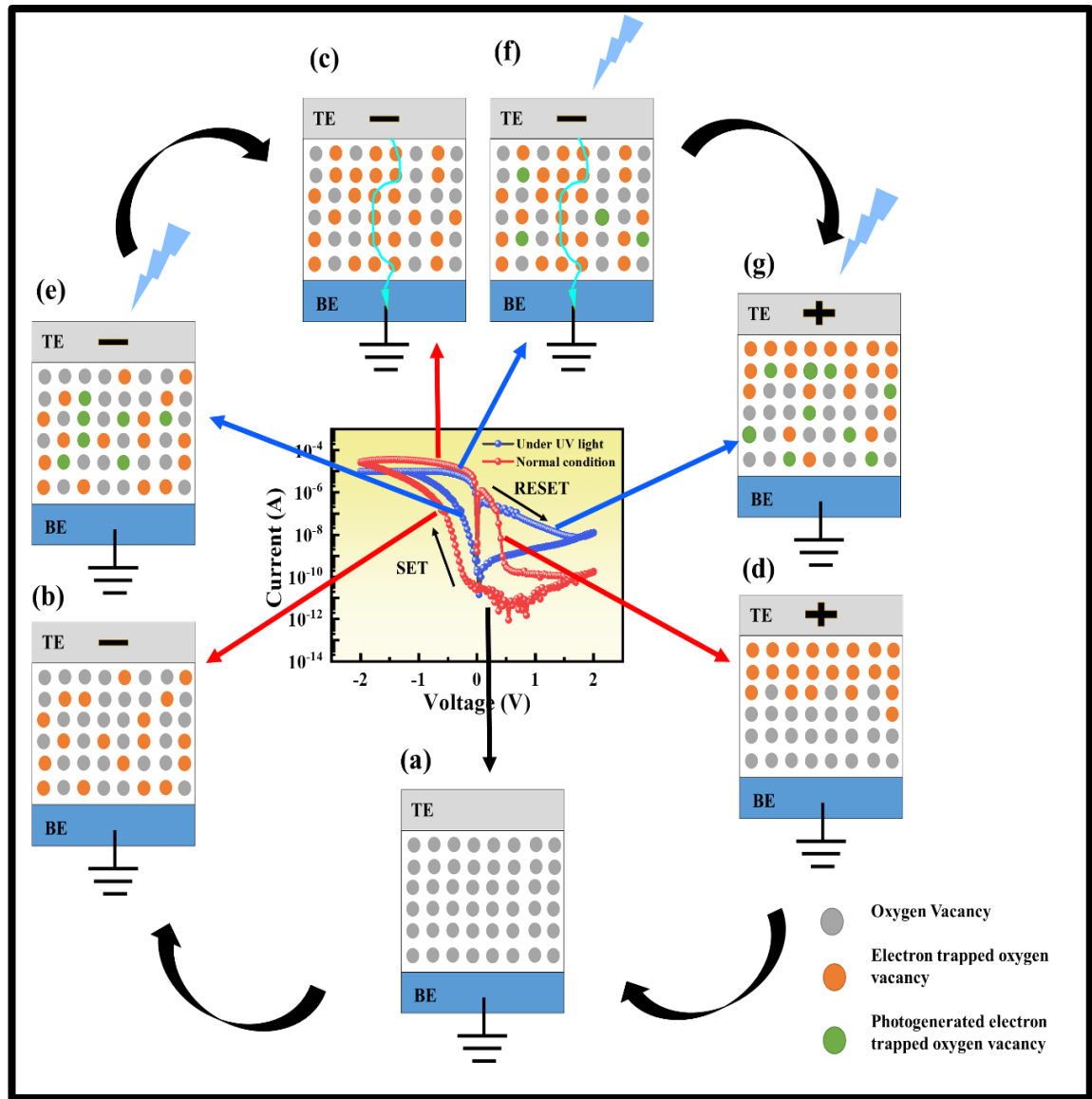

Figure 4.15: Schematic representation of switching process inside T1 device with and without blue light illumination.

Now for positive side of the graph RESET process, we applied positive bias to top electrode. For this reason, positive field withdraws the trap electrons towards top electrode and they accumulated near the same. Aa a result a capacitor like structure created as per figure 4.15 (d). Due to this a negative differential resistance (NDR) effect

has been created inside the system which was noticed in positive side of the I-V characteristics. More we applied positive bias then capacitive effect increases respectively. By increasing the positive bias, the accumulated electrons collected via top probe and device goes to HRS again.

When we applied blue light illumination (λ=405nm), extra photogenerated electrons introduced (green circles) inside active layer of the device as per figure 4.15 (e). For this reason, current sharply increases compared to previous case. Comparison graph shown in figure 4.15 I-V graph. And also due to more electron distribution in active layer, capacitor effect gone and very low NDR effect seen in latter case. Other processes executed same as previous one, respective processes schematically shown in figure 4.15 (f), (g).
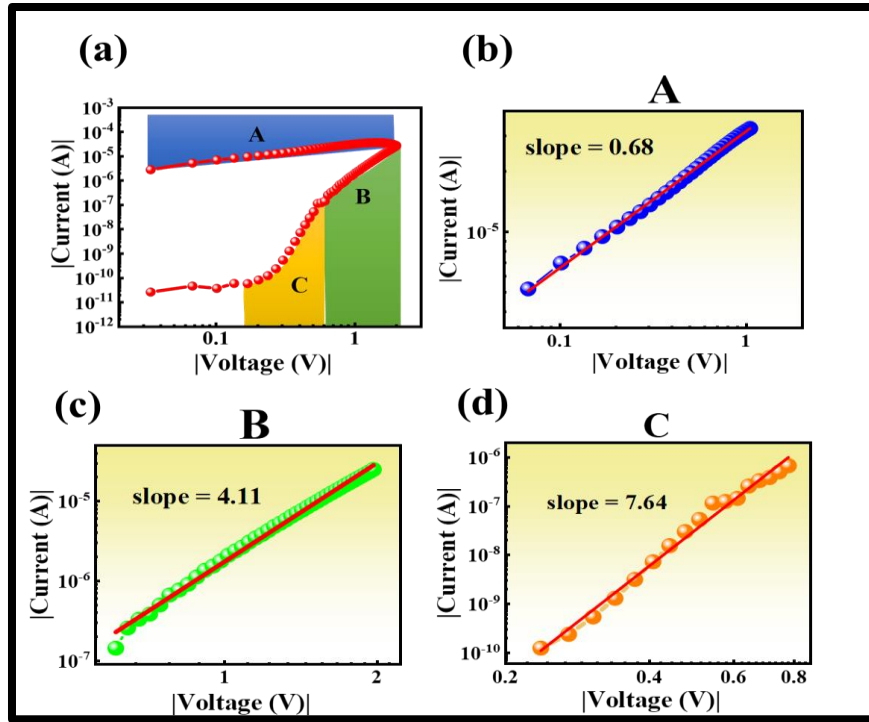
Figure 4.16: (a) log |I| vs. log |V| plot for T1 device only for negative side I-V graph, (b), (c), (d) separate plots with linear fitting with slope values for A, B, C region parts.

Height of the TiO_2 nanorods and oxygen vacancy concentration or defect concentration are the two key factor behind resistive switching conduction mechanism in TiO_2 nanorod based RS device. [15] Oxygen vacancy concentrations are responsible for set current and bipolar switching for this type of device. For getting exact description of conduction process we need to plot log |I| vs. log |V| graph. Eight types of conduction mechanisms are there by using those we can linearly fit the log |I| vs. log |V| graph. These conduction mechanisms are a) Ohmic conductance, b) Space charge limited current (SCLC), [16,17] c) Poole-Frenkel emission,[18] d) Fowler-Nordheim tunnelling,[19] e) Schottky emission,[20] f) direct tunnelling, g) hooping conductance, h) Thermionic emission. In our work oxygen vacancies contribute in switching process as we seen in above discussion, so we use SCLC mechanism to explain the I-V loop. [21] In SCLC mechanism oxygen vacancies act as electron trapping sites and can easily transport through material and also capable to form new vacancies under external electric field. [22]

We have plotted log |I| vs. log |V| graph for T1 device to determine the exact conduction process. The log |I| vs. log |V| graph for T1 device shown in figure 4.16 (a) with three separate labelled regions namely A, B, C. Further we linearly fitted those three regions separately which are shown in figure 4.16 (b), (c), (d) with corresponding slopes. Slopes of A, B, C segments are 0.67, 4.11, 7.64 respectively. From 0V to <-0.6V sweeping region electron transported from probe to top electrode to active layer via Schottky barrier of Ag/TiO_2 NRs due to difference between work function of Ag electrode (4.3eV) and Fermi level of TiO2 NRs (rutile) (4.2eV). Electrons and oxygen vacancies obstructed by this barrier and for this reason some small rectifying current noticed in HRS region in the I-V loop. Slope of C segment was 7.64 which was signifies trap filled SCLC and we discussed in above discussion that when we increased the voltage reversely form 0V to -

2V then electrons started to trapped by oxygen vacancies. This C segment described by trap filled SCLC mechanism. From -0.6V to -2V, concentration of filled oxygen vacancies were increased and creates channels for fast electron transport. Due to this reason slope of segment B (4.11) falling under SCLC mechanism. The device switched to LRS from HRS after formation of conducting filament by electron filled oxygen vacancies. This situation additionally triggered the formation of oxygen vacancies in active layer. By this process new vacancies contributed to making conductive filament more prominent and device was in LRS. [23] Voltage from -2V to 0V device was in LRS and conducts current like conductor for this reason slope of segment A was 0.67 which was comparably near 1 and mechanism was Ohmic conductance.

We did not determine the conductance mechanisms for RESET process. In positive side due to capacitance effect NDR noticed and RESET was not prominent. But we discussed the reason behind the nature of I-V loop for positive side in our previous discussion when we try to illustrate a switching mechanism for T1 device.

4.4: Synaptic Functions Emulated on T1 Device:

Now we discuss about T1 device examined as artificial synapse via both electrical and optical inputs. In artificial synapse conductance value is associated with synaptic weight of biological synapse. This conductance value depends on number of pulses, repetition of intervals, number of repetitions, pulse magnitude, pulse width and relative time between pre and post synaptic currents. During learning process in biological synapse synaptic weight increases, similarly conductance (current) increases in artificial counterpart. For forgetting process opposite phenomenon happens. Behind good learning process long term potentiation plays a vital role. Other types of synaptic functions are STDP (Spike Time Dependent Plasticity), SRDP (Spike Rate Dependent Plasticity), PPF (Paired pulse Facilitation), PPD (Paired Pulse Depression). STDP associated with relative time interval

of pre and post synaptic pulses. SRDP associated with frequency of input pre synaptic pulse. [24]

> **Long-Term Potentiation (LTP) and Long-Term Depression (LTD):**

Learning and forgetting process of biological synapse emulated on T1 device as LTP and LTD. Figure 4.17 (a) shows LTP and LTD response of T1 device. 300 continuous negative input pulses each of amplitude = -2V, measure delay = 0.05 sec, T_{off} = 21ms, T_{on} = 1ms are applied shown in figure 4.17 (b). Current value increases after each pulse due to trapping of electrons by oxygen vacancies and migration from FTO to Ag electrode. For this reason, conductive filament width increases with time and then current increased. It is LTP (Long Term Potentiation) response of T1 device. Here all electrical measurements were done in negative SET region due to this negative voltage pulse applied for potentiation. Similarly for depression study we applied same but positive pulses. And from the graph it is clearly noticed that in depression study current decreases gradually which signifies LTD (Long Term Depression). In LTD conductive filament started to ruptured and oxygen vacancies started to de trapped.
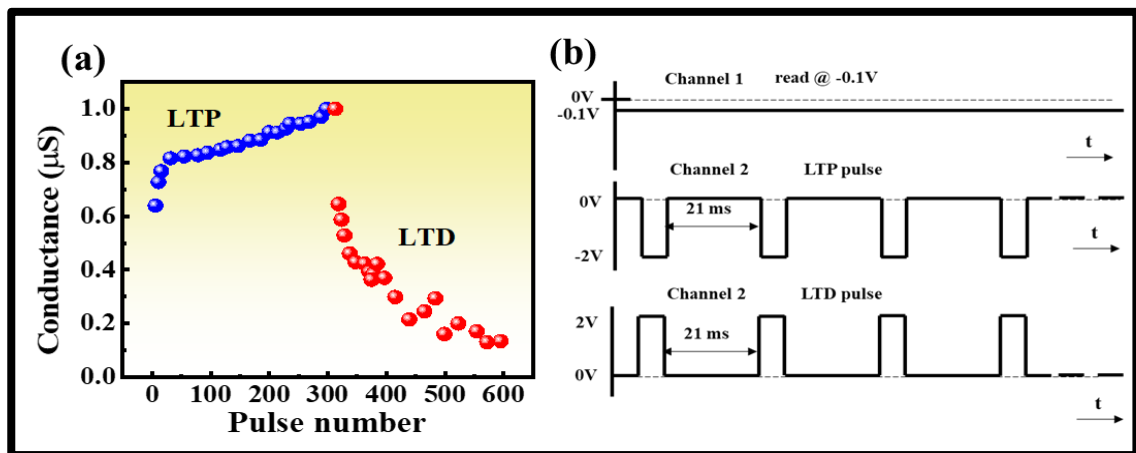
Figure 4.17: (a) LTP and LTD response of T1 device, (b) Measurement pulses used via two channel method.

110

➢ **Spike Time Dependent Plasticity (STDP):**

Synaptic weights modulated by changing relative time of pre and post synaptic spikes in biological synapse. [25] STDP governed by Hebbian rules. Four different Hebbian rules are there, a) Symmetric Hebbian, b) Symmetric anti Hebbian, c) Asymmetric Hebbian, d) Asymmetric anti Hebbian. In T1 device only Symmetric Hebbian type STDP response observed, other three were not observed for this device. According to Hebbian rule if two neurons wired together then they should fire together. [26] The graphical result is shown in the figure 4.18 (a). ΔW% is the change of conductance,

$$\Delta w\% = \frac{G_2 - G_1}{G_1} \times 100$$

G_2 = conductance after simulation

G_1 = initial conductance

Maximum synaptic weight (conductance) change occurs at Δt = 0. If pre spike and post synaptic spike fired at a time, then maximum conductance change noticed. The applied pre and post synaptic spikes are shown in figure 4.18(b) with respective values and notations. The data points fitted using Gaussian curve fitting.
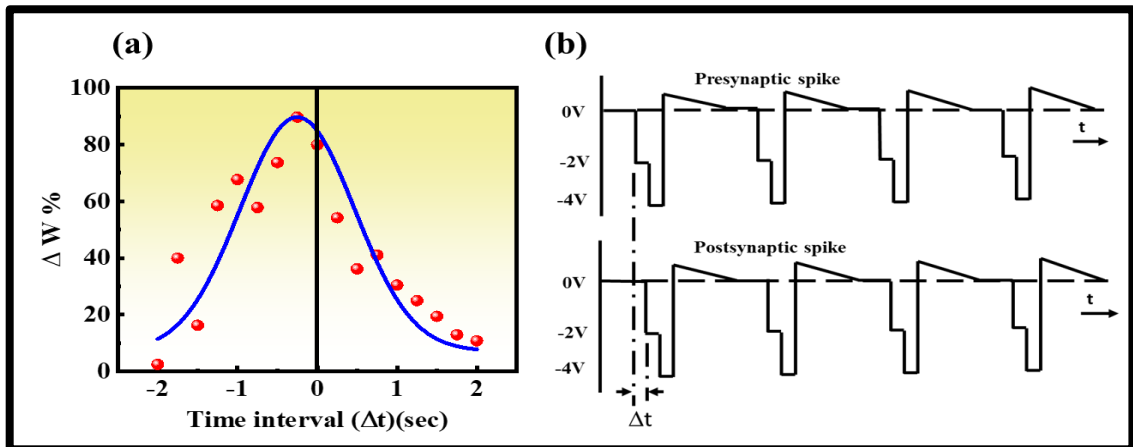
Figure 4.18: (a) STDP response of T1 device, (b) pre and postsynaptic spikes used in STDP measurement.

➢ **Spike Rate Dependent Plasticity (SRDP):**

In SRDP conductance or synaptic weight changes with respect to frequency of presynaptic spike. Here only presynaptic spike applicable. It is also an important learning process in our brain. [27-29] In T1 device we employed 1, 3, 5, 10 Hz presynaptic spike signals to Ag electrode. From figure 4.19 (a), it is seen that current gain increases with increase in frequency like biological counterpart. Here -0.5V read voltage applied. Applied presynaptic pulse shown in figure 4.19 (b) with respective values. An illustrative schematic diagram shown in figure 4.22 in terms of biological synapse.
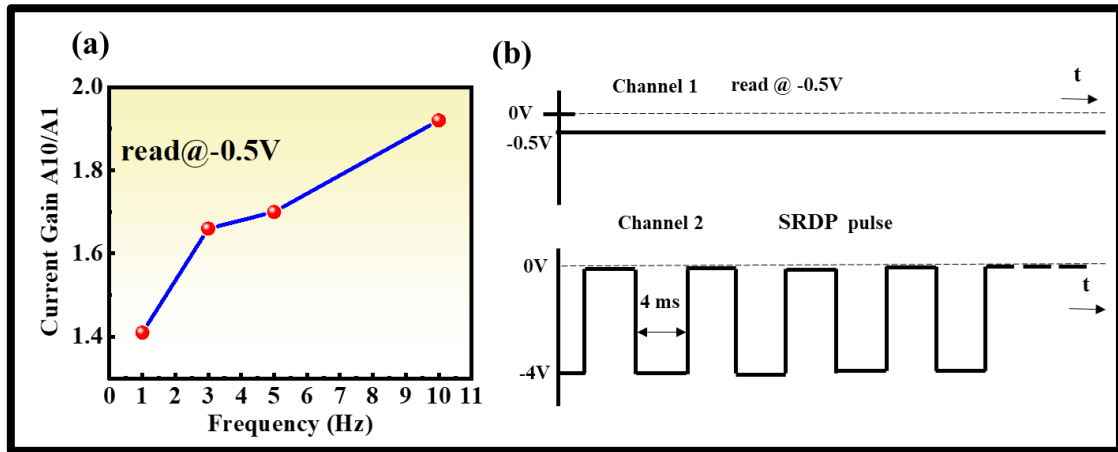
Figure 4.19: (a)SRDP response of T1 device, (b) schematic representation of

measurement pulses.

❖ **Optical Long-Term Memory:**

As we mentioned earlier our device T1 capable to give response under blue light illumination (λ = 405 nm blue laser), so; we also examined synaptic functions by optical input. Optical long-term memory achieved in T1 device and corresponding graph shown in figure 4.20 (a). Here optical pulse duration of 30 sec and light power was 45mW/cm^2, off time 120 sec applied. Under illumination condition charge carriers produced by photogeneration process, current increases. When light is off current decreases gradually

because recombination process of photogenerated carriers. [30] Here, -0.3V read voltage applied. The schematic representation of applied light pulse with respective values shown in figure 4.20 (b). Synaptic weight in term of current increases with time denoted by arrow sign. This response is analogous with electrical synapse.
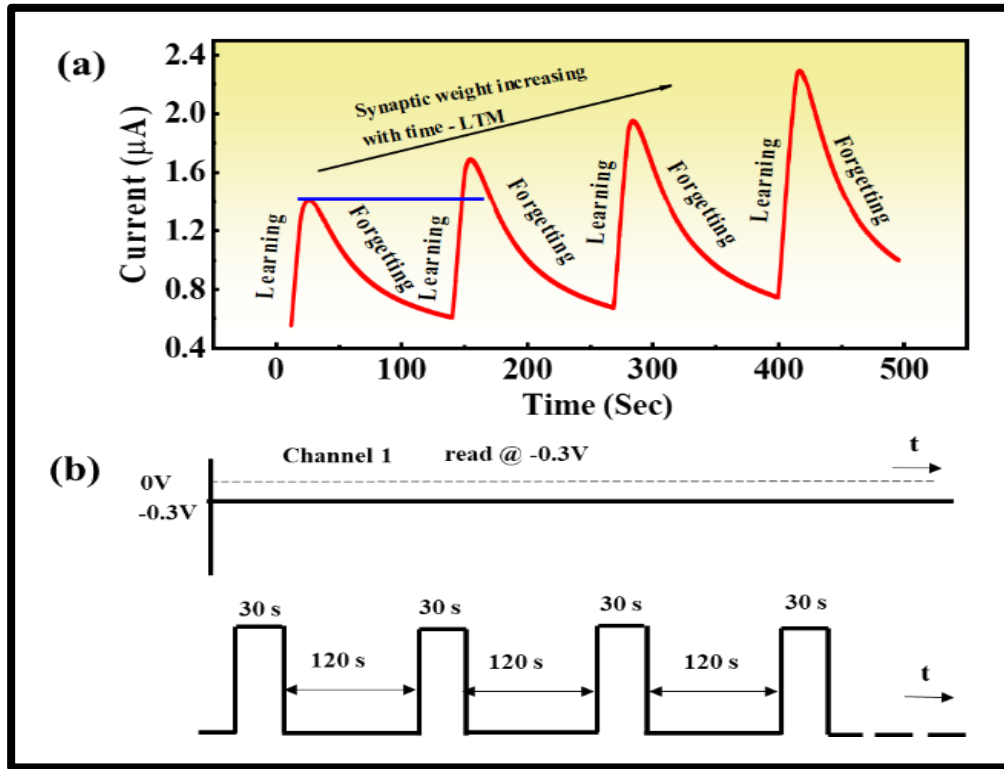

Figure 4.20: (a) Optical response of T1 device under 47 mW/cm^2 blue light ($\lambda = 405$nm) illumination and LTM achieved by Learning – forgetting – relearning mechanism of human brain, (b) measurement pulses (optical and electrical).

Long term memory also obtained by varying the intensity of applied light source. By using this graph another important human learning mechanism described. Cognitive learning in human brain divided into three parts, learning, forgetting, relearning. in relearning process people learn previous things again but less effort needed to reach

previous level of knowledge. And total knowledge increased after relearning process. Under light pulse current gradually increases, represents learning process. When light off, current decreases gradually, denotes forgetting process. And in next light on state current increases denoted as relearning process. In the graph, peak value of 1st learning process marked by blue line for reference. In relearning phase current cross that line but other parameters are same. So, synaptic weight (current) increased, knowledge increased. [31]

➢ **Paired Pulse Facilitation (PPF) and Paired Pulse Depression (PPD):**

PPF studied by applying paired pulses with different on time (pulse width variation) (5, 10, 30, 60, 120 sec) and 47mW/cm^2 power blue laser (λ = 405nm). Two types of PPF study carried out one for pulse width variation and another for intensity variation. Paired pulses with low pulse width produces low EPSC (excitatory post synaptic current) and pair pulses with high pulse width produces high EPSC. Same phenomenon for intensity variation study. Two graphs are shown in figure 4.21(a), (b). Percentage PPF can be calculated as, [32,33]

$$PPF\% = \left(\frac{I_2 - I_1}{I_1}\right) \times 100$$

I_1 = EPSC for first pulse
I_2 = EPSC for second pulse

PPF% is maximum for 120 sec on time pulse and minimum for 5 sec on time pulse.

PPD studied by different off time (intervals) light pulses. PPD% graph also shown in figure 4.21 (c). By increasing interval between two pulses EPSC decreased. All graphs are fitted for better understanding. An illustrative schematic diagram shown in figure 4.22 in terms of biological synapse.
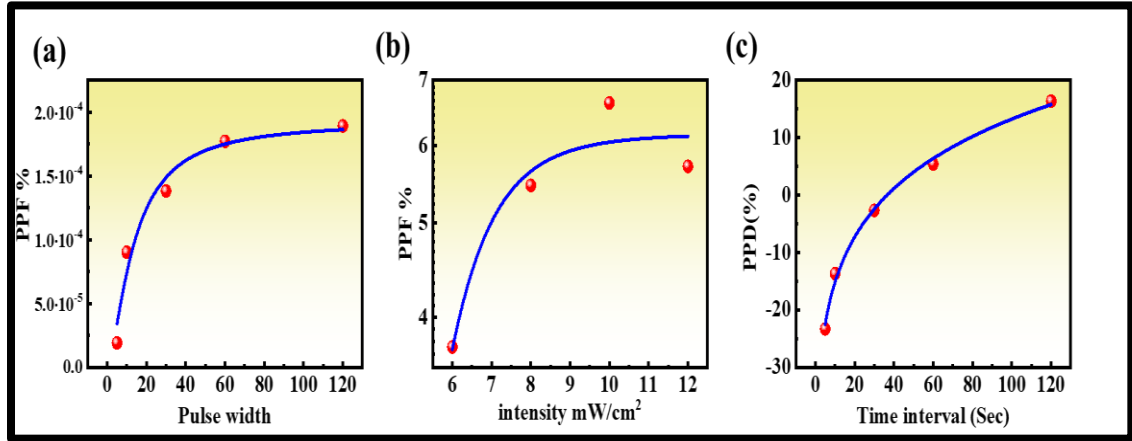
Figure 4.21: (a) PPF response of T1 device with pulse width variation, (b) PPF response with light intensity variation, (c) PPD response with time interval variation of two consecutive presynaptic optical pulses.
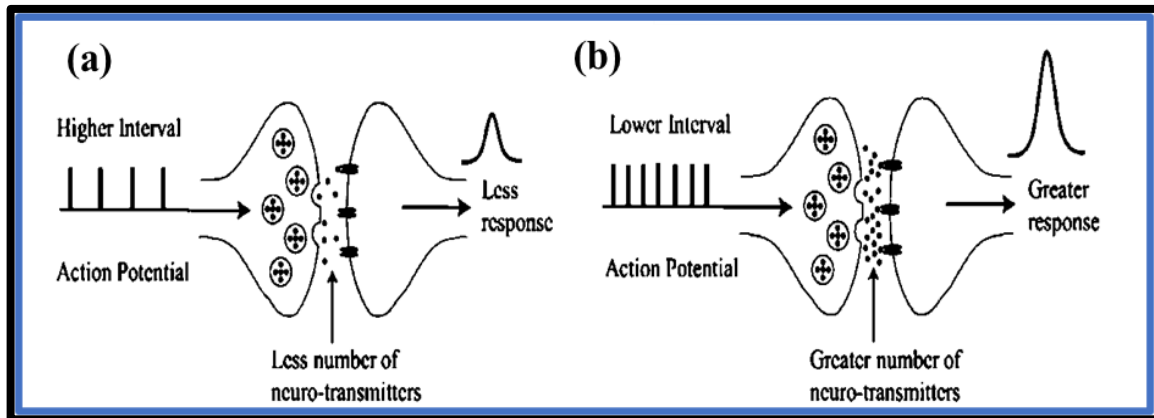

Figure 4.22: (a), (b) Schematic representation of PPF and SRDP, when interval is high (frequency low) then postsynaptic current will be low, opposite for low interval (high frequency). (adopted from internet)

4.5: T1 Device Used as Artificial Retina with Machine Learning:

In a camera there are three main parts namely, silicon-based CMOS sensor which sense the input incoming lights from object, field programmable gate arrays which converts input light intensities into spike signal and inbuilt software program which process that spike signals into human understandable output image. Due to expensive CMOS technology researchers trying to find new technology with new nanomaterials. [34]

In our experiment we used T1 device to make a working model of whole camera system with image recognition feature. Our aim is to build artificial retina with robotic vision system. T1 device was employed to emulate sensing and pre-processing features of biological retina. A schematic representation of human vision system is shown in figure 4.23. Here light from real object or image entering into eye via lens and make an inverted replica of input object on retina. By chemical changes rod and cone cells of retina generates sensory spike signals which goes to occipital lobe in cerebral cortex region of brain. In occipital lobe these spike signals processed and recognised. Similar to this mechanism we developed our artificial robotic visual system with the help T1 (as artificial retina) device and machine learning algorithm. The schematic representation shown in figure 4.24.
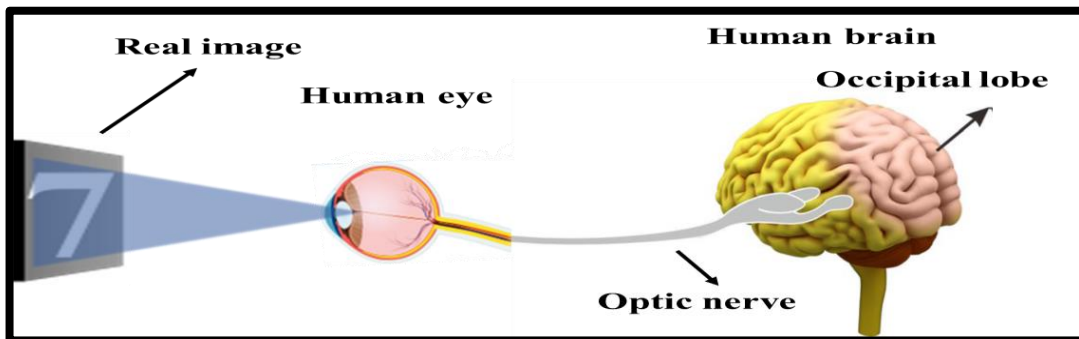

Figure 4.23: Schematic diagram of human vision system. (reproduction of the internet image)
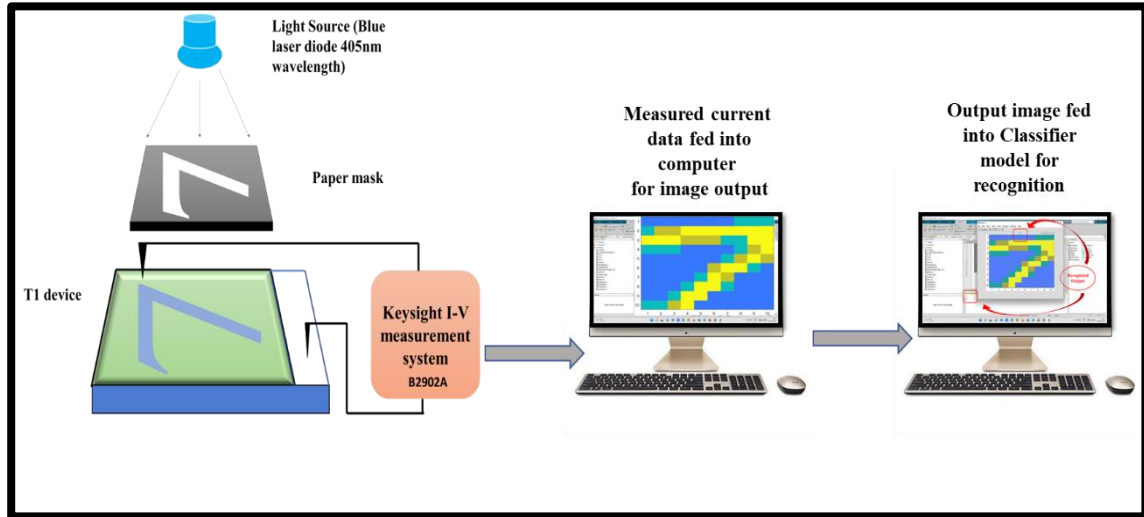
Figure 4.24: Schematic representation of artificial vision model by T1 device, replication of biological vision system.

T1 device act as artificial retina and sense the incident light intensity also produce corresponding current outputs. In figure 4.25 (a), blue line highlighted area denoted the unmask area on the T1 device. When we applied blue light means when we applied light stimulus the current increases in illuminated cells but current not increased in masked cells. This is schematically shown by figure 4.25 (b). An original output image for **"7"** digit mask in terms of current response shown in figure 4.25 (c).
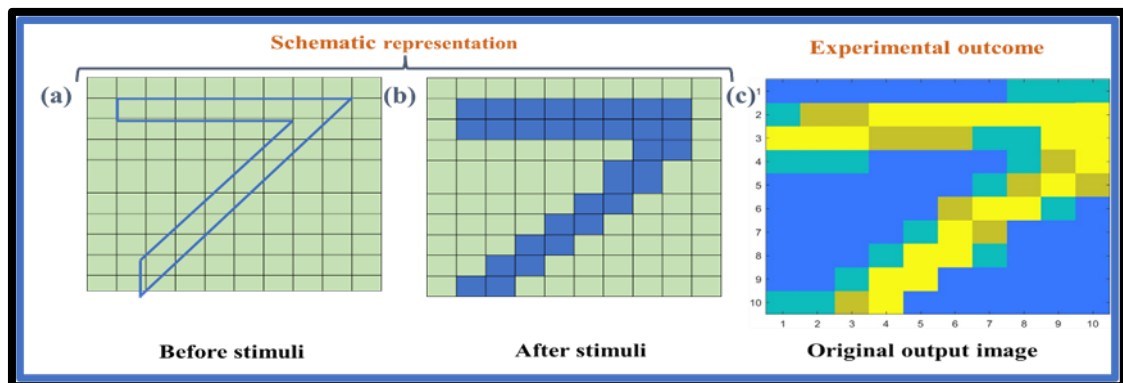
Figure 4.25: (a) Device current states before light stimulus, (b) device current changes for unmasked pixels after stimulus applied, (c) experimental output image with different current values for mask and unmask pixels.

These current outputs associated with each unique pixels of input paper mask (image). For dark portion of the image low current and for lighted portion high current generated. After getting these current values we fed it into MATLAB program for getting human understandable output image. Three different output images are shown in figure 4.26 for three different testing results. We first test **"7"** and then **"M"** as image. **"M"** tested for two times to examined the pre-processing characteristic of human retina. It is clearly seen that by twice simulation image quality improves.
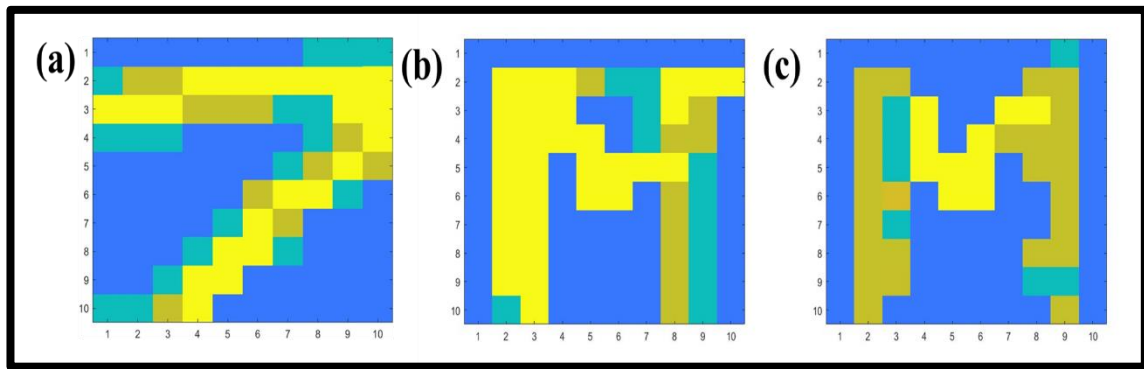
Figure 4.26: (a), (b), (c) three different output images with different mask.

After that we fed these images into Support vector Machine (SVM) linear classifier led by HOG (Histogram of Oriented Gradients) feature machine learning program for recognition purpose. The flowchart of whole Classifier model and simulation process shown in figure 4.27. The outputs of recognition process shown in the figure 4.28. It is clear that our SVM classifier model successfully recognised these output images. We manually prepared 110 grey scale handwritten images of digits and few alphabets with 28*28-pixel values. Irrespective of pixel values our SVM linear classifier model easily recognised test output images. It strongly supports advance vision sensing and recognition process like human vision system.
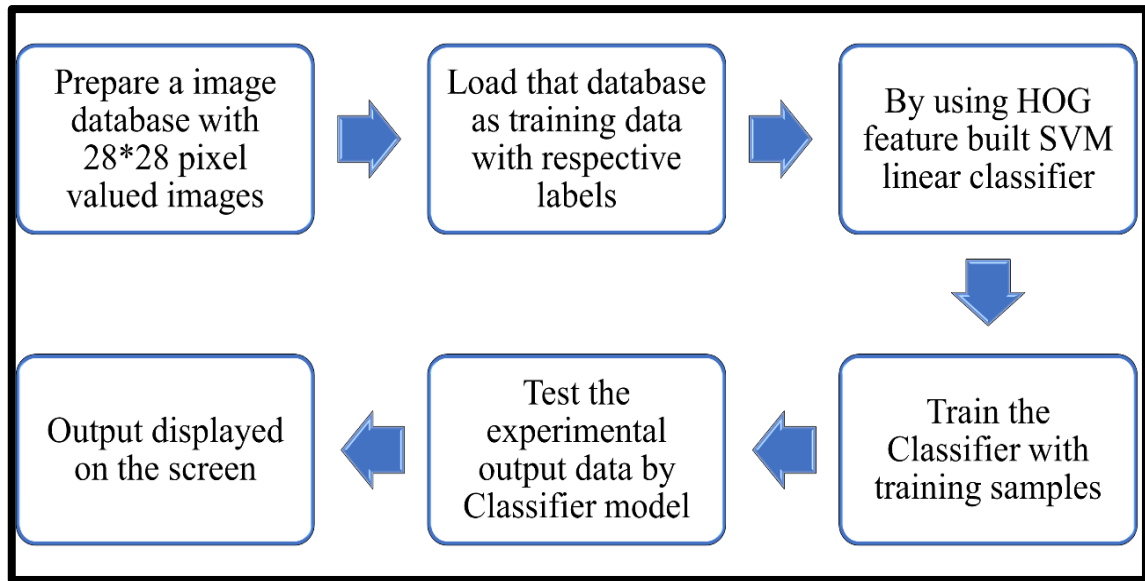
Figure 4.27: Flowchart of whole Classifier model and simulation process used in this experiment.
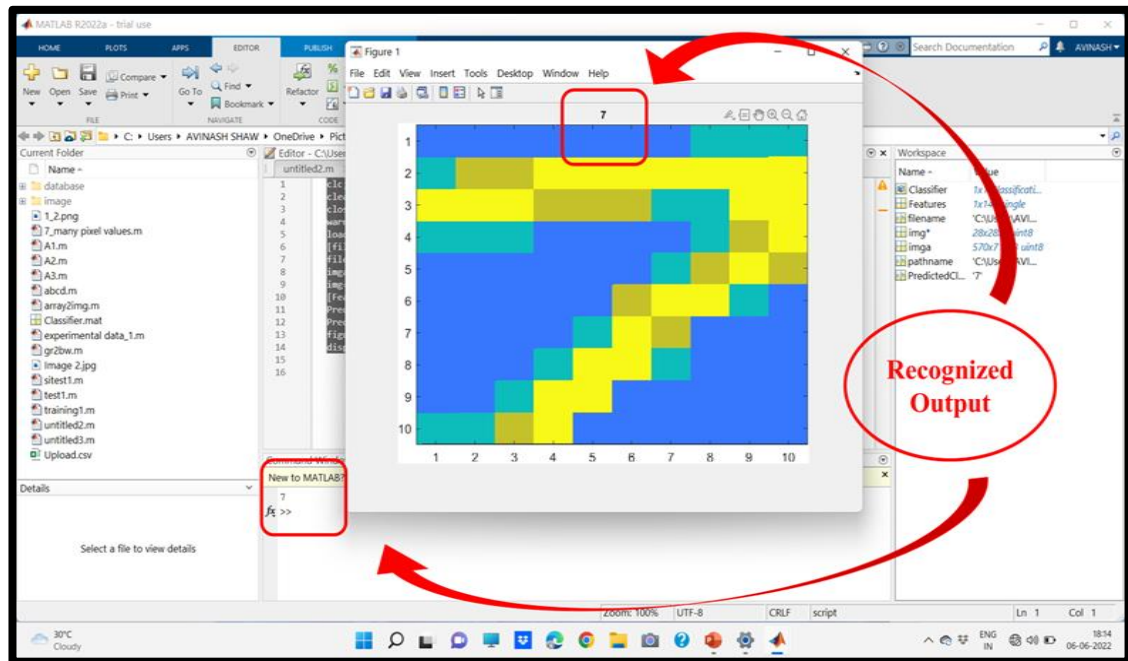

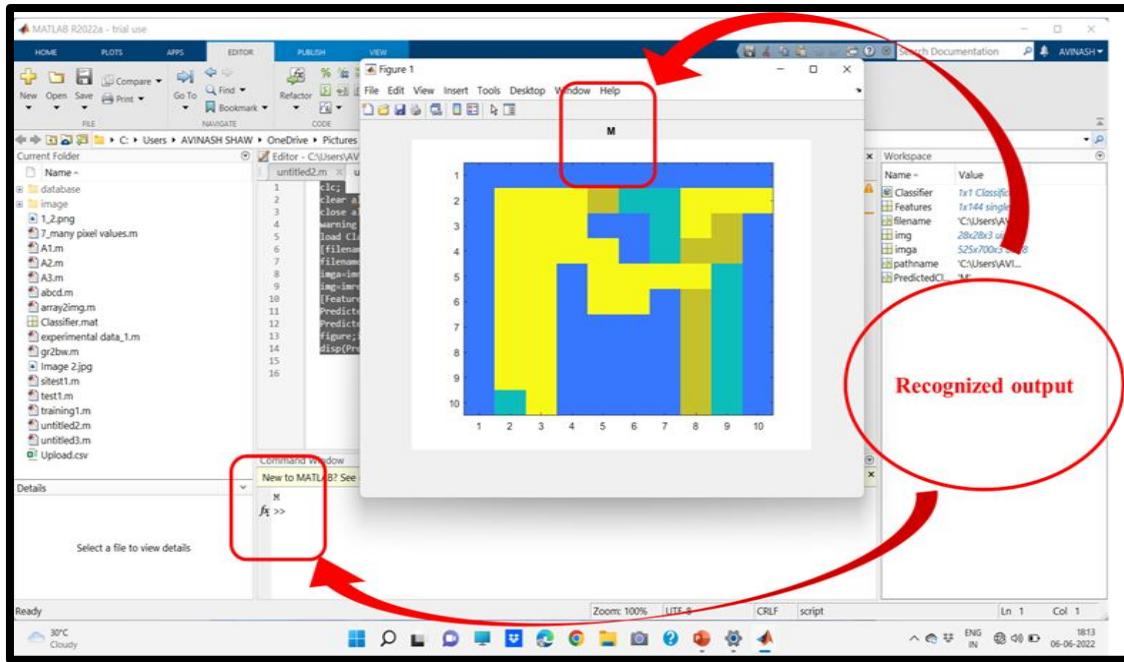**Figure 4.28**: (a) Simulation output after recognition from Classifier model when **"7"** digit mask used.

Figure 4.28: (b) Simulation output after recognition from Classifier model when **"M"**
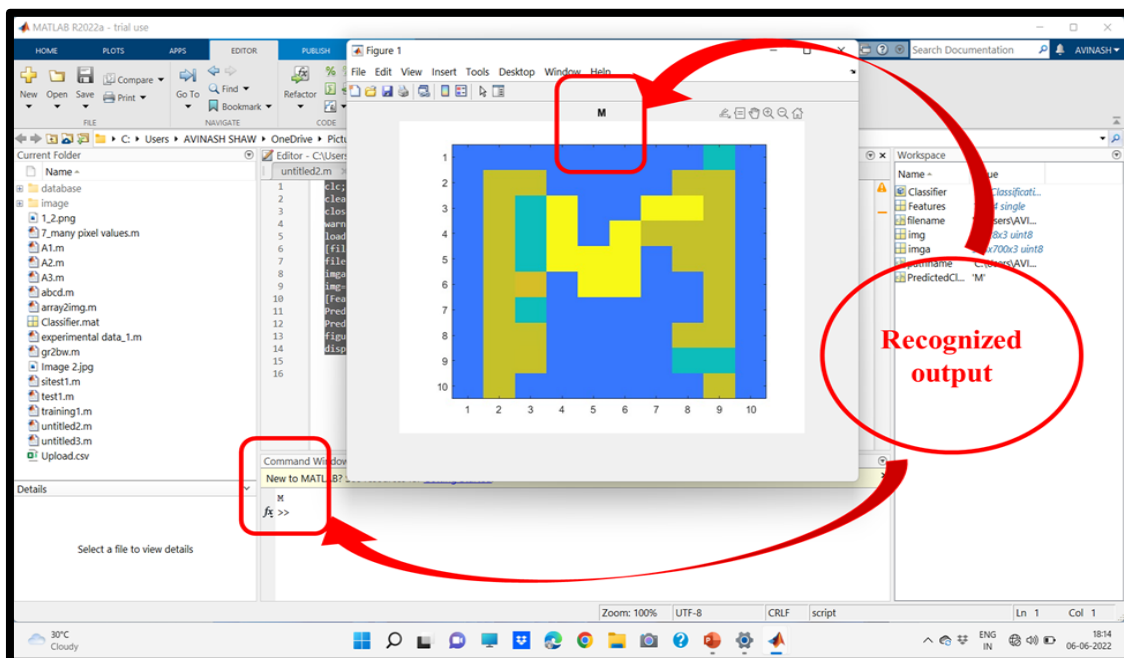
digit mask used. (First simulation)

Figure 4.28: (c) Simulation output after recognition from Classifier model when **"M"**

digit mask used. (2nd simulation)

Now we can say that our T1 device successfully examined as artificial retina and our whole artificial vision model can be used as robotic vision system.

4.6: Conclusion:

In conclusion, we have successfully demonstrated synthesis of TiO$_2$ nanorod arrays on FTO coated glass substrate via low cost, less complicated hydrothermal route. In this chapter, synthesis time variation scheme adopted to see difference results in RS behaviour. We have selected T1 device as our best device based on low and high resistive state current ratio. We also elaborately discussed the probable switching mechanism with respective carrier conduction mechanisms. We have successfully examined all types of synaptic properties with both electrical and optical inputs on T1 device. It is established that our T1 device has capability to applicable in neuromorphic device applications for both electrical and optical input signals. We successfully made a machine learning classifier model and test our device as an artificial vision sensor. Our classifier model capable to convert T1 device output current response to real world image output with accurate recognition of that with similar learning inputs.

4.7: Reference:

[1] Waser, R. & Aono, M. Nanoionics-based resistive switching memories. *Nat Mater* **6**, 833–840, doi:10.1038/nmat2023 (2007).

[2] Sawa, A. Resistive switching in transition metal oxides. *Materials Today* **11**, 28–36, doi:10.1016/S1369-7021(08)70119-6 (2008).

[3] Waser, R., Dittmann, R., Staikov, G. & Szot, K. Redox-Based Resistive Switching Memories – Nanoionic Mechanisms, Prospects, and Challenges. *Advanced Materials* **21**, 2632–2663, doi:10.1002/adma.200900375 (2009).

[4] Yang, J. J., Strukov, D. B. & Stewart, D. R. Memristive devices for computing. *Nat Nano* **8**, 13–24, doi:10.1038/nnano.2012.240 (2013).

[5] F. Zhang, X. Gan, X. Li, L. Wu, X. Gao, R. Zheng, Y. He, X. Liu, R. Yang, Realization of rectifying and resistive switching behaviours of TiO2 nanorod arrays for non-volatile memory, Electrochem. Solid-State Lett. 14 (2011) H422–H425.

[6] Yantao Yu, Chunqi Wang, Chao Jiang, Isaac Abrahams, Zuojuan Du, Qiancheng Zhang, Jia Sun, Xiaozhong Huang, Resistive switching behavior in memristors with TiO2 nanorod arrays of different dimensions, Applied Surface Science, Volume 485, 2019, Pages 222-229, ISSN 0169-4332.

[7] A., L., Patterson. (1939). The Scherrer Formula for X-Ray Particle Size Determination. Physical Review, 56(10), 978-982. doi: 10.1103/PHYSREV.56.978.

[8] X. Feng, K. Shankar, O.K. Varghese, M. Paulose, T.J. Latempa, C.A. Grimes, Vertically aligned single crystal TiO2 nanowire arrays grown directly on transparent conducting oxide coated glass: synthesis details and applications, Nano Lett. 8 (2008) 3781–3786.

[9] X. Feng, K. Zhu, A.J. Frank, C.A. Grimes, T.E. Mallouk, Rapid charge transport in dye-sensitized solar cells made from vertically aligned single-crystal rutile TiO2 nanowires, Angew. Chem. 124 (2012) 2781–2784.

[10] Z. Wei, Y. Yao, T. Huang, A. Yu, Solvothermal growth of well-aligned TiO2 nanowire

arrays for dye-sensitized solar cell: dependence of morphology and vertical orientation upon substrate pretreatment, Int. J. Electrochem. Sci. 6 (2011) 1871–1879.

[11] Y. Zhang, C. Han, G. Zhang, D.D. Dionysiou, M.N. Nadagouda, PEG-assisted synthesis of crystal TiO2 nanowires with high specific surface area for enhanced photocatalytic degradation of atrazine, Chem. Eng. J. 268 (2015) 170–179.

[12] E. Hosono, S. Fujihara, K. Kakiuchi, H. Imai, Growth of submicrometer-scale rectangular parallelepiped rutile TiO2 films in aqueous TiCl3 solutions under hydrothermal

conditions, J. Am. Chem. Soc. 106 (2004) 7790–7791.

[13] J. Yu, G. Wang, B. Cheng, M. Zhou, Effects of hydrothermal temperature and time on the photocatalytic activity and microstructures of bimodal mesoporous TiO2 powders, Appl. Catal., B 69 (2007) 171–180.

[14] K. Szot, M. Rogala, W. Speier, Z. Klusek, A. Besmehn, R. Waser, TiO2-a prototypical memristive material, Nanotechnology 22 (2011) 254001.

[15] T.D. Dongale, S.S. Shinde, R.K. Kamat, K.Y. Rajpure, Nanostructured TiO2 thin film memristor using hydrothermal process, J. Alloys Compd. 593 (2014) 267-270.

[16] Y.D. Xia, W.Y. He, L. Chen, X.K. Meng, Z.G. Liu, Field-induced resistive switching based on space-charge-limited current, Appl. Phys. Lett. 90 (2007) 022907–022909.

[17] T. Harada, I. Ohkubo, K. Tsubouchi, H. Kumigashira, T. Ohnishi, M. Lippmaa, Y. Matsumoto, H. Koinuma, M. Oshima, Trap-controlled space-charge-limited current mechanism in resistance switching at Al/Pr0.7Ca0.3MnO3 interface, Appl. Phys. Lett. 92 (2008) 222113.

[18] H. Hirashima, Y. Watanabe, T. Yoshida, Switching of TiO2-V2O5-P2O5 glasses, J. Non-Cryst. Solids 95 (1987) 825–832.

[19] E.W. Lim, R. Ismail, Conduction mechanism of valence change resistive switching memory: a survey, Electronics 4 (2015) 586–613.

[20] T. You, N. Du, S. Slesazeck, T. Mikolajick, G. Li, D. Buerger, I. Skorupa, H. Stoecker, B. Abendroth, A. Beyer, K. Volz, O.G. Schmidt, H. Schmidt, Bipolar electric field enhanced trapping and detrapping of mobile donors in BiFeO3 memristors, ACS Appl. Mater. Interfaces 6 (2014) 19758–19765.

[21] M. Xiao, K.P. Musselman, W.W. Duley, Y.N. Zhou, Reliable and low-power multilevel resistive switching in TiO2 nanorod arrays structured with a TiOx seed layer, ACS Appl. Mater. Interfaces 9 (2017) 4808–4817.

[22] X.W. He, Y.L. Yin, J. Guo, H.J. Yuan, Y.H. Peng, Y. Zhou, D. Zhao, K. Hai, W.C. Zhou, D.S. Tang, Memristive properties of hexagonal WO3 nanowires induced
by oxygen vacancy migration, Nanoscale Res. Lett. 8 (2013)

[23] J. Joshua Yang, F. Miao, M.D. Pickett, D.A. Ohlberg, D.R. Stewart, C.N. Lau, R.S. Williams, The mechanism of electroforming of metal oxide memristive switches, Nanotechnology 20 (2009) 215201.

[24] Subin, P.S., Asha, A.S., Saji, K.J. et al. Spike-dependent plasticity modulation in TiO2-based synaptic device. J Mater Sci: Mater Electron 32, 13051–13061 (2021).

[25] C. Zamarre~no-Ramos, L.A. Camu~nas-Mesa, J.A. Pe´rez-Carrasco, T. Masquelier, T. Serrano- Gotarredona, B. Linares Barranco, On spike-timing-dependnet-plasticity,

memristive devices, and building a self-learning visual cortex. Front. Neurosci. 5, 26 (2011).

[26] C. Zamarre~no-Ramos, L.A. Camu~nas-Mesa, J.A. Pe´rez-Carrasco, T. Masquelier, T. Serrano- Gotarredona, B. Linares-Barranco, On spike-timing-dependnet-plasticity, memristive devices, and building a self-learning visual cortex. Front. Neurosci. 5, 26 (2011)

[27] S. Song, K.D. Miller, L.F. Abbott, Nat. Neurosci. 3, 919 (2000).

[28] S. Li, F. Zeng, C. Chen, H. Liu, G. Tang, S. Gao, C. Song, Y. Lin, F. Pan, D. Guo, J. Mater. Chem. C 1, 5292 (2013).

[29] Y. Zhang, Z. Zeng, and S. Wen, in 2014 Int. Jt. Conf. Neural Networks, pp. 2226–2233 (2014).

[30] D. Li, C. Li, N. Ilyas, X. Jiang, F. Liu, D. Gu, M. Xu, Y. Jiang, W. Li, *Adv. Intell. Syst.* **2020**, *2*, 2000107.

[31] Lei, P. X., Duan, H., Qin, L., Wei, X. H., Tao, R., Wang, Z. G., Guo, F., Song, M. L., Jie, W. J., Hao, J. H., High-Performance Memristor Based on 2D Layered BiOI Nanosheet for Low-Power Artificial Optoelectronic Synapses. *Adv. Funct. Mater.* 2022, 32, 2201276. https://doi.org/10.1002/adfm.202201276.

[32] R.S. Zucker, W.G. Regehr, Annu. Rev. Physiol. 64, 355 (2002)

[33] Subin, P.S., Asha, A.S., Saji, K.J. *et al.* Spike-dependent plasticity modulation in TiO$_2$-based synaptic device. *J Mater Sci: Mater Electron* **32,** 13051–13061 (2021). https://doi.org/10.1007/s10854-021-05710-2.

[34] Zhou, F., Zhou, Z., Chen, J. *et al.* Optoelectronic resistive random-access memory for neuromorphic vision sensors. *Nat. Nanotechnol.* **14,** 776–782 (2019).

Determination of Nonlinear Refractive Index (n_2) and Third Order Susceptibility $(\chi^{(3)})$ for RbPbI$_3$ Nanorods in Different Solvents Using SSPM Method
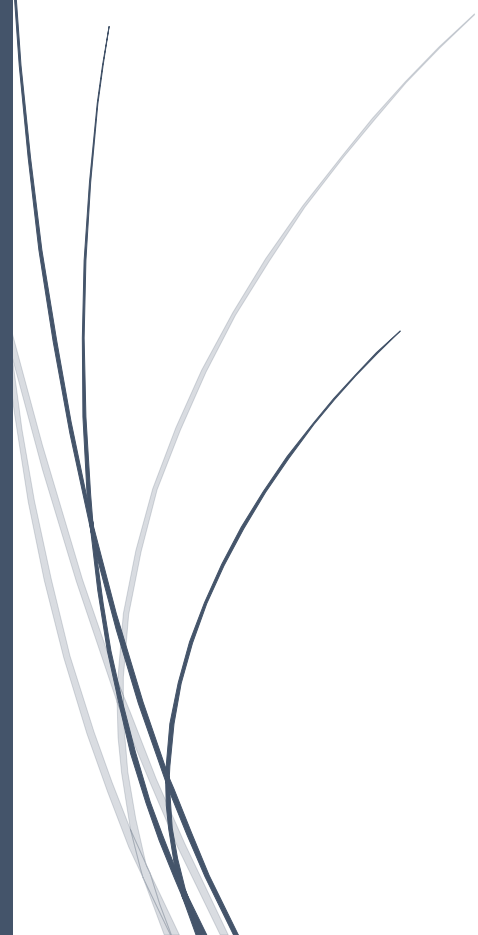
5.1. Introduction:

The terminology Spatial Self-Phase Modulation (SSPM) refers to the phase modulation of an optical field traveling through an optical medium caused by the spatial distribution of the applied intensity and the optical medium's unique nonlinear refractive index. [1] Due to the coherent superposition of transverse wave vectors with spatially modulated optical phases caused by the characteristic nonlinear refractive index of the optical medium and the spatially distributed intensity of the Gaussian beam, the SSPM of Gaussian beam in the nonlinear optical materials exhibits the optical concentric diffraction rings at the far-field. According to the even- or odd-integer difference of the nonlinear phase shift, which is regulated by the nonlinear refraction coefficient and the input intensity, the optical field with intensity-modulated spatial phases interferes either constructively or destructively with itself. Strong coherent light-matter interaction causes spatial phase modulation of the incident laser light and diffraction ring patterns in the far field. Following the discovery of the SSPM in liquid crystals by Durbin et al., Wu et al. explored the third-order nonlinear susceptibility in exfoliated graphene using the SSPM technique in 2011. [2-4] Since then, SSPM has seen a sharp rise in attention, and numerous research teams have looked into the nonlinear behaviour of various kinds of materials. Quantum confinement and nonlinear optical absorption are the main reasons for strong nonlinear optical properties in materials.

Halide perovskite materials have strong linear and nonlinear optical and electrical properties, due to these they applied in many optoelectronic applications, optical applications etc. $RbPBI_3$ has relatively thermodynamically stable at room temperature and stable crystallographic structure due to large I (iodine) atoms in halogen part. Nonlinear refractive index is the change in refractive index of the material or medium is proportional to the incident light intensity. It is denoted by n_2. By intensity dependent SSPM we got third order nonlinear susceptibility ($\chi^{(3)}$) and nonlinear refractive index (n_2). Many halide

perovskites were used to determine the nonlinear optical properties of that materials by researchers worldwide but RbPBI$_3$ first used in this work. this is a novel of its kind for this perovskite to determination of nonlinear optical refractive index (n$_2$) with different solvents and also nonlinear third order susceptibility ($\chi^{(3)}$).

5.1.1. Measurement Techniques for Material Specific Nonlinear Optical Properties:

Three independent methods are there to investigate materials NLO properties. They are as follows

- a) Degenerate Four Wave Mixing Technique (DFWM) – It is most powerful method among others.
- b) Z- Scan
- c) Spatial Self Phase Modulation (SSPM)

Z-Scan and DFWM both methods require high-cost advanced complicated experimental arrangements. [5-7] Same results can be getting from SSPM method. For this reason, SSPM technique become more acceptable and efficient one. We can get nonlinear refractive index (n$_2$) and nonlinear susceptibility (χ^3) from all these techniques. [8-10] In this experiment we used SSPM technique.

5.1.2. Theory and Mathematical Foundation of SSPM:

Kerr effect is the foundation principle behind SSPM response of nanomaterials.[11] This effect only applicable in laser light sources. The nonlinear refractive index of a material proportionally changes with incident light intensity. That means if intensity increases then nonlinear refractive index of that material also increases under same conditions. The relationship as follows,

$$n = n_0 + n_2 I \qquad \text{...............1}$$

here, I = intensity of incident light beam

　　n_0 = linear refractive index of that material

　　n_2 = nonlinear refractive index of that material

Phase of incident beam modulated by this Kerr effect. Here incident laser beam has Gaussian distribution. And nonlinear phase shift $\Delta\Psi$ (r) written as follows,

$$\Delta\Psi\ (r) = \frac{2\pi n_0}{\lambda} \int_0^{Leff} n_2\ I(r,z)dz \qquad \text{.....................2}$$

$R \in [0, +\infty)$ is the radial position of Gaussian beam

L_{eff} = effective length of the light beam travelling through cuvette

λ = wavelength of the laser beam

The phase shift $\Delta\Psi$ (r) of incident beam gets modulated because of changing nonlinear refractive index of material through Kerr effect. This phase shifting resulted diffraction rings in the far field due to spatial self-phase modulation process. The schematic representation shown in the figure 5.1.
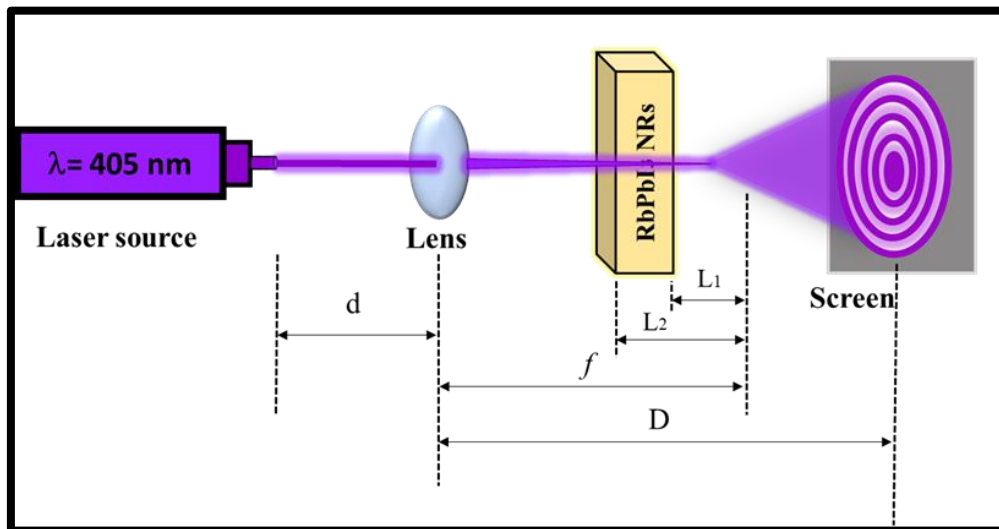

Figure 5.1: Schematic representation of generated diffraction rings due to SSPM

Two points in Gaussian incident field have same slopes, so, they are in same phase and construct bright rings in far field. Diffraction pattern have combination of bright and dark rings that governed by the following equation,

$$\Delta\Psi\ (r_1) - \Delta\Psi\ (r_2) = 2M\pi \qquad \ldots\ldots\ldots\ldots\ldots\ldots.3$$

M = integer number, odd for dark rings, even for bright rings.

L$_{eff}$ expressed as the following relation,

$$L_{eff} = \int_{L1}^{L2} \left(1 + \frac{z^2}{z0^2}\right)^{-1} dz = z_0 \tan^{-1}\left[\frac{z}{z0}\right]_{L_1}^{L_2} \qquad \ldots\ldots\ldots\ldots.4$$

Here $z_0 = \dfrac{\pi\omega_0^2}{\lambda}$ and $\omega_0 = \dfrac{1}{e2}$ beam radius, L$_1$, L$_2$ are the distances from focus (*f*) to cuvette sides.

From equation 2 and 4 we get,

$$n_2 = \frac{\lambda}{2n_0 L_{eff}} \cdot \frac{dN}{dI} \qquad \ldots\ldots\ldots\ldots\ldots.5$$

Here, I (0, z) = 2I = central peak intensity of Gaussian beam.

N2 is nonlinear refractive index of experimented material.

$\dfrac{dN}{dI}$ = slope of intensity vs rings no graph.

Third order nonlinear susceptibility $(\chi^{(3)})_{total}$ getting from following equation. [12-14]

$$(\chi^{(3)})_{total} = \frac{cn_0^2}{12\pi^2} 10^{-7} n_2 \ _{(e.s.u.)} \qquad \ldots\ldots\ldots\ldots.6$$

c = velocity of light in free space.

$$(\chi^{(3)})_{total} = (\chi^{(3)})_{monolayer} \times N^2_{eff} \qquad \ldots\ldots\ldots\ldots.7$$

here, N_{eff} = effective number of layers of material in cuvette.

$(\chi^{(3)})_{total}$ strongly dependent on incident optical electric field.

Equation 4,5,6,7 is used to calculate desire parameters.

5.1.3. *Wind-Chime model -* **Explanation for Light matter interaction in SSPM***:*

By nonlinear Kerr effect SSPM occurred and we got the diffraction patterns. Diameter of the diffraction rings changed with respect to intensity of the incident beam. By increasing the intensity of the incident laser beam diffraction rings became more bigger means their diameter increases. At a fixed intensity value these diameters became maximum. This incident described by "Wind-Chime model", first described by Wu et al. [15] Suspended nanorods reoriented by optical electric field of incident laser beam by energy relaxation process. By this process ring number increases with time. Nanorods dispersed in solvent considered as individual entities and polarized nanorods coherently interact with Gaussian incident laser beam shown in figure 5.2.
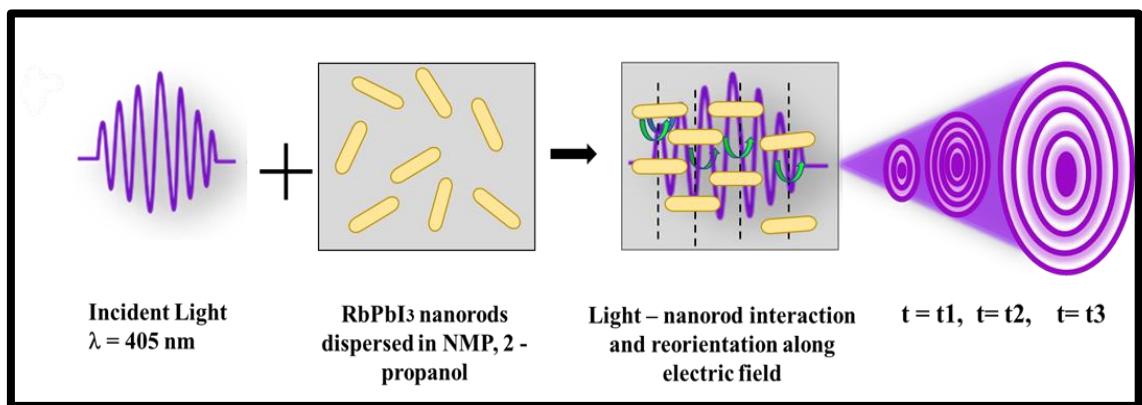

Figure 5.2: Dispersed RbPbI$_3$ nanorod interaction with incident laser beam and polarised along electric field of incident laser beam. Ring number increases with time. Schematic representation of Wind- Chime model.

5.2. Experiment Section:

5.2.1. Synthesis Process of RbPbI₃ Nanorods:

- **Materials needed:**

Lead (II) iodide (PbI₂, 99.99%, Sigma-Aldrich), rubidium iodide (RbI, Sigma-Alldrich), dimethylformamide (DMF, Alfa-Aesar), n-hexane (Alfa-Aesar), oleic acid (OA, Alfa-Aesar), n-octylamine (Sigma-Aldrich) and tert-butaol(Sigma-Aldrich) were used without any purification.

- **Synthesis process:**

Initially 1.0 mmol PbI₂ was dissolved in DMF and stirred at room temperature simultaneously, 1.0 mmol RBI was mixed in DI water separately. This aqueous solution mixed with aforesaid DMF-PbI₂ solution drop wise. An oil phase was prepared via adding hexane (10ml) with 1ml oleic acid and 0.5ml of n-octylamine. Furthermore, the solution mixture and the oil phase were mixed under vigorous stirring. 8ml tert-butanol was added into it instantly to initiates the demulsification. Finally, sample was collected via centrifugation followed by drying overnight in vacuum oven. The schematic diagram of synthesis process shown in the figure 5.3 below.
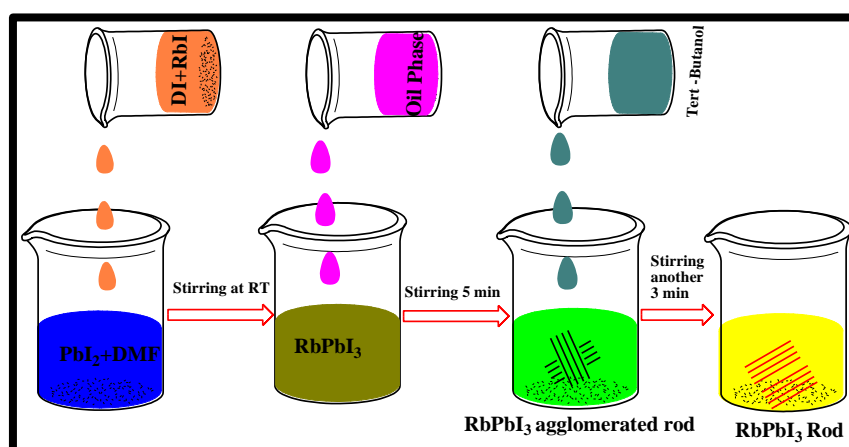

Figure 5.3: Schematic representation of RbPbI₃ nanorod synthesis process.

5.2.2. Basic Characterisation of Material:

5.2.2.1. XRD analysis:

X-Ray diffraction analysis was carried out by Rigaku MiniFlex 600 XRD instrument. Intensity vs. 2θ graph of $RbPbI_3$ sample shown in figure 5.4.
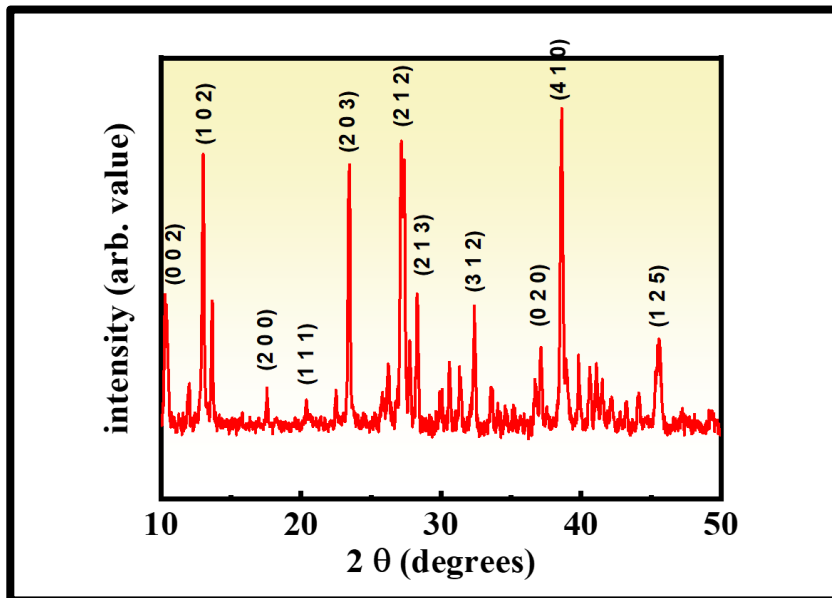

Figure 5.4: XRD pattern of RbPbI3 sample

By using Scherrer equation calculated average crystallite size is 41.29 nm. By using x-pert high score software it revealed that the material we synthesised was pure $RbPbI_3$ and matched ICDD card no ICDD-98-000-6067. It had orthorhombic crystal structure with P_{nma} space group. There are so many sharp peaks in xrd graph that is clear indicating that this material had very much crystallinity. These (h k l) values strongly indicating toward possibility of $RbPbI_3$ in the sample.

5.2.2.2. Morphological analysis:

The morphology and microstructure of the sample studied by field emission scanning electron microscope (Inspect F50) at an accelerating voltage of 5.0 kV. FESEM images are shown in figure 5.5.
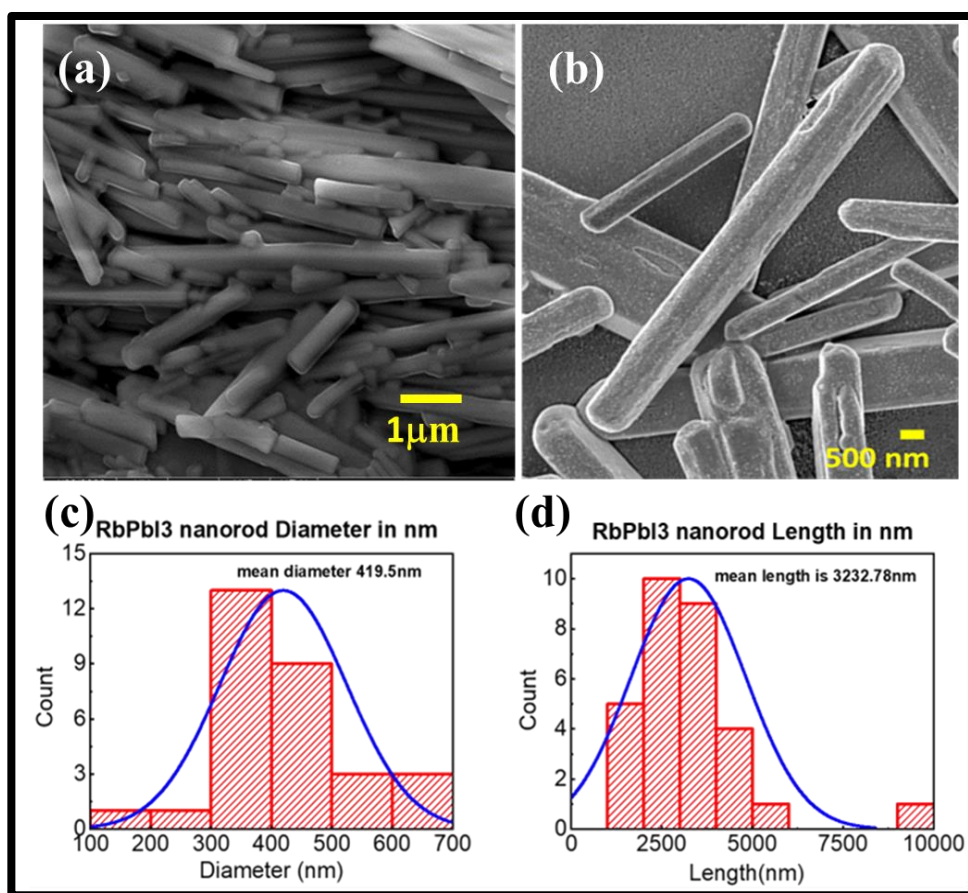
Figure 5.5: (a), (b) FESEM images for different magnifications. (c), (d) graphs for calculate mean diameter and length of RbPbI$_3$ NRs.

Here two FESEM images shown left one (a) at 1µm and right one (b) at 500 nm magnification. From these images it is clear that in our sample RbPbI$_3$ had nanorod structure. We also measured the length and diameters of nanorods via software tool. Average length and diameter are 3232.78 nm and 419.5 nm respectively. The statistical distribution of length and diameter with counts shown in figure 5.5 (c), (d).

5.2.2.3. Compositional analysis (EDS-Analysis):

The chemical compositions, as well as the spatial uniformity of the elemental distribution, were analysed by energy disruptive X-ray spectroscopy (EDS, Inspect F50) at 15.0 kV.

The EDS results are presented in figure 5.6. EDS spectra indicates that the sample is composed of Rb, Pb, I with an atomic ratio nearly 1:1:3 which is expected for orthorhombic $RbPbI_3$. extra carbon peak is found because of carbon tap. Elemental mapping confirms the uniformity in the distribution of all elements present in the sample $RbPbI_3$. The atomic weight percentages of all elements for sample $RbPbI_3$ presented in a tabular form table 5.1.

(a) EDS elemental analysis

Table 5.1

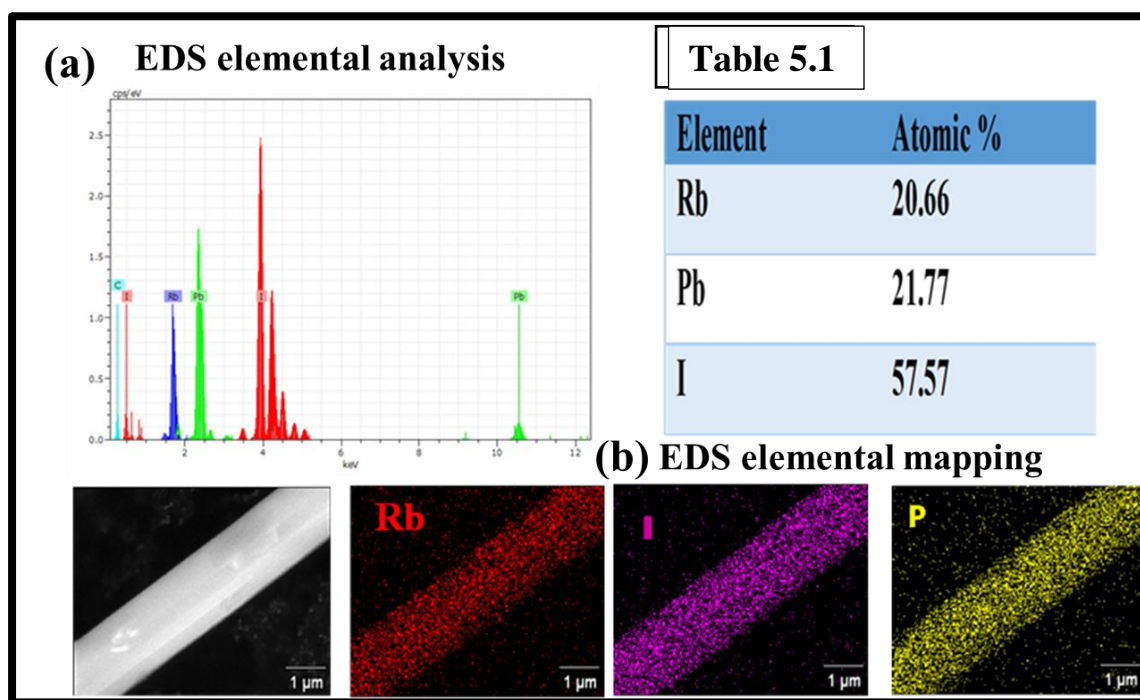| Element	Atomic %
Rb	20.66
Pb	21.77
I	57.57

(b) EDS elemental mapping

Figure 5.6: (a) EDS elemental analysis result showing elements present in the sample. (b) EDS elemental mapping that confirms uniformity in the distribution of all elements.

5.2.2.4. UV-Vis Absorbance Study – Band Gap Determination:

The band gap of the $RbPbI_3$ sample was analysed by UV - Vis - NIR spectrometer (Shimadzu UV-Vis-NIR (UV-3101-PC) spectrophotometer). Here only UV-Vis absorbance study conducted by dispersed in NMP solvent. The Tauc plot for determination of band gap of $RbPbI_3$ nanorods shown in figure 5.7. From this technique we easily

determined the direct band gap of the experimental halide perovskite material. The calculated band gap was 3.04 eV for RbPbI$_3$ nanorods in NMP medium.
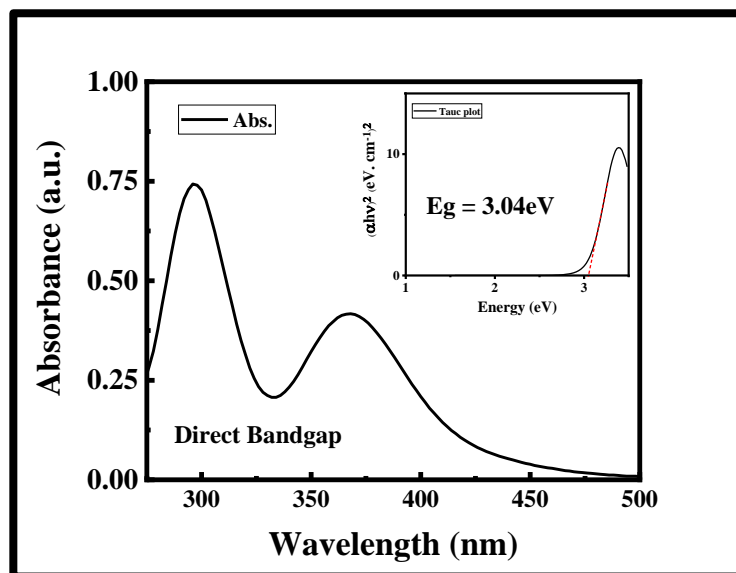

Figure 5.7: Absorbance spectra of RbPbI$_3$ nanorods in NMP, the respective Tauc plot given in inset.

5.3. SSPM Experiment – Nonlinear Refractive Index (n$_2$) and Third Order Susceptibility ($\chi^{(3)}$) Calculation:

We experimentally calculated the nonlinear refractive index and third order susceptibility for the RbPbI$_3$ perovskite nanorods. We have discussed in introduction section that ring numbers in SSPM experiment plays very important role to find out n$_2$ (nonlinear refractive index) and by getting n$_2$ we can get $\chi^{(3)}$ (third order susceptibility). For doing SSPM experiment we were chosen two polar solvents one is NMP (N-Methyl-2-pyrrolidone), and another is 2- Propanol. Here two different solvents used for investigation of viscosity

dependency of n_2. In this chapter we also discuss about how n_2 (nonlinear refractive index) changes with cuvette length (L) variation.

5.3.1. Sample preparation for SSPM experiment:

First 1mg of $RbPbI_3$ measured by digital weighting machine and poured into a centrifuge tube. 4 ml NMP added into that tube. The solution sonicated for 15 minutes for evenly dispersion of perovskite into NMP. After sonication dispersed solution ready for experiment. Another batch prepared for 2-propanol solvent with same weights.

5.3.2. SSPM response of $RbPbI_3$ when NMP used as solvent:

Violet and green both laser sources used in NMP solvent based SSPM experiment. In figure 5.8 shows the different diffraction rings formation with time for green laser. Here increase in ring number with time not shown for violet light measurement due to poor video output. Ring numbers and their diameters increases with time and intensity. In figure 5.9, (a), (b) shows diffraction pattern on screen on green and violet laser application at highest intensity and (c) shows intensity (I) vs. ring number (N) graph when NMP used as solvent.
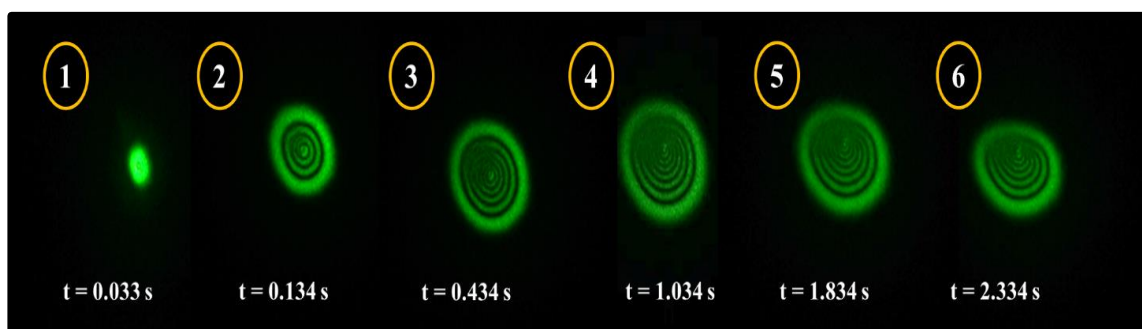

Figure 5.8: Diffraction ring pattern formed on the screen as a function of time for green
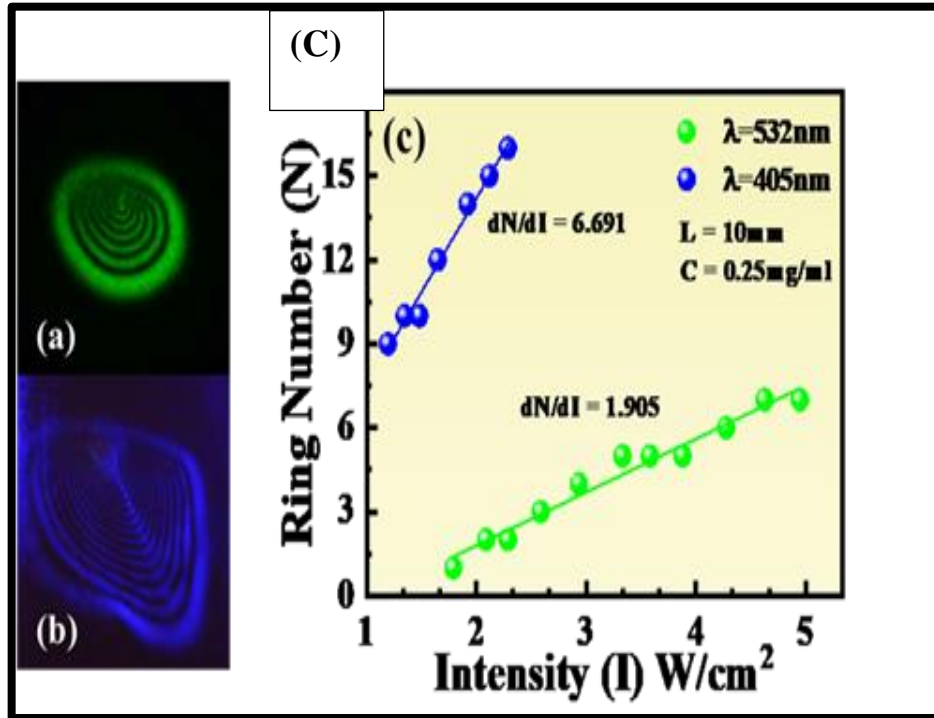
light (λ=532 nm)

Figure 5.9: (a), (b) diffraction rings at highest intensity for green and violet laser. (c)

graphical plot of diffraction ring numbers vs. laser intensity (l=532 nm, 405 nm)

Here only 10mm cuvette used. Both plots were linear fitted linearly and slops are 6.691

and 1.905 for violet and green lasers respectively. It is clearly seen that for low wavelength

light $\frac{dN}{dI}$ (slope of the plots) is high. Slope of the fitted curve increases when wavelength

decreases. We used 2.19 and 2.35 as n_0 (linear refractive index) for calculation of n_2. (These

values taken from literature) [16-17]. For green and violet lights calculated n_2 are 2.165x

10^{-5} and 6.196 x10^{-5} respectively. And third order susceptibility $\chi^{(3)}_{total}$ is 0.0030 and

0.0075 respectively. $\chi^{(3)}_{monolayer}$ values are 9.67 x10^{-9} and 2.38 x10^{-8} for green and violet

light application respectively.

5.3.3. SSPM response of RbPbI₃ when 2 – propanol used as solvent:

Only violet laser source used in 2 – propanol solvent based SSPM analysis because cuvette

length was varied in this case. We used cuvettes with three different lengths (L) like 10mm,

5mm, 1mm. intensity (I) vs. ring number (N) graph shown in figure 5.10. The diffraction rings also shown in figure 5.11 for 10, 5, 1 mm cuvette respectively at highest intensity. Ring numbers are dependent on cuvette length as cuvette length increases then ring no increases. For 10 mm cuvette we got very big diffraction ring diameter and greater number of rings compare to others. Slope values are 2.255, 1.813, 0.708 for L= 10, 5, 1 mm cuvettes. For 10 mm cuvette the amount of dispersed material in the medium was high compare to others, for this reason in 10mm cuvette light matter interaction was high resulted greater number of diffraction rings. Due to this, slope and ring numbers both are increased with increased cuvette length (L).
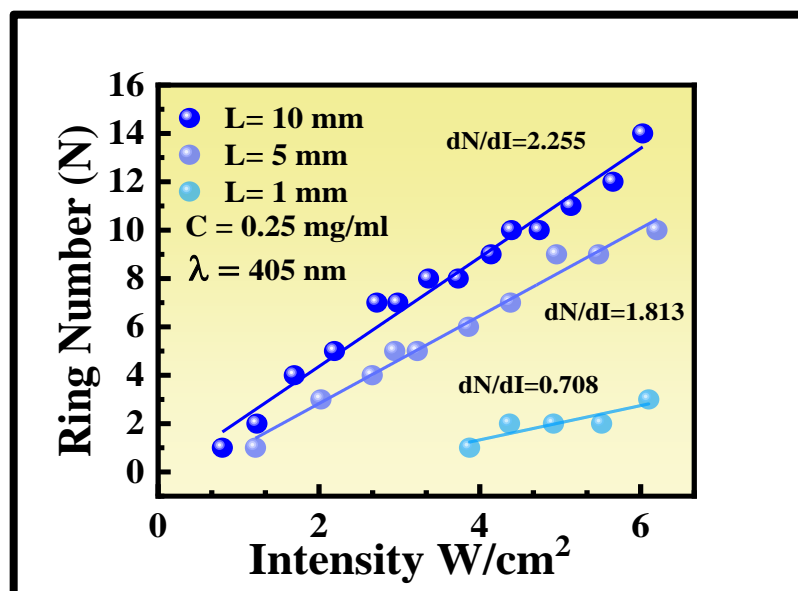

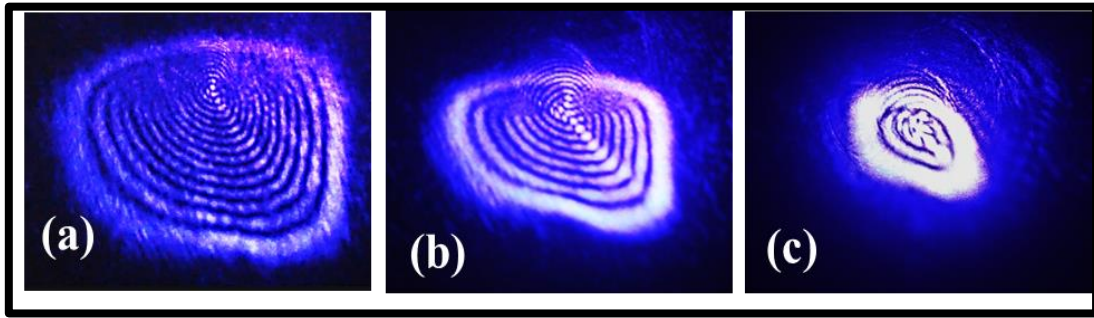**Figure 5.10**: Graphical plot of diffraction ring numbers vs. laser intensity (L= 10,5,1 mm)

Figure 5.11: Diffraction ring pattern formed on the screen at highest intensity
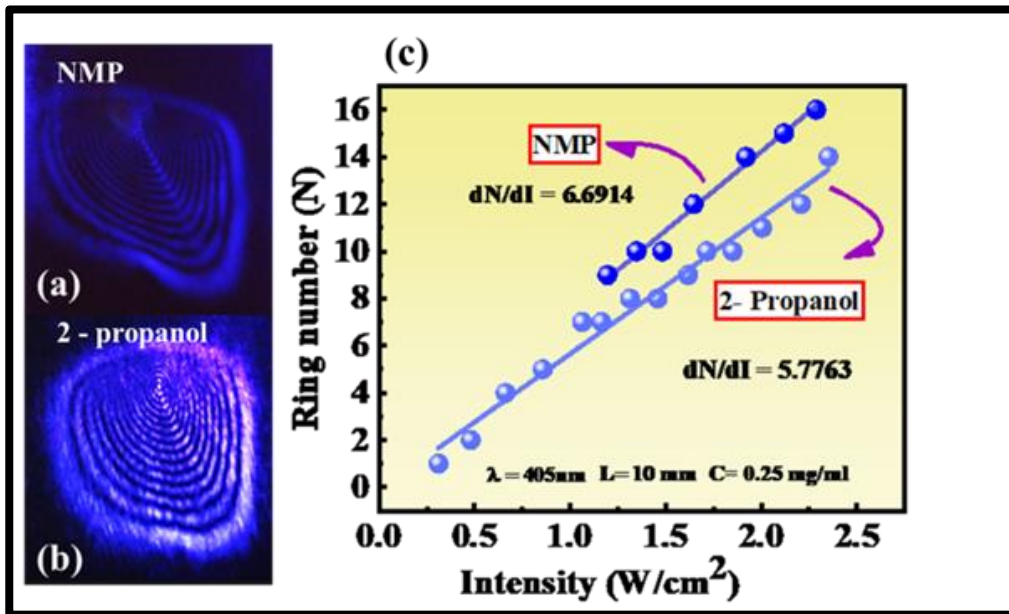
(λ=405 nm and L = 10,5,1 mm)

Figure 5.12: (a), (b) diffraction pattern on screen at highest intensity for RbPbI$_3$@NMP

and RbPbI$_3$@2- propanol respectively I = 2.28 W/cm$_2$, 2.35 W/cm$_2$ and L= 10mm(c)

shows the variation of ring numbers with intensity of incident laser for different viscus

mediums.

In figure 5.12 (c) slope of fitted curve for NMP higher than slope of fitted curve for 2-propanol. According to Wind-Chime model discussed in introduction section, suspended particles take short time to reorient in low viscous medium. Viscosity of NMP and 2 –

propanol is respectively 1.66 cP, 1.96 cP respectively. NMP is less viscous than 2-propanol. For this reason, slope of fitted curve is higher for NMP medium than 2 – propanol medium.

According to Wind- Chime model time required for formation of maximum circular ring is equal to time taken to polarize nanorods along electric field of incident laser beam. To calculate this time first time vs ring number graph plotted and then fitted with this given

$N = A \cdot \left(1 - e^{-t/\tau_c} \right)$ equation. Here N is ring number, A is constant value, τ_C is rise time. From figure 5.13 it is clearly noticed that when green laser used in NMP medium the rise time was calculated around 0.17879 sec and experimental patten formation time was 0.4752 sec when 10mm cuvette used. In 2 – propanol medium by using different cuvette length variation it is noticed that for 10 mm cuvette length rise time was small compare to others 0.22036 sec figure 5.14 and the ring formation time was same for 10- and 5-mm cuvette length 0.4667 sec but 0.4334 sec for 1mm cuvette length. Diffraction rings form on screen with respect to time for different cuvette lengths (a) for 10mm, (b) for 5mm, (c) for 1mmcuvettes respectively shown in the figure 5.15.
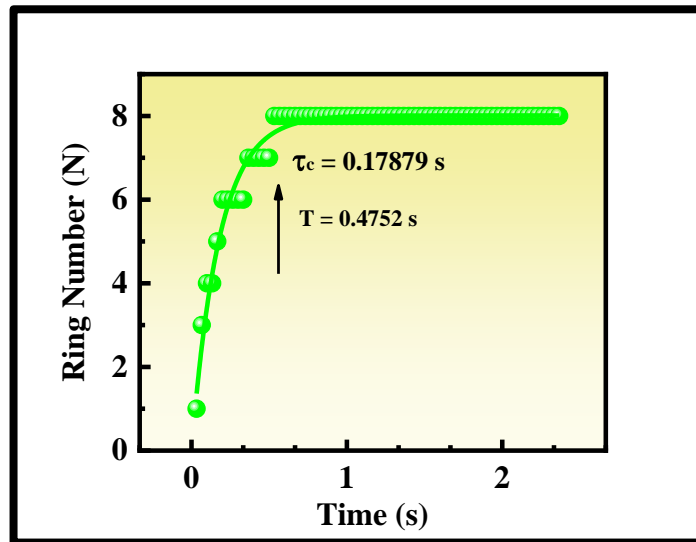

Figure 5.13: Evolution of diffraction ring numbers with time at highest intensity for green laser (λ=532 nm) and NMP solvent.
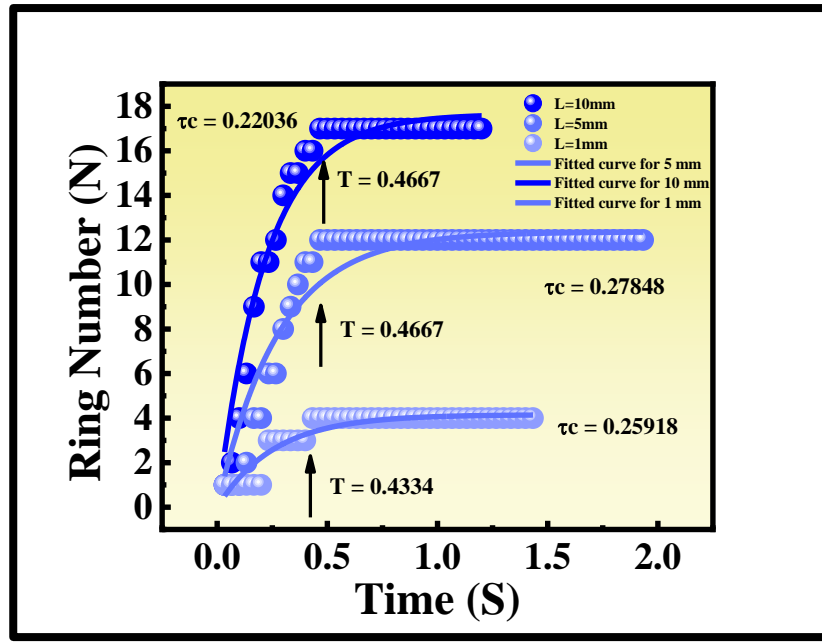
Figure 5.14: Evolution of diffraction ring numbers with time at highest intensity (I = 4.94 W/cm^2) for violet laser (λ=405 nm), different cuvettes and 2-propanol solvent.
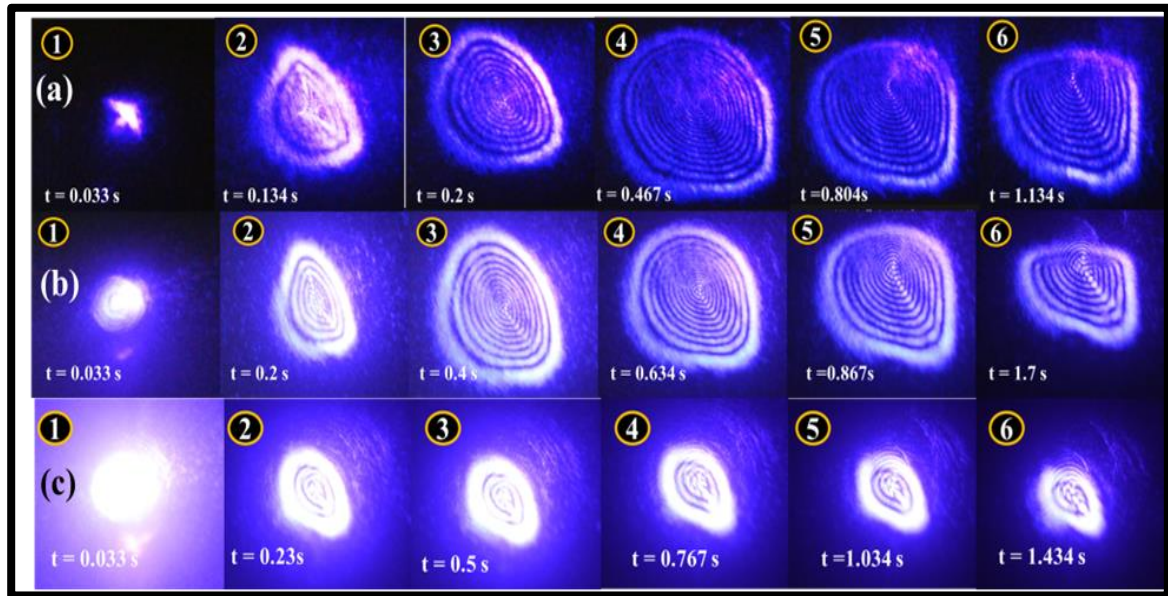

Figure 5.15: diffraction rings form on screen with respect to time for different cuvette lengths (a) for 10 mm, (b) for 5 mm, (c) for 1mm cuvettes respectively.

A summarised comparable table given below, here all calculated nonlinear optical parameters are given in table 5.2.

Table 5.2: Summarised comparable table for all calculated nonlinear optical parameters

Solution	Concentration (mg/ml)	Laser Wavelength (nm)	dN/dI	n_0	n_2	$\chi^{(3)}_{total}$	$\chi^{(3)}$ (monolayer)	Cuvette Length (L) (mm)
NMP	0.25	532	1.905	2.352	2.165×10^{-5}	0.0030	9.673×10^{-9}	10
NMP	0.25	405	6.691	2.19	6.196×10^{-5}	0.0075	2.382×10^{-8}	10
2- propanol	0.25	405	2.255	2.19	2.088×10^{-5}	0.00254	8.031×10^{-9}	10
2- propanol	0.25	405	1.813	2.19	3.356×10^{-5}	0.00405	1.291×10^{-8}	5
2- propanol	0.25	405	0.708	2.19	6.554×10^{-5}	0.00796	2.521×10^{-8}	1

5.3.4. Illustrative Explanation Behind Collapsed Upper Half of Diffraction Pattern:

From figure 5.15 it is clearly seen that upper half of the diffraction rings were distorted with time (collapsed towards centre). This collapse phenomenon started when diffraction rings reached maximum limit. It occurs along perpendicular axis not along horizontal axis and lower half remains unaltered. Non axis symmetrical thermal convection process is the reason behind this distorted diffraction pattern and first described by Wang et.al. [18] By this process material absorbs some part of the incident laser light then temperature gradient increases along the perpendicular direction of incident laser spot. This method initiates thermal convection process. [19] The concentration of material in upper part of the solution decreases than lower part. Due to this reason upper part of the incident laser less diffracted than lower part. For this reason, upper part of the diffraction pattern collapsed toward perpendicular direction shown in figure 5.16.

Half cone angle of the diffraction rings of the incident Gaussian laser beam is,

$$\theta_H = n_2 \left[-\frac{8IrL}{\omega_0^2} \exp\left(\frac{-2r^2}{\omega_0^2}\right) \right]_{max} \quad \ldots\ldots\ldots\ldots\ldots\ldots\ldots\ldots\ldots \quad 8$$

Where, $\left[-\frac{8IrL}{\omega_0^2} \exp\left(\frac{-2r^2}{\omega_0^2}\right) \right]$ is a constant, $r \in [0, +\infty)$.

θ_H is proportional to n_2 nonlinear refractive index) of the material. [20-22]

Distortion angle represented as,

$$\theta_D = \theta_H - \theta_{H'} = \frac{R_H}{D} - \frac{R_{H'}}{D} = \frac{R_D}{D} \quad \ldots\ldots\ldots\ldots\ldots\ldots \quad 9$$

R_H is maximum diffraction radius.

θ_H is maximum half diffraction angle, and by diffraction process R_H, θ_H changes.

θ_D represented as difference of nonlinear refractive index as follows,

$$\frac{\Delta n_2}{n_2} = \frac{\theta_D}{\theta_H} = \frac{R_D}{R_H} \quad \ldots\ldots\ldots\ldots\ldots\ldots\ldots\ldots\ldots\ldots\ldots \quad 10$$

$\frac{\Delta n_2}{n_2}$ is related with intensity of the incident laser beam, time and temperature of the medium
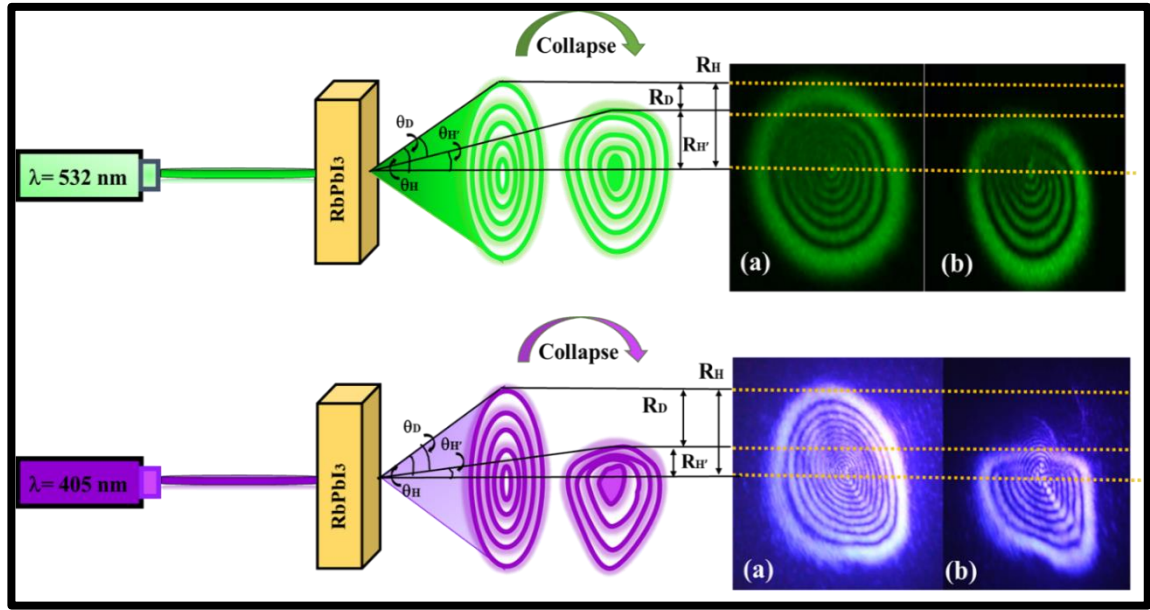
and surroundings.

Figure 5.16: Schematic representation with original images of collapse phenomenon of diffraction rings with half cone and distortion angle.

5.4. Conclusion:

In conclusion, we have successfully synthesized RbPbI$_3$ nanorods via low cost, less complicated chemical route. In this study we first calculate nonlinear refractive index and third order susceptibility for monolayer RbPbI$_3$ NRs in two different solvents by cost effective SSPM method. We successfully discussed the reasons behind different dN/dI values in different conditions. Large values of n$_2$ and $\chi^{(3)}$ indicates toward intensive nonlinear coherent interaction of incident beam with suspended perovskite NRs. Formation time (T) also calculated for different conditions. We strongly believe that these new findings open new optical application routes for RbPbI$_3$ perovskite in future.

5.5.   Reference:

[1] K. Sk *et al.*, "Nonlinear coherent light–matter interaction in 2D MoSe $_2$ nanoflakes for all-optical switching and logic applications," *Adv. Opt. Mater.*, p. 2200791, 2022.

[2] S. D. Durbin, S. M. Arakelian, Y. R. Shen, *Phys. Rev. Lett.* **1981**, *47*,1411.

[3] S. D. Durbin, S. M. Arakelian, Y. R. Shen, *Opt. Lett.* **1982**, *7*, 145.

[4] R. Wu, Y. Zhang, S. Yan, F. Bian, W. Wang, X. Bai, X. Lu, J. Zhao, E. Wang, *Nano Lett.* **2011**, *11*, 5159.

[5] S. K. Turitsyn, A. E. Bednyakova, M. P. Fedoruk, S. B. Papernyi, W. R. L. Clements, *Nat. Photonics* **2015**, *9*, 608.

[6] C. Wang, S. Xiao, X. Xiao, H. Zhu, L. Zhou, Y. Wang, X. Du, Y. Wang, Z. Yang, R. Duan, M. Zhong, H.-G. Rubahn, G. Zhang, Y. Li, J. He, *J. Phys. Chem. C* **2021**, *125*, 15441.

[7] Y. L. Wu, L. L. Zhu, Q. Wu, F. Sun, J. K. Wei, Y. C. Tian, W. L. Wang, X. D. Bai, X. Zuo, J. Zhao, *Appl. Phys. Lett.* **2016**, *108*, 241110.

[8] Y.-R. Shen, *The Principles of Nonlinear Optics*, Wiley, Hoboken, NJ **1984**.

[9] R. W. Boyd, *Nonlinear Optics*, Academic Press, Cambridge, MA **2020**.

[10] Y. Jia, Y. Liao, L. Wu, Y. Shan, X. Dai, H. Cai, Y. Xiang, D. Fan, *Nanoscale* **2019**, *11*, 4515.

[11] G. Wang, S. Zhang, F. A. Umran, X. Cheng, N. Dong, D. Coghlan, Y. Cheng, L. Zhang, W. J. Blau, J. Wang, *Appl. Phys. Lett.* **2014**, *104*, 141909.

[12] R. W. Boyd, *Nonlinear Optics*, Academic Press, Cambridge, MA **2020**.

[13] L. Wu, Y. Dong, J. Zhao, D. Ma, W. Huang, Y. Zhang, Y. Wang, X. Jiang, Y. Xiang, J. Li, Y. Feng, J. Xu, H. Zhang, *Adv. Mater.* **2019**, *31*, 1807981.

[14] Y. Shan, L. Wu, Y. Liao, J. Tang, X. Dai, Y. Xiang, *J. Mater. Chem. C* **2019**, *7*, 3811.

[15] Y. Wu, Q. Wu, F. Sun, C. Cheng, S. Meng, J. Zhao, *Proc. Natl. Acad. Sci. U. S. A.* **2015**, *112*, 11800.

[16] A. Natik, Y. Abid, R. Moubah, F. Khelfaoui, E. K. Hlil, H. Zaari, A. Benyoussef, M. Abid & H. Lassri (2020), 93:1, 54-61, DOI: <u>10.1080/01411594.2019.1699087</u>

[17] Tikaram Neupane, Hua Wang, William W. Yu, Bagher Tabibi, Felix Jaetae Seo, Second-order hyperpolarizability and all-optical-switching of intensity-modulated spatial self-phase modulation in CsPbBr1.5I1.5 perovskite quantum dot, Optics & Laser Technology, Volume 140, 2021, 107090, ISSN 0030-3992

[18] G. Wang, S. Zhang, F. A. Umran, X. Cheng, N. Dong, D. Coghlan, Y. Cheng, L. Zhang, W. J. Blau, J. Wang, *Appl. Phys. Lett.* **2014**, *104*, 141909.

[19] C. Teng, L. Su, J. Chen, J. Wang, *Composites, Part A* **2019**, *124*, 105498.

[20] Y. Jia, Y. Shan, L. Wu, X. Dai, D. Fan, Y. Xiang, *Photonics Res.* **2018**, *6*, 1040.

[21] L. Wu, Z. Xie, L. Lu, J. Zhao, Y. Wang, X. Jiang, Y. Ge, F. Zhang, S. Lu, Z. Guo, J. Liu, Y. Xiang, S. Xu, J. Li, D. Fan, H. Zhang, *Adv. Opt. Mater.* **2018**, *6*, 1700985.

[22] M. Zidan, M. El-Daher, M. Al-Ktaifani, A. Allahham, A. Ghanem, *Optik* **2020**, *219*, 165275.

Chapter 6

Grand Conclusion and Scopes for Future Works
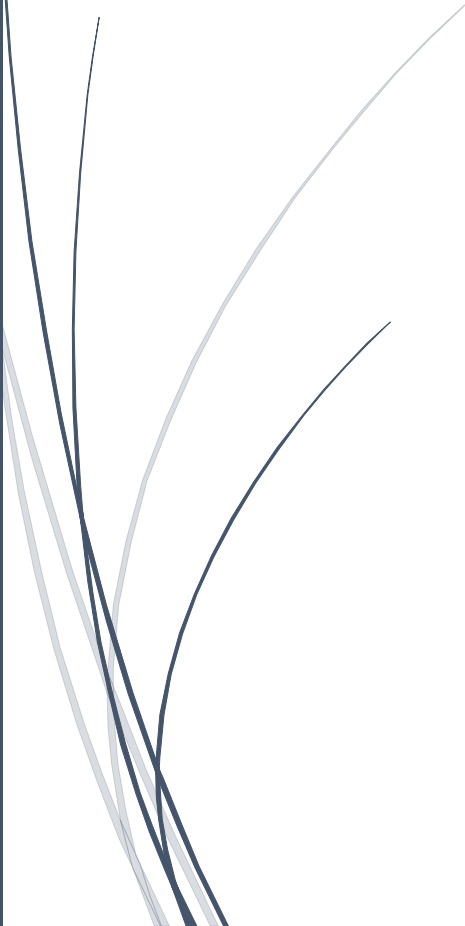
6.1. Conclusion:

For the first experiment, we have successfully demonstrated synthesis of TiO_2 nanorod arrays on FTO substrate via low cost, less complicated hydrothermal route. Synthesis time variation scheme adopted to see difference results in resistive switching (RS) behaviour. We have picked T1 device as our best device based on low and high resistive state current ratio. We also elaborately discussed the probable switching mechanism with respective carrier conduction mechanisms. We have successfully examined all types of synaptic functionalities with both electrical and optical inputs on T1 device. It is established that our T1 device has capability to applicable in neuromorphic device applications for both electrical and optical input signals. We successfully made a machine learning classifier model and test our device as an artificial vision sensor. Our classifier model capable to convert T1 device output current response to real world image output with accurate recognition of that with similar learning inputs.

In second experiment, we have successfully synthesized $RbPbI_3$ nanorods via low cost, less complicated chemical route. In this study we first calculate nonlinear refractive index and third order susceptibility for monolayer $RbPbI_3$ NRs in two different solvents by cost effective SSPM method. We successfully discussed the reasons behind different slopes of intensity vs. ring number plot (dN/dI) values in different conditions. Large values of n_2 and $\chi^{(3)}$ indicates toward intensive nonlinear coherent interaction of incident beam with suspended perovskite NRs. Formation time (T) also calculated for different conditions. The calculated nonlinear refractive indexes were 2.165×10^{-5} and 2.088×10^{-5} and third order susceptibility were 9.67×10^{-9} and 8.031×10^{-9} for NMP and 2-propanol solvents

respectively. We strongly believe that these new findings open new optical application routes for RbPbI$_3$ perovskite in future.

6.2. Scopes for Future Works:

First experiment related to neuromorphic memory device with artificial retina, work has drawn many exciting conclusions and answered crucial questions in terms of resistive switching mechanism, artificial retina device with machine learning. However, there remain several grand challenges like on/off ratio improvement, large retention time, large number of endurance cycles, memory crossbar array design and implementing in-memory computing with addressing the sneak path current issue. We would like to addressed these challenges in future with special modifications. In addition, we would try to recheck machine learning classifier model with different material based optical sensor devices for making generalised recognition model.

As the second experiment is stepping stone for RbPbI$_3$ material in nonlinear optics domain, we try to find out nonlinearly for different polar and non-polar solvents with Some other solvents also. We also would try to figure out the physical phenomenon behind generating that diffraction patterns and collapse nature of that pattern with time. In addition, we would like to find out the effect of temperature on whole process.

153